Astrophysical turbulence modeling

Astrophysical turbulence modeling

Axel Brandenburg[1,2] **and Åke Nordlund**[3]

[1] NORDITA, Roslagstullsbacken 23, SE-10691 Stockholm, Sweden
[2] Department of Astronomy, Stockholm University, SE-10691 Stockholm, Sweden
[3] Niels Bohr Institute, Juliane Maries Vej 30, DK-2100 Copenhagen Ø, Denmark

Abstract
The role of turbulence in various astrophysical settings is reviewed. Among the differences to laboratory and atmospheric turbulence we highlight the ubiquitous presence of magnetic fields that are generally produced and maintained by dynamo action. The extreme temperature and density contrasts and stratifications are emphasized in connection with turbulence in the interstellar medium and in stars with outer convection zones, respectively. In many cases turbulence plays an essential role in facilitating enhanced transport of mass, momentum, energy and magnetic fields in terms of the corresponding coarse-grained mean fields. Those transport properties are usually strongly modified by anisotropies and often completely new effects emerge in such a description that have no correspondence in terms of the original (non-coarse-grained) fields.

(Some figures in this article are in colour only in the electronic version)

Contents

1. Introduction

Astrophysical flows tend to be turbulent in the sense of being highly irregular. The study of astrophysical turbulence is important for several reasons. Firstly, turbulence needs to be taken into account when modeling most astrophysical systems. It can provide enhanced turbulent viscosity, turbulent heating, turbulent pressure, and leads to other effects, some of which can be non-diffusive in nature. Secondly, turbulence needs to be taken into account when interpreting observations of such systems. This is particularly evident in modeling line broadening and line asymmetries. Thirdly, astrophysical turbulence often spans an enormous range of length scales, allowing unique insights into the scaling properties of turbulence.

In many text books various definitions of turbulence are suggested. However, none of them is quite without problems. Throughout this review, turbulence will remain a loosely defined property of flows that are highly irregular in space and time.

Astrophysical turbulence as such is in principle no different from ordinary turbulence. What is characteristic about it is the extremes in some parameters, e.g. huge Reynolds numbers, Prandtl numbers very different from unity, and, in some cases, strong density stratification and/or very high Mach numbers. Also, of course, the gas is often ionized and hence electrically conducting, so the interaction with magnetic fields cannot be neglected. As a rule, astrophysical flows tend to be magnetized spontaneously by self-excited dynamo action.

In contrast to laboratory and technical realizations of turbulence, where the driving often comes from the interaction with boundaries, astrophysical turbulence tends to be largely independent of explicit boundaries and is facilitated by intrinsic instabilities. Another difference between astrophysical and laboratory turbulence is the fact that, with very few exceptions, *in situ* observations are impossible and one has to rely on the radiative properties of the gas to infer velocity, temperature and magnetic fields, for example. Yet another difference is that in some astrophysical flows the gas is extremely tenuous and close to collisionless, so the fluid approximation may actually break down. In some cases, multi-fluid descriptions are possible, for example when charged and neutral species move at different speeds, have different temperatures, or when positive and negative charge carriers, as well as dust particles need to be considered. However, quite often the multi-fluid description is then also not sufficient and it is better to employ more accurate techniques using, for example, particle-in-cell (PIC) methods or to solve the underlying Vlasov equations. This can be made more feasible by making use of the guide-field or gyrokinetic approximations, where one averages out the azimuthal particle position around magnetic field lines.

Astrophysical turbulence has been discussed in many excellent text books and reviews [1–10]. In recent years, however, high-resolution numerical simulations have become feasible and have added significantly to our understanding. Furthermore, the availability of three-dimensional codes has helped us to make astrophysical turbulence a natural ingredient in many astrophysical investigations. The purpose of this review is to highlight recent progress in the field. We will focus on hydrodynamic and magnetohydrodynamic (MHD) aspects, but will try to keep the level of repetition with earlier reviews at a minimum. In particular, we shall not go in depth into aspects of dynamo theory, but refer instead to the recent review of Brandenburg and Subramanian [11] on recent progress and in particular on the nonlinear saturation of dynamos.

2. Commonly used tools and conventions

Throughout this review we assume some basic level of familiarity with commonly used tools and techniques in turbulence research. Here we only review the essentials in simplistic terms.

2.1. Spectra

Common tools include energy and helicity spectra, as well as structure functions and structure function exponents. These concepts become particularly useful if spatial homogeneity can be assumed. In simulations this usually means that one deals with triply periodic boundary conditions. Alternatively, one can apply these tools to just one or two periodic directions (for example convection in a domain with periodic boundary conditions in the horizontal directions).

In incompressible (or nearly incompressible) isotropic turbulence one usually defines the spectral energy per unit mass,

$$E(k, t) = \sum_{k_- < |\boldsymbol{k}| \leqslant k_+} |\hat{\boldsymbol{u}}(\boldsymbol{k}, t)|^2, \tag{1}$$

where $k_{\pm} = k \pm \delta k/2$ mark a constant linear interval around wavenumber k, and the hat on $\boldsymbol{u}$ denotes the three-dimensional Fourier transformation in space. The spectral kinetic energy is normalized such that

$$\int_0^\infty E(k)\, \mathrm{d}k = \frac{1}{2}\langle \boldsymbol{u}^2 \rangle, \tag{2}$$

where angular brackets denote volume averaging. This equation shows that the dimension of $E(k, t)$ is $\mathrm{cm}^3\,\mathrm{s}^{-2}$, and $E(k)$ can be interpreted as the kinetic energy per unit mass and wavenumber.

In turbulent flows spectra remain in general time-dependent, so one is interested in spectra that are averaged over a sufficiently long time span. Such spectra can then also be compared with analytic predictions where statistical averaging is adopted instead.

In strongly compressible flows one can also define the spectrum of kinetic energy per unit volume as

$$E_2(k, t) = \sum_{k_- < |\boldsymbol{k}| \leqslant k_+} |\widehat{\rho^{1/2}\boldsymbol{u}}|^2, \tag{3}$$

and the spectrum

$$E_3(k, t) = \sum_{k_- < |\boldsymbol{k}| \leqslant k_+} |\widehat{\rho^{1/3}\boldsymbol{u}}|^2, \tag{4}$$

which does not have a simple physical interpretation, except that $E_3(k, t)^{3/2}$, integrated over k, has the dimension of an

energy flux [12]. In strongly compressible (e.g. supersonic) flows these various spectra can become quite distinct. The closest agreement between spectra for subsonic and supersonic turbulence is achieved when using the quantity $E_3(k, t)$ [13].

In anisotropic turbulence it is useful to consider the spectral energy dependence along and perpendicular to the preferred direction of the turbulence, i.e. $E(k_\perp, k_\parallel, t)$. Examples where this is important include rotating turbulence and turbulence in the presence of a strong magnetic field, but also inhomogeneous turbulence such as stratified turbulence and convection where one usually considers the spectral dependence on the horizontal wavenumber only.

The kinetic helicity spectrum is defined as

$$F(k) = \sum_{k_- < |\boldsymbol{k}| \leqslant k_+} (\hat{\boldsymbol{\omega}}^* \cdot \hat{\boldsymbol{u}} + \hat{\boldsymbol{\omega}} \cdot \hat{\boldsymbol{u}}^*), \tag{5}$$

where $\boldsymbol{\omega} = \boldsymbol{\nabla} \times \boldsymbol{u}$ is the vorticity, and asterisks denote complex conjugation. The kinetic helicity spectrum is normalized such that

$$\int_0^\infty F(k)\, \mathrm{d}k = \langle \boldsymbol{\omega} \cdot \boldsymbol{u} \rangle. \tag{6}$$

This kinetic helicity spectrum obeys the realizability condition,

$$|F(k)| \leqslant 2k E(k), \tag{7}$$

which is easily demonstrated by decomposing velocity and vorticity into positively and negatively polarized waves [11, 14]. Sometimes the helicity is defined with a 1/2 factor, just like the energy is. In that case the factor 2 in equation (7) would disappear.

Equivalent concepts and definitions also apply to the magnetic field $\boldsymbol{B}$, where one defines spectra of magnetic energy $M(k)$, magnetic helicity $H(k)$ and current helicity $C(k)$, which are normalized such that $\int M(k)\, \mathrm{d}k = \langle \boldsymbol{B}^2 \rangle / 2\mu_0$, where μ_0 is the vacuum permeability, $\int H(k)\, \mathrm{d}k = \langle \boldsymbol{A} \cdot \boldsymbol{B} \rangle$ and $\int C(k)\, \mathrm{d}k = \langle \boldsymbol{J} \cdot \boldsymbol{B} \rangle$. Here, $\boldsymbol{A}$ is the magnetic vector potential with $\boldsymbol{B} = \boldsymbol{\nabla} \times \boldsymbol{A}$ and $\boldsymbol{J} = \boldsymbol{\nabla} \times \boldsymbol{B} / \mu_0$ is the current density. The magnetic helicity and its spectrum are gauge-invariant because of the assumed periodicity of the underlying domain. In that case the addition of a gradient term, $\boldsymbol{\nabla}\Lambda$, in $\boldsymbol{A}$ has no effect, because $\langle \boldsymbol{\nabla}\Lambda \cdot \boldsymbol{B} \rangle = \langle \Lambda \boldsymbol{\nabla} \cdot \boldsymbol{B} \rangle = 0$, where we have used the condition that $\boldsymbol{B}$ is solenoidal. Additional mathematical properties can be found in [15]. Magnetic helicity is an important quantity, because it is conserved in the limit of vanishing magnetic resistivity and in the absence of boundary losses. Another similarly conserved quantity is the cross helicity, $\langle \boldsymbol{u} \cdot \boldsymbol{B} \rangle$. Its sign indicates whether Alfvén waves travel preferentially parallel or antiparallel to the local magnetic field.

2.2. Turbulent cascade

The energy-carrying scale is often defined as the scale $\ell_f = 2\pi/k_f$, where k_f is the wavenumber where the energy spectrum peaks. It is close to the integral scale $\ell_I = 2\pi/k_I$, where $k_I^{-1} = \int k^{-1} E(k)\, \mathrm{d}k / \int E(k)\, \mathrm{d}k$.

Turbulence is driven either by some explicit stirring or by some type of instability. Explicit stirring is frequently used in direct numerical simulations (DNS) and large-eddy simulations (LES). Here, DNS means that one considers the original equations with the proper diffusion term, as opposed to other schemes such as LES that are motivated by numerical considerations and limited resolution. An astrophysical example is the driving accomplished by supernova explosions in the interstellar medium within each galaxy. Examples of instability-driven turbulence include Rayleigh–Bénard convection, the magneto-rotational instability (MRI) and shear flow instabilities with inflection points resulting from rigid surfaces such as the accretion disk near the surface of a neutron star. In the latter case the domain is obviously no longer periodic.

The driving usually occurs over a certain range of length scales around the wavenumber k_f. The nonlinearity of the hydrodynamic equations produces power on progressively smaller scales (larger wavenumbers). Qualitatively, this leads to a cascade of energy from large to small scales until energy is dissipated at scales corresponding to the wavenumber k_d. The range of wavenumbers between k_f and k_d is called the inertial range. An important quantitative property of turbulence is the approximate constancy of spectral energy flux ϵ throughout the inertial range, where ϵ has dimensions $\mathrm{cm}^2\,\mathrm{s}^{-3}$. Making the ansatz

$$E(k) = C_K \epsilon^a k^b, \tag{8}$$

where C_K is the Kolmogorov constant, the values of the exponents a and b are determined by matching the dimensions for length (cm) and time (s) as follows: $3 = 2a - b$ and $2 = 3a$, respectively. This yields $a = 2/3$ and $b = -5/3$, so $E(k) = C_K \epsilon^{2/3} k^{-5/3}$.

The length of the inertial range can be calculated by assuming that $E(k)$ is finite only in the range $k_f \leqslant k \leqslant k_d$. Thus, u_{rms} and ϵ are given by the two integrals

$$\frac{1}{2} u_{\mathrm{rms}}^2 = \int_{k_f}^{k_d} E(k)\, \mathrm{d}k \approx \frac{3}{2} C_K \epsilon^{2/3} k_f^{-2/3}, \tag{9}$$

$$\epsilon = \int_{k_f}^{k_d} 2\nu k^2 E(k)\, \mathrm{d}k \approx \frac{3}{2} \nu C_K \epsilon^{2/3} k_d^{4/3}, \tag{10}$$

which are just the normalization condition of $E(k)$ and the definition of the energy dissipation, respectively. Here, ν is the kinematic viscosity. Eliminating ϵ, and writing the result in terms of the Reynolds number yields

$$Re = \frac{u_{\mathrm{rms}}}{\nu k_f} \approx \frac{3}{2}\sqrt{3}\, C_K^{3/2} \left(\frac{k_d}{k_f}\right)^{4/3}. \tag{11}$$

Thus, the length of the inertial range scales with the Reynolds number like $k_d/k_f \approx Re^{3/4}$; see, e.g., [16].

In astrophysics one often deals with extremely large Reynolds numbers, and hence an extremely broad inertial range. This is in practice not possible to simulate. However, many aspects of interest are independent of the length of the inertial range. Those that are not exhibit a well-understood scaling with Reynolds number. This is the main reason why it is at all possible to attempt simulating astrophysical systems on the computer!

2.3. Taylor hypothesis and one-dimensional spectra

In laboratory and atmospheric turbulence, for example, one usually measures time series which allow only one-dimensional spectra to be determined. This involves making the Taylor hypothesis, i.e. the assumption that the temporal power spectrum, $\tilde{u}(\omega)$, can be associated with a spatial one, $\hat{u}(k)$, via $\omega = U_0 k$. Here, U_0 is the mean flow at the location of the detector.

It is important to realize that one-dimensional spectra can differ from the fully three-dimensional spectra that are normally considered in numerical simulations of turbulent flows. The two agree only in regions of the spectrum where one has power law scaling, i.e. where $E(k) \sim k^n$ with some exponent n. This is evidently not the case near the dissipation subrange and near the sub-inertial range at small wavenumbers. This is probably the main reason why spectra from high-resolution DNS show a significantly shallower spectrum just before the dissipative subrange than the one-dimensional spectra obtained using the Taylor hypothesis, where a shallower part in the spectrum is essentially absent. In the following we briefly explain this difference [17].

Consider the case of a one-dimensional spectrum obtained by Fourier transformation over the z direction. To relate this to the three-dimensional spectrum, we average over the remaining x and y directions. Thus, we compute for $k_z > 0$

$$E_{1D}(k_z) = \iint |\hat{u}(x, y, k_z)|^2 \frac{dx\,dy}{L_x L_y}. \tag{12}$$

Next, using Parseval's relation for converting the averaging in real space to an integration in spectral space, we can write

$$\begin{aligned} E_{1D}(k_z) &= \iint |\hat{u}(k_x, k_y, k_z)|^2 \, dk_x \, dk_y \\ &= 2\pi \int_0^\infty |\hat{u}(k_r, k_z)|^2 \, k_r \, dk_r, \end{aligned} \tag{13}$$

where we have assumed that $|\hat{u}|^2$ is statistically axisymmetric, i.e. independent of the azimuthal angle about the k_z axis. Next, we use $k_r^2 = k^2 - k_z^2$ to replace the $k_r\,dk_r$ integration by one over $k\,dk$ in the range from $k_z \leqslant k < \infty$, i.e.

$$E_{1D}(k_z) = 2\pi \int_{k_z}^\infty |\hat{u}(k)|^2 \, k \, dk = \int_{k_z}^\infty \frac{E(k)}{k} \, dk, \tag{14}$$

where we have used the fact that the three-dimensional spectrum can also be written as $E(k) = 2\pi k^2 |\hat{u}(k)|^2$, where we have assumed averaging over full shells in wavenumber space. Thus, we see that one-dimensional spectra, $E_{1D}(k)$, are related to the fully three-dimensional spectra, $E(k)$, via integration, or via differentiation for the reverse operation, i.e.

$$E_{1D}(k) = \int_k^\infty \frac{E(k')}{k'} \, dk' \qquad \text{and} \qquad E(k) = -k \frac{dE_{1D}}{dk}. \tag{15}$$

We reiterate that, if one of the two spectra were a pure power law, the other one would also be a pure power law. However, this assumption breaks down near k_f and k_d. We mention this aspect here, because one of the unexpected results obtained

from a number of simulations over the last decade is a strong departure from the Kolmogorov $k^{-5/3}$ slope near k_d, where the spectrum can be substantially shallower [17–19]. This is now known as the bottleneck effect [20] and was first noticed in atmospheric turbulence [21]. It is by far not as marked in one-dimensional spectra as in three-dimensional spectra from recent high-resolution DNS [17].

2.4. Intermittency

The scaling of velocity differences over fixed distances is different in different locations. The flow is therefore said to be intermittent. A related property is that the scaling of the structure functions,

$$S_p(r, t) \equiv \langle |\boldsymbol{u}(\boldsymbol{x} + \boldsymbol{r}, t) - \boldsymbol{u}(\boldsymbol{x}, t)|^p \rangle, \tag{16}$$

with distance $r = |\boldsymbol{r}|$ deviates from the scaling $r^{p/3}$ for all moments $p \neq 3$, for both parallel ($\boldsymbol{r}$ parallel to $\boldsymbol{u}$) and transverse ($\boldsymbol{r}$ perpendicular to $\boldsymbol{u}$) structure functions. This property is quantified by the structure function exponents, ζ_p, which denote the slopes in graphs of $\ln S_p(r, t)$ with $\ln r$. The averaging, denoted by angular brackets, is here taken to be over the full volume.

In practice, approximate scaling can only be identified in a rather limited range of $\ln r$. Analytic theory predicts $\zeta_3 = 1$; see, e.g., [6, 8]. This property is often used to improve the accuracy in the determination of ζ_p for $p \neq 3$ from numerical or experimental data by plotting $\ln S_p(r, t)$ versus $\ln S_3(r, t)$. This procedure is referred to as extended self-similarity or ESS [22].

Intermittency is linked to the property that the ζ_p deviate from a linear dependence on p. Completely non-intermittent behavior would mean $\zeta_p = p/3$. A phenomenological relation that describes the behavior observed in experiments and simulations is given by the She–Leveque relation [23]

$$\zeta_p = \frac{p}{9} + C \left[1 - \left(1 - \frac{2/3}{C} \right)^{p/3} \right], \tag{17}$$

where C is interpreted as the co-dimension of the dissipative structures. For weakly compressible or incompressible turbulence the dissipative structures are one-dimensional tube-like structures, so the co-dimension is $C = 2$. Under compressible conditions the dissipative structures tend to become two-dimensional sheet-like structures, so $C = 1$ [24], which is also borne out by simulations of highly supersonic turbulence [25, 26]. Sheet-like dissipative structures are also expected in hydromagnetic turbulence, where these structures correspond to current sheets. In that case one expects the same scaling as for supersonic turbulence [27]. However, in incompressible hydromagnetic turbulence with constant density $\rho = \rho_0$, the relevant structure functions are based on the so-called Elsasser variables $\boldsymbol{z}^\pm = \boldsymbol{u} \pm \boldsymbol{B}/\sqrt{\mu_0 \rho_0}$. In that case, analytic theory predicts that the mixed third-order longitudinal structure functions of Politano and Pouquet [28],

$$S_{3\parallel}^\pm(r) = \langle \delta z_\parallel^\mp(r) [\delta z^\pm(r)]^2 \rangle, \tag{18}$$

4

scale linearly with $r = |\boldsymbol{r}|$. Here, $\delta z^\pm(r) = z^\pm(\boldsymbol{x} + \boldsymbol{r}) - z^\pm(\boldsymbol{x})$, $\delta z_\parallel^\pm(r) = \delta z^\pm \cdot \hat{\boldsymbol{r}}$ and $\hat{\boldsymbol{r}} = \boldsymbol{r}/r$ is the unit vector of $\boldsymbol{r}$.

Simulations tend to give slightly different scalings for the longitudinal and transverse structure functions. This may be a consequence of different cascade speeds for longitudinal and transverse velocity increments [29], but it may also just be an artifact of insufficient resolution and may go away at larger resolution, as indicated by recent simulations at high numerical resolution [13].

The assumption of the constancy of the spectral flux is well confirmed, but the correlation between energy injection and energy dissipation displays significant scatter. This is mostly because the spectral flux fluctuates significantly in time and there is some delay before the spectral energy has reached the dissipation scale. By taking into account the appropriate delay the scatter can be significantly reduced [30]. The energy flux at large scales is characterized by

$$\epsilon = C_\epsilon u_{1D}^3/L, \tag{19}$$

where $C_\epsilon \approx 0.5$. It is customary to define the length scale as $L = 3\pi/4k_f$, so in terms of k_f and $u_{rms}^2 = 3u_{1D}^2$ we can then write

$$\epsilon \approx 0.04\, k_f u_{rms}^3. \tag{20}$$

This formula will be useful later in connection with turbulence in interstellar and intergalactic media.

3. Sites of astrophysical turbulence

The following discussion is concerned mainly with observations and simulations covering a range of astrophysical settings where turbulence occurs. In some cases strong theoretical evidence is used to argue for the existence of turbulence, as for example in accretion disks where turbulence has not yet been observed explicitly [31].

3.1. Solar wind

The gas above the visible surface of the Sun is not in hydrostatic equilibrium. Instead, because of geometrical constraints and because of a gravitational potential inversely proportional to the radial distance, there is the possibility of a critical point, where the radial velocity equals the sound speed. The theory of such flows was first understood by Parker [32] in 1967 and is now explained in a number of text books on compressible flows or on astrophysical fluid dynamics [33, 34]. Other transonic flows of this type include those through a Laval nozzle, as well as Roche-lobe overflow between binaries, astrophysical jets from accretion disks and Bondi accretion. In the case of the Sun the gas reaches speeds of around $400\,\mathrm{km\,s^{-1}}$ in the equatorial plane and $800\,\mathrm{km\,s^{-1}}$ at higher latitudes [35]. The solar wind is turbulent and fluctuates between 300 and $800\,\mathrm{km\,s^{-1}}$ on time scales ranging from seconds to hundreds of hours [7].

In the case of the solar wind, spectral information can be obtained under the Taylor hypothesis that was discussed in section 2.3. Using this hypothesis the following properties have been inferred.

- An approximate $k^{-5/3}$ energy spectrum both for velocity and magnetic field [36].
- Below the ion Larmor radius a steeper spectrum (between k^{-2} and k^{-4}) is found for the magnetic field [37]. In view of theoretical expectations the transition to a $k^{-7/3}$ spectrum for the magnetic field together with a $k^{-1/3}$ spectrum for the electric field is particularly interesting [38, 39]; see figure 1.
- Finite magnetic helicity (negative in the northern hemisphere and positive in the southern hemisphere), possibly with a $k^{-7/3}$ spectrum [40].
- Finite cross helicity of positive sign, indicating outward traveling waves [41].
- Decay of turbulence with distance and evidence for additional heating [7, 36, 42, 43].

A possible connection between a $k^{-7/3}$ tail in the energy spectrum at small scales (below the scale of the ion Larmor radius) and so-called electron MHD as a model for collisionless plasmas such as the solar corona and the Earth's magnetosphere has been discussed [44]. A similar slope has now also been seen in simulations using the gyrokinetic equations [38]. These equations emerge from the Vlasov equations for a collisionless plasma by averaging over the azimuthal angle of the gyrokinetic motions [45]. Let us also mention here the possibility of obtaining spectra steeper than $k^{-7/3}$ using electron MHD when equipartition between kinetic and magnetic energies is not satisfied [46], or when compressible effects are included [47].

In view of our discussion in section 2.3, it should be noted that near the break point where the spectral index changes, the spectra inferred using the Taylor hypothesis are not exactly representative of the three-dimensional spectra obtained from simulations. However, in view of other general uncertainties, the changes in the spectral slopes are probably sufficiently weak to be ignorable.

3.2. Solar convection

The visible surface of the Sun is the photosphere, from where photons can reach the Earth in a direct path. Deeper inside the Sun the gas is opaque and photons are continuously absorbed and re-emitted, following approximately a diffusion-like process. At the surface, the Sun exhibits a granular pattern that can already be seen with small amateur telescopes. The pattern is irregular and changes on a time scale of around 5 min. The horizontal pattern size is 1–2 Mm. Here and elsewhere we use $1\,\mathrm{Mm} = 1000\,\mathrm{km}$ as a convenient length scale. The visible granulation is just a thin layer on top of a 200 Mm deep convection zone. The convection zone covers the outer 30% of the Sun by radius. The inner 70% is convectively stable. This region is referred to as the radiative interior.

Its overall dynamics can be understood through simulations and turbulence theory (i.e. mixing-length theory) [5]. Excellent agreement between observed and simulated granulation patterns has been obtained; see figure 2. By calculating diagnostic spectra in the visible light and comparing with observations one can determine the abundance
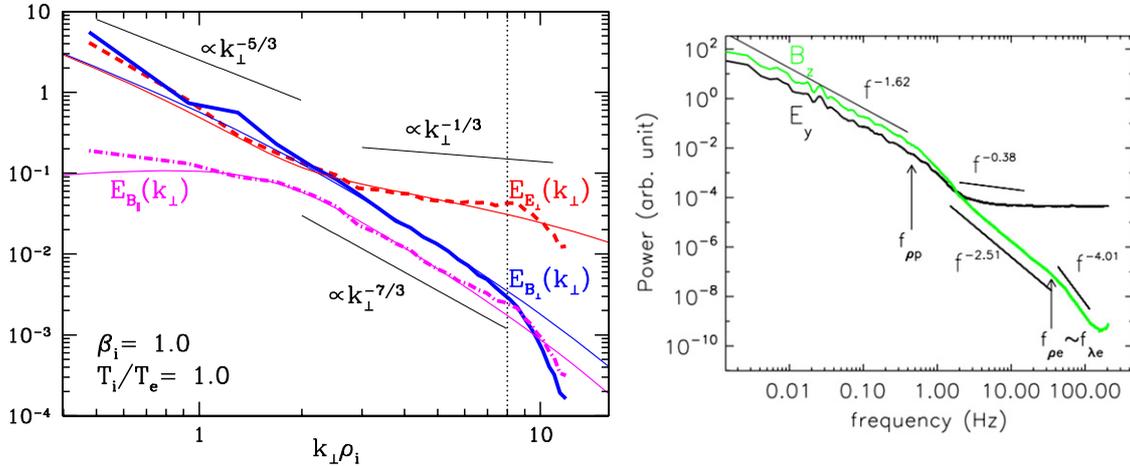
Figure 1. Spectra of electric and magnetic fields from a gyrokinetic simulation [38] (left) compared with those obtained from the Cluster spacecraft [39] (right). Note the approximate $k^{-5/3}$ spectrum below the Doppler-shifted inverse proton Larmor radius and an approximate $k^{-7/3}$ spectrum for the magnetic field (solid/blue on the left and light shaded/green on the right) between the Doppler-shifted inverse proton and electron Larmor radii (in the right-hand plot referred to as $f_{\rho p}$ and $f_{\rho e}$, respectively), followed by a steeper dissipation subrange. Above the inverse Doppler-shifted electron Larmor radius the electric field spectrum develops a shallower subrange consistent with $k^{-1/3}$ (dashed/red on the left and black on the right). Courtesy of Gregory Howes [38], as well as Fouad Sahraoui and Melvyn Goldstein [39].
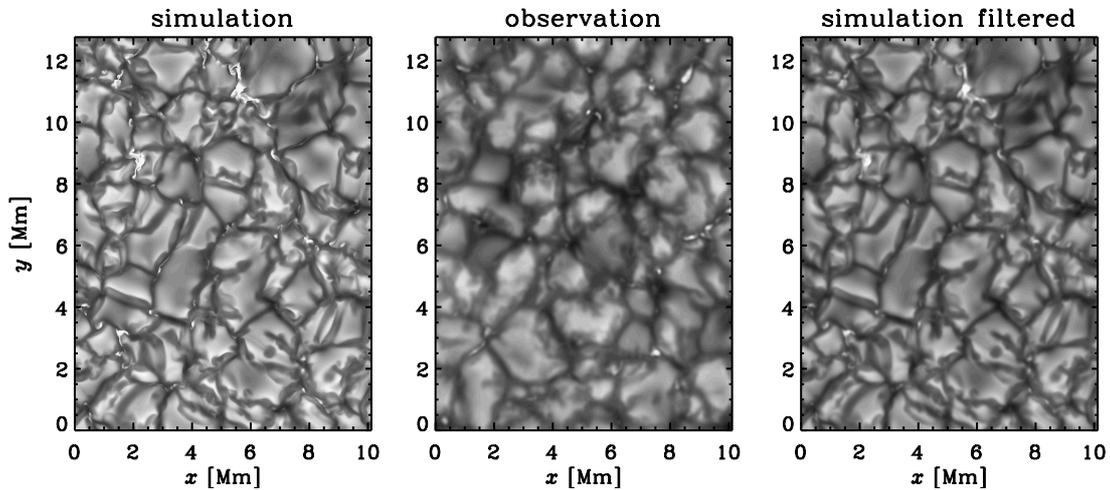

Figure 2. Comparison between a granulation pattern from a simulation with 12 km grid size (left), an observed granulation pattern from the Swedish 1 m Solar Telescope at disk center (middle), and the simulated one after convolving with the theoretical point spread function of a 1 m telescope. The simulation images are for wavelength integrated light intensity while the observed image is for a wavelength band in the near UV. The image was taken on 23 May 2010 at 12:42 GMT with image restoration by use of the multi-frame blind de-convolution technique with multiple objects and phase diversity [48]. Courtesy of V M J Henriques and G B Scharmer.

of chemical elements [49–51]. The chemical element abundances are important for determining the opacity of the gas which, in turn, determines the radial structure of the Sun. This will be discussed in more detail in section 6.10.

From the viewpoint of turbulence theory, this type of convection is special—not so much because the Rayleigh number is extremely large ($\sim 10^{30}$), but mainly because the density and temperature stratifications are extreme, covering 6 orders of magnitude of change in density and a factor of 300 in temperature. This huge stratification implies that the turbulence characteristics become strongly depth-dependent. It has long been anticipated that the energy-carrying scale varies with depth in such a way that it is proportional to the local pressure scale height, H_p. The pressure scale height is proportional to the temperature and varies from about 200 km at the top of the convection zone to about 60 Mm at the bottom.

The typical correlation time of the turbulence is expected to be proportional to the local turnover time, $H_p/u_{\rm rms}$, where $u_{\rm rms}$ is the rms velocity of the turbulence. Estimating the convective energy flux as $F_{\rm conv} \sim \rho u_{\rm rms}^3$, we expect $u_{\rm rms}$ to vary by a factor of 100 from about 4 km s^{-1} at the top of the convection zone to about 40 m s^{-1} at the bottom. Thus, the turnover times vary by more than 4 orders of magnitude, from minutes at the top of the convection zone to about a month at the bottom.

A general difficulty in carrying out simulations of the deep solar convection zone is the long Kelvin–Helmholtz time in deeper layers. The Kelvin–Helmholtz time can be defined as the ratio of thermal energy density to the divergence of the energy flux or (operationally more convenient) as the total thermal energy above a certain layer divided by the solar luminosity. This time scale determines the thermal adjustment time and can be rather long. However, by
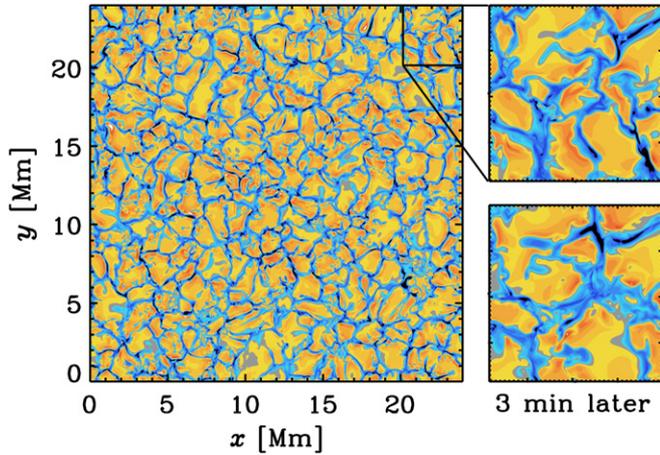
Figure 3. Vertical velocity near the surface from a solar convection simulation. The right-hand panels show part of the domain at two different times.
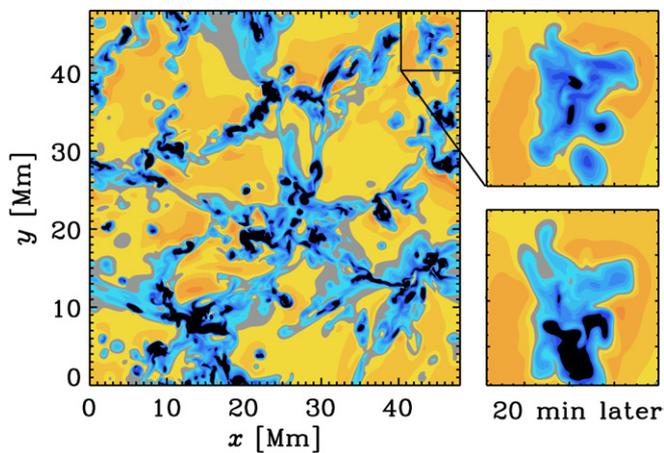
Figure 4. Same as figure 3, but for a deeper level, about 4 Mm away from the surface.

preparing initial conditions such that the mean stratification as well as the fluctuations are close to those in the final state, the difficulty with long time adjustment times can be alleviated.

Figure 3 shows an example from radiation hydrodynamics simulations of the horizontal pattern of the vertical velocity near the surface and figure 4 the same at a depth of about 4 Mm. One sees clearly that the number of cells has decreased and that the horizontal scale of the cells changes from about 2 Mm near the top to about 10 Mm at a depth of about 3 Mm. This illustrates two important properties: (i) The horizontal cell size below the surface is typically a few times the distance from the surface (which really reflects that it is several times the local pressure and density scale heights) and (ii) the structure size increases so rapidly with depth that even using the concept of 'cells' may be misleading. One also sees that the typical cell life time changes rapidly with depth. Near the surface the cell pattern shows some clear changes after only 3 min, while at 4 Mm depth the changes remain more limited even after 20 min. The scales of the patterns and their rates of change are thus generally consistent, at a semi-quantitative level, with the following assumptions that have generally been made in simplified (mixing-length) models of convection.

- The energy-carrying scales of the turbulence are of the order of the local vertical pressure scale height, $H_p = |\nabla \ln p|^{-1}$.
- The turbulence varies on time scales comparable to the turnover time defined as $H_p/u_{\rm rms}$.

One should, however, not conclude that the numerical results 'confirm' a scaling with the pressure scale height. Mass conservation really involves the density scale height rather than the pressure scale height, and the main reason that analytical theories of convection have generally tended to avoid using the density scale height is that, because of a rapid change of the degree of hydrogen ionization there is a narrow layer close to the surface of stars where the density scale height may tend to infinity.

Many of the qualitative expectations from mixing-length theory are borne out by simulations. This also includes the scaling of velocity and the temperature fluctuations with convective flux and hence with depth. Indeed, one finds that the convective energy flux (or enthalpy flux), $F_{\rm conv}$, is proportional to the negative specific entropy gradient. Velocity and temperature fluctuations scale like $F_{\rm conv}^{1/3}$ and $F_{\rm conv}^{2/3}$, respectively; see figure 11 in [52].

Early ideas about distinctively different modes of convection at different scales are mostly due to differences in observational techniques rather than real physical differences in the convection. Supergranulation, for example, refers to a convection pattern with a horizontal scale of about 30 Mm, which is seen in Dopplergrams measuring the line-of-sight velocity. When plotting the horizontal velocity amplitude as a function of horizontal size the supergranulation scales appear to be just a part of a rather featureless power law extending over many orders of magnitude in size [53]. Banana cells, on the other hand, refer to a theoretically expected pattern of convection in deeper layers This expectation is based on the Taylor–Proudman theorem [54], rather than an observationally established fact, but it remains a pronounced feature of convection in rotating shells between $\pm 30°$ latitude [55, 56].

3.3. Other effects of solar turbulence

There are a number of properties that occur on scales that are larger than the energy-carrying scale. These properties include the following.

- The angular velocity varies by about 30% in latitude (slow at the poles and fast at the equator) with approximate solid body rotation below the convection zone and a general deceleration in the outer 5% of the solar radius [57].
- There is a large-scale magnetic field exhibiting a 22 year cycle (11 years for the sunspot number) and a statistical antisymmetry of the radial field with respect to the equator (figure 5).
- The solar surface exhibits a magnetic field that is strongest inside sunspots, where it is seen through Zeeman splitting.
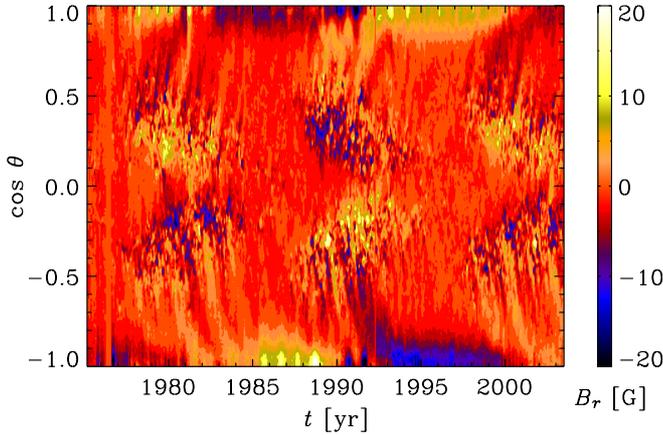
Figure 5. Longitudinally averaged radial component of the observed solar magnetic field as a function of cos(colatitude) and time. Dark/blue shades denote negative values and light/yellow shades denote positive values. Note the sign changes both in time and across the equator. Courtesy of R Knaack.

• Magnetic and current helicity with strong fluctuations, but well-defined averages: negative in the northern hemisphere and positive in the southern hemisphere; see, e.g., figure 1 in [58].

In addition to the convective motions of the Sun, there are coherent wave patterns that correspond to discrete frequencies in wavenumber and frequency space. Using a technique called helioseismology [59–62], the information contained in these modes can be used to infer the depth dependence of sound speed and hence the radial dependence of the temperature of the Sun.

Helioseismic constraints of the core temperature were important in pinning down the origin of the low observed neutrino flux from the Sun [63–65] in terms of neutrino oscillations, i.e. the Mikheyev–Smirnov–Wolfenstein effect [66, 67].

Solar rotation lifts the degeneracy of modes with different azimuthal order and allows a determination of the dependence of the internal angular velocity on radius and latitude [57]. Rotation also causes the convection pattern to propagate in a prograde direction [68].

At the equator, the Sun rotates with a period of about $t_{rot} = 26$ d, but at the poles it spins about 30% slower. This is referred to as differential rotation. The angular velocity is $\Omega = 2\pi/t_{rot}$, but in helioseismology one often talks about the rotation rate, $\Omega/2\pi$, which is measured in nHz. The equatorial value at the surface is 452 nHz. The radiative interior is found to rotate rigidly [57]. The interface between the differentially rotating convection zone and the rigidly rotating radiative interior is referred to as the tachocline [69, 70].

3.4. Interstellar turbulence

The gas between the stars can be observed in absorption or emission both at infrared and radio wavelengths. The line-of-sight velocity component can be determined by Doppler shifts of spectral lines; see, e.g., [71]. There is a general power law scaling of velocity amplitudes and velocity differences with

geometrical scale [71–73]. Velocity dispersions scale with size to a power of about 0.4 from sub-parsec scales to scales of the order of about 1 kpc; see figure 1 of [72]. The velocity scaling is practically the same in regions with varying intensities of star formation, indicating that the velocity scaling is inertial, and driven mostly by energy input at large scales, rather than a result of direct, local driving by on-going star formation [74–76]. Direct evidence of turbulence on small length scales ($\sim 10^{12}$ cm) in the ISM comes from radio scintillation measurements [77, 78].

Galaxies such as our own have typical radii of $R \approx 15$ kiloparsecs (kpc). Here, $1 \, \text{kpc} = 3 \times 10^{21}$ cm is used as a convenient length scale. The density decreases rapidly away from the midplane with a typical density scale height of $H \approx 70$ pc. Near the midplane of a typical galaxy the 3D rms turbulent velocities are around 15 km s^{-1}. This implies a typical turnover time, H_p/u_{rms}, of around 5 Myr (megayears).

An important aspect is the occurrence of supernovae, which mark the death of massive stars and provide a significant energy release into the interstellar medium through thermal energy and momentum injection. Traces of supernovae are seen as supernova remnants, which give a qualitative idea about the nature of interstellar turbulence.

Supernova explosions contribute about $E_{SN} = 10^{51}$ erg per explosion. With about 20 supernovae per million years per kpc^2 estimated for the solar neighborhood this corresponds to an energy injection per unit area of

$$\int \epsilon_{SN} \, dz \approx 20 \times 10^{51} \, \text{erg}/(3 \times 10^{13} \, \text{s} \times 9 \times 10^{43} \, \text{cm}^2)$$

$$\approx 7 \times 10^{-5} \, \text{erg cm}^{-2} \, \text{s}^{-1}. \tag{21}$$

This is almost two orders of magnitude more that what is required to sustain the turbulent energy dissipation per unit area and time, which, from equation (19), may be estimated to be

$$\int \epsilon \, dz \approx 0.5 \, \rho u_{1D}^3 \approx 10^{-24} \, \text{g cm}^{-3} \, (10^6 \, \text{cm s}^{-1})^3$$

$$\approx 10^{-6} \, \text{erg cm}^{-2} \, \text{s}^{-1}, \tag{22}$$

where the mean density of the interstellar medium is $\rho \approx 2 \times 10^{-24}$ g cm^{-3} and the one-dimensional rms velocity is $u_{1D} \approx 10 \, \text{km s}^{-1} = 10^6 \, \text{cm s}^{-1}$. This is also in good agreement with simulations [79]. A visualization of density and magnetic field strength in such a simulation is shown in figure 6.

The linear polarization properties of synchrotron radiation can be used to infer the magnetic field both along the line of sight via Faraday rotation and perpendicular to it through the polarization plane projected onto the sky [80–82]. The field strength is typically around 5 μG in the solar neighborhood of our Galaxy, but it can be several mG in the galactic center [83, 84]. For many spiral galaxies large-scale magnetic fields have been found. In many of them the magnetic field is approximately axisymmetric and symmetric about the midplane [85].
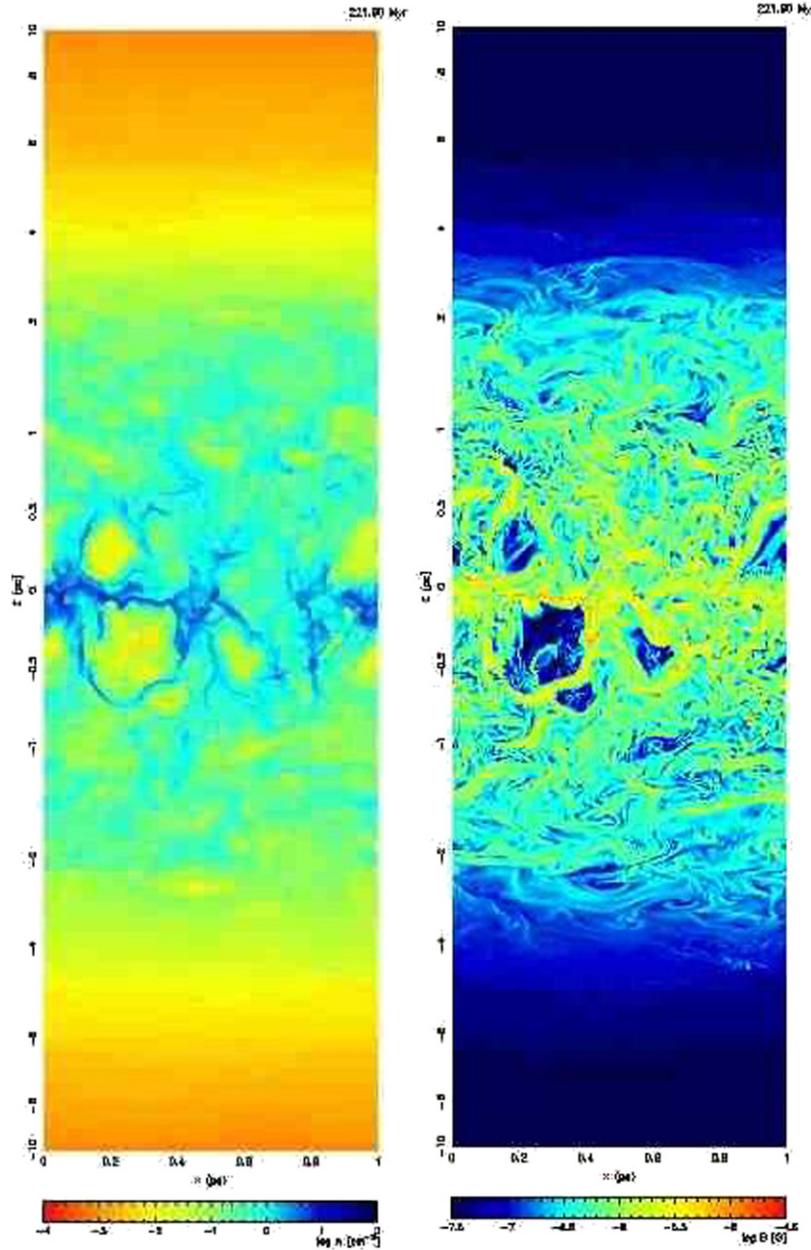
Figure 6. Two-dimensional slices through a three-dimensional simulation domain of supernova-driven turbulence in the interstellar medium showing the vertical distribution of the density (left) and magnetic field (right). Note the appearance of supernova remnants in density and magnetic fields as well as an overall concentration around the midplane at $z = 0$. Courtesy of Miguel de Avillez [79].

3.5. Accretion disks

Accretion disks are disk-like structures through which gas gradually spirals toward a central massive object while converting potential energy into kinetic and magnetic energies that are dissipated and radiated away. This conversion is believed to be of turbulent nature and may be driven by the magneto-rotational instability [31, 86]. An alternative mechanism for disk dissipation is that the disk functions as a self-regulating buffer. As long as the disk accretion toward the central object is smaller than the rate of mass in-fall onto the disk from the surrounding nebula, the mass density of the disk increases. When the surface density reaches a level sufficient for gravitationally driven instabilities to develop, spiral waves start to grow, develop into spiral shocks, and dissipation in the

shocks then enhances the disk accretion enough to balance the rate of in-fall onto the disk [87].

In order to allow material to spiral inward at a mass accretion rate $\dot{M}$, half of the orbital potential energy must be converted viscously and resistively into heat and radiation. Therefore, the total (bolometric) luminosity of an accretion disk is [88]

$$L = \frac{GM\dot{M}}{2R_{in}}, \tag{23}$$

where M is the mass of the central object and R_{in} is the inner radius of the accretion disk. Obviously, the further the disk stretches toward the central object, i.e. the smaller the value of R_{in}, the more efficient the energy conversion will be. Disks around black holes are most efficient in this respect, because

here the innermost stable orbit is 1–3 Schwarzschild radii, i.e. $(2–6) \times GM/c^2$, where c is the speed of light. Thus, $L = 0.1 \times \dot{M}c^2$, which constitutes a much more efficient conversion than nuclear fusion, where the efficiency is only $0.007 \times \dot{M}c^2$. Here we have used for $\dot{M}$ the rate of hydrogen burning [88]. Note that the factor 0.007 comes from the relative mass difference between a helium atom (4.0026) and four hydrogen atoms (1.0078).

3.6. Turbulence in galaxy clusters

Galaxies themselves tend to cluster on Mpc scales. There are typically around 10^4 galaxies in a cluster, but some clusters can be substantially smaller. All clusters are generally strong x-ray emitters, but some are also strong radio-emitters resulting from synchrotron emission in the presence of magnetic fields.

Typical temperatures are around 10^8 K corresponding to a sound speed of around $1000 \, \text{km s}^{-1}$. The implied velocity dispersion is also of that order, as expected when the system is in approximate virial equilibrium. With typical length scales on the order of the density scale height, $H_\rho = 100 \, \text{kpc}$, the turnover time is $100 \, \text{kpc}/(1000 \, \text{km s}^{-1}) = 0.1 \, \text{Gyr}$. This would also be the typical decay time of the turbulence in the absence of mechanisms driving the turbulence.

Mechanisms for driving such turbulence include mutual encounters of clusters [89, 90]. Given that only a fraction of all galaxy clusters also have strong radio halos [91], one may speculate that these clusters have undergone a recent encounter or merger with another cluster within the last few gigayears. Obviously, in this scenario one would just have decaying turbulence between encounters. In the context of galaxy clusters this subject has been studied by various groups [92–94]. Another mechanism that has been discussed in the literature is the driving by individual galaxies moving through the cluster and producing a turbulent wake behind them [95–97].

3.7. Decaying turbulence in the early universe

Various mechanisms for the generation of 'primordial' fields have been proposed [98]. One problem is that the predicted magnetic field strengths are extremely uncertain. Another general problem is the small length scale of such fields. For example, after the electroweak phase transition, about 10^{-10} s after the Big Bang, the horizon scale was around 3 cm. Magnetic fields generated during such a phase transition may possess magnetic helicity, but this is also rather uncertain [99]. However, during the subsequent decay of a helical field, energy is transformed to larger scale by an inverse cascade of magnetic helicity [100, 101]. Figure 7 shows the evolution of the resulting magnetic power spectrum at different times from a direct numerical simulation of the relevant hydromagnetic equations [102]. Simulations have demonstrated that turbulence decays in power law fashion with the total energy being proportional to t^{-n}, where $n = 0.5$ for maximally helical fields and $n = 1$ for non-helical fields [102]. By comparison, non-helical fluid turbulence leads to $n = 1.2$ [103, 104]. As argued by Biskamp and Müller [105], helical fields may be more typical than non-helical ones. Of
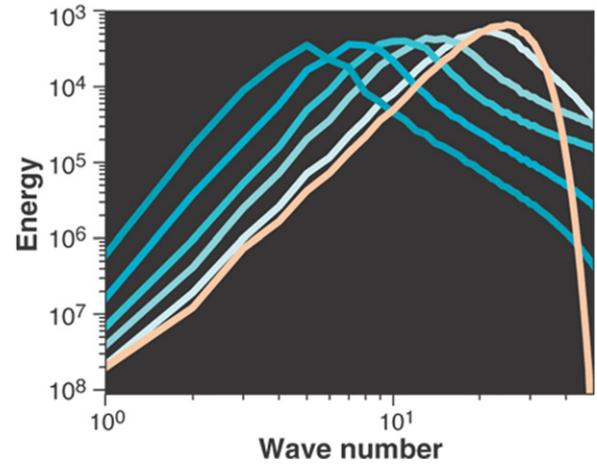
Figure 7. Magnetic energy spectra at different times (increasing roughly by a factor of 2). The curve with the right-most location of the peak corresponds to the initial time, while the other curves refer to later times (increasing from right to left). Note the temporal growth of spectral magnetic energy at wavenumbers to the left of the peak and the associated propagation of spectral energy to successively smaller wavenumbers, i.e. to successively larger scales. Adapted from [101, 102].

course, the magnetic fields generated in rotating bodies (stars and galaxies, although neither is relevant to the early Universe) tend to be helical, but of opposite sign in the two hemispheres, so the net magnetic helicity would cancel to zero. On the other hand, the helical contribution of a field generated at an early phase transition will decay more slowly than the non-helical contribution, and so the *relative* importance of the helical fields will grow with time.

The question of the decay law of helical MHD turbulence is still not fully settled. It is generally believed that the magnetic energy, E_M, follows a power law decay, i.e. $E_M \sim t^{-n}$, but proposals for the value of n range from 2/3 to 1/2, depending essentially on the assumptions made about the evolution of the typical length scale L of the energy-carrying motions. If one assumes L to be controlled by a resistive evolution of magnetic helicity, H_M, i.e.

$$-\frac{dH_M}{dt} = \frac{2\eta}{L^2} H_M, \qquad (24)$$

then, for a power law evolution of H_M we have $L \sim t^{1/2}$, and with $E_M = H_M/L$ and $H_M \approx \text{const}$ we find [106],

$$E_M \sim t^{-1/2}. \qquad (25)$$

On the other hand, if one discards resistive effects, and assumes instead that the decay is controlled by inertial range turbulence, i.e.

$$-\frac{dE_M}{dt} \equiv \epsilon \sim \frac{U^3}{L} \sim \frac{E_M^{3/2}}{L} \sim \frac{E_M^{5/2}}{H_M}, \qquad (26)$$

then, after integration, we obtain [105]

$$E_M \sim t^{-2/3}, \qquad (27)$$

together with $L \sim t^{2/3}$. Note that in either of the two proposals one has assumed that $H_M \sim L E_M \approx \text{const}$. However, in the

former approach $H_{\rm M}$ is not assumed to be constant exactly, but to decay resistively like $H_{\rm M} \sim t^{-2\eta t/L^2}$, which implies a corresponding speed-up of the decay of $E_{\rm M}$ and hence an increase in n from $1/2$ to $1/2 + 2\eta t/L^2$. This may explain why simulations at finite η [105, 107] suggest exponents close to $n = 2/3$. This question needs to be followed up again in future at higher resolution, but simulations at moderate resolution have confirmed the idea of a correction factor proportional to $t^{-2\eta t/L^2}$ in the decay of $E_{\rm M}$ [106].

It is still unclear whether such primordial magnetic fields would have a detectable effect on the polarization signal of the cosmic background radiation and whether significant fields may have been present when the first stars or galaxies were formed. These questions are subject to current investigations [108, 109]. Another subject under active investigation concerns the production of gravitational waves from the Maxwell stress associated with primordial magnetic fields [110–113].

4. Theoretical studies of turbulence

4.1. Incompressible turbulence

Most turbulence research is restricted to incompressible turbulence, in which case the Navier–Stokes equations take the form

$$\frac{{\rm D}\boldsymbol{u}}{{\rm D}t} = -\boldsymbol{\nabla}\tilde{p} + \boldsymbol{f} + \nu\nabla^2\boldsymbol{u}, \qquad \boldsymbol{\nabla}\cdot\boldsymbol{u} = 0. \quad (28)$$

Here, ${\rm D}/{\rm D}t = \partial/\partial t + \boldsymbol{u}\cdot\boldsymbol{\nabla}$ denotes the advective derivative. It is this term that constitutes the important nonlinearity of the Navier–Stokes equations. In order to understand the nature of the nonlinearity it is useful to make use of the vector identity $\boldsymbol{u}\cdot\boldsymbol{\nabla}\boldsymbol{u} = \boldsymbol{\omega}\times\boldsymbol{u} + \frac{1}{2}\boldsymbol{\nabla}u^2$, with $\boldsymbol{\omega} = \boldsymbol{\nabla}\times\boldsymbol{u}$. Thus, we have

$$\frac{\partial\boldsymbol{u}}{\partial t} = \boldsymbol{u}\times\boldsymbol{\omega} - \boldsymbol{\nabla}\tilde{p} + \boldsymbol{f} + \nu\nabla^2\boldsymbol{u}. \quad (29)$$

Owing to incompressibility, we have $\rho = $ const, and only the reduced pressure, $\tilde{p} = p/\rho + \frac{1}{2}\boldsymbol{u}^2$, enters in equation (29). However, because of the solenoidality constraint, $\boldsymbol{\nabla}\cdot\boldsymbol{u} = 0$, the pressure gradient also constitutes a quadratic nonlinearity of the form

$$\tilde{p} = \nabla^{-2}\boldsymbol{\nabla}\cdot(\boldsymbol{u}\times\boldsymbol{\omega} + \boldsymbol{f}). \quad (30)$$

This relation follows directly from equation (29) after taking its divergence and noting that $\boldsymbol{\nabla}\cdot\partial\boldsymbol{u}/\partial t = \boldsymbol{\nabla}\cdot\nabla^2\boldsymbol{u} = 0$.

4.2. Compressible fluid dynamics

In the compressible case, the Navier–Stokes equation can be written in the form

$$\rho\frac{{\rm D}\boldsymbol{u}}{{\rm D}t} = -\boldsymbol{\nabla}p + \boldsymbol{F} + \boldsymbol{\nabla}\cdot\boldsymbol{\tau}, \quad (31)$$

where $\boldsymbol{\tau} = 2\rho\nu\mathbf{S}$ is the stress tensor, here assumed to be proportional to the kinematic viscosity ν and the traceless rate of strain tensor, $\mathbf{S}$, whose components are

$$\mathsf{S}_{ij} = \tfrac{1}{2}(u_{i,j} + u_{j,i}) - \tfrac{1}{3}\delta_{ij}\boldsymbol{\nabla}\cdot\boldsymbol{u}, \quad (32)$$

where commas denote partial differentiation. Note that the form of the stress tensor above applies only to a monatomic gas. In more general cases there may be additional contributions from the bulk viscosity corresponding to terms proportional to $\delta_{ij}\boldsymbol{\nabla}\cdot\boldsymbol{u}$.

To compare with the incompressible case, we evaluate

$$\frac{1}{\rho}\boldsymbol{\nabla}\cdot\boldsymbol{\tau} = \nu\left[\nabla^2\boldsymbol{u} + \frac{1}{3}\boldsymbol{\nabla}\boldsymbol{\nabla}\cdot\boldsymbol{u} + 2\mathbf{S}\cdot\boldsymbol{\nabla}\ln(\rho\nu)\right], \quad (33)$$

and note that, in addition to the $\nabla^2\boldsymbol{u}$ term, there is also a term $\boldsymbol{\nabla}\boldsymbol{\nabla}\cdot\boldsymbol{u}$, which vanishes in the incompressible case, and a term $\mathsf{S}_{ij}\nabla_j\ln(\rho\nu)$, which vanishes when the dynamical viscosity, $\mu = \rho\nu$, is constant.

Equation (31) has to be solved together with the continuity equation

$$\frac{{\rm D}\rho}{{\rm D}t} = -\rho\boldsymbol{\nabla}\cdot\boldsymbol{u}, \quad (34)$$

and an energy or entropy equation,

$$\rho T\frac{{\rm D}s}{{\rm D}t} = 2\nu\rho\mathbf{S}^2. \quad (35)$$

The heating term is generally given by $u_{i,j}\tau_{ij}$. Splitting $u_{i,j} = s_{ij} + a_{ij}$ into symmetric and antisymmetric parts, it is clear that only s_{ij} contributes after multiplying with another symmetric matrix, i.e. with τ_{ij}. Furthermore, since τ_{ij} is also trace-free, the result does not change when adding or subtracting from s_{ij} a term proportional to δ_{ij}, in particular $\frac{1}{3}\delta_{ij}\boldsymbol{\nabla}\cdot\boldsymbol{u}$. Therefore, we have $u_{i,j}\tau_{ij} = 2\rho\nu\mathbf{S}^2$, which is manifestly positive definite.

For a perfect gas the specific entropy s is related to pressure and density via

$$s = c_v\ln p - c_p\ln\rho + s_0, \quad (36)$$

where s_0 is an additive constant. (The specific entropy s is not to be confused with s_{ij} or S_{ij}.) It is important to realize that even in the inviscid limit, $\nu\to 0$, the term $2\nu\rho\mathbf{S}^2$ cannot be neglected in equation (35). For example, across a shock there is always a well-defined increase in specific entropy that is independent of the value of ν.

In compressible fluid dynamics it is often advantageous to consider the evolution equations in their conservative form. This means that the rate of change of the density of a conserved quantity, X, is given by the negative divergence of its corresponding flux, i.e.

$$\frac{\partial}{\partial t}(\text{density of } X) = -\boldsymbol{\nabla}\cdot(\text{flux density of } X)$$
$$+ \text{sources} - \text{sinks}, \quad (37)$$

where the presence of sources and sinks indicates additional processes whose detailed evolution is not captured by the total energy equation within the same framework. An example is radiation, which provides sources and sinks to the energy equation as heating and cooling terms. Alternatively, if the evolution of the radiation energy is included in the total energy equation, any explicit heating and cooling terms disappear, and only boundary (flux divergence) terms remain [114]. If

there is no radiation, gravity, external forcing, etc, there are no additional terms, so the conservative form of the equations is

$$\frac{\partial \rho}{\partial t} = -\frac{\partial}{\partial x_j}(\rho u_j), \tag{38}$$

$$\frac{\partial}{\partial t}(\rho u_i) = -\frac{\partial}{\partial x_j}(\rho u_i u_j + \delta_{ij} p - \tau_{ij}), \tag{39}$$

$$\frac{\partial}{\partial t}\left(\rho e + \frac{1}{2}\rho \boldsymbol{u}^2\right) = -\frac{\partial}{\partial x_j}\left(\rho u_j h + \frac{1}{2}\rho u_j \boldsymbol{u}^2 - u_i \tau_{ij}\right), \tag{40}$$

where $h = e + p/\rho$ is the specific enthalpy per unit mass. For a perfect gas, h and e are proportional to temperature with $h = c_p T$ and $e = c_v T$, where c_p and c_v are the specific heats at constant pressure and constant volume, respectively.

The equations above show explicitly that the volume integrals of the terms under the time derivative are conserved, i.e. constant in the absence of fluxes in or out of the domain. In one dimension, the terms in parentheses under the spatial derivatives are constant and, in particular, uniform across a shock. This allows shock jump conditions to be derived. Note that, since viscosity acts only locally, these conditions are independent of the width of the shock. This is an important property that allows simulating highly supersonic turbulence using a modified viscosity (Neumann–Richtmyer artificial viscosity) for smearing out the shock [115]. In the presence of source or sink terms in equations (38)–(40) this would no longer be possible.

4.3. Anelastic approximation

The advantage of making the assumption of incompressibility is not only that one has one equation less to solve (the $\partial \rho/\partial t$ equation), but mainly that one eliminates sound waves, whose associated wave speed is often much faster than the speed associated with other processes. This means that one can then focus more efficiently on the slower dynamics of the system.

Incompressibility is normally associated with constant density. In view of our earlier discussion regarding the strong density stratification in stars, incompressibility would not be a useful assumption, even though the sound speed can be much larger than other speeds such as that associated with the convection itself. It is then better to relax the condition $\boldsymbol{\nabla} \cdot \boldsymbol{u} = 0$ and use instead $\boldsymbol{\nabla} \cdot \rho \boldsymbol{u} = 0$. This is called the anelastic approximation [116, 117]. It is important to realize that with this assumption one *replaces* the original continuity equation (38). Consequently this equation can then no longer be used to argue that $\partial \rho/\partial t = 0$. Indeed, ρ is in general not constant in time and can evolve, while $\boldsymbol{\nabla} \cdot \rho \boldsymbol{u} = 0$ is maintained at all times. This technique is sometimes used in simulations of solar convection [55, 118–122].

Just like in the incompressible case, also here one has to solve a Poisson-like equation that emerges when taking the divergence of the evolution equation for the momentum density. Taking the divergence of equation (39) one obtains

$$\nabla^2 p = \boldsymbol{\nabla} \cdot \boldsymbol{R}, \tag{41}$$

where $\boldsymbol{R} = -\rho \boldsymbol{u} \cdot \boldsymbol{\nabla} \boldsymbol{u} + \boldsymbol{F} + \boldsymbol{\nabla} \cdot \boldsymbol{\tau}$ is the sum of the advection term plus all the other terms on the right-hand side of equation (39), except for the pressure gradient term. The $\boldsymbol{F}$ term in equation (41) refers to additional terms such as gravity and Lorentz force terms in equation (31).

The anelastic approximation is sometimes associated with linearizing the equation of state [55]. However, this is not necessary and one can just continue working with the original, fully nonlinear equation of state [119, 123]. The only difference is that in the fully compressible case one would obtain the pressure from density and specific entropy, while in the anelastic case one obtains the density from pressure and specific entropy, if the latter is indeed the main thermodynamic variable.

4.4. Large-eddy and hyperviscous simulations

The maximum achievable Reynolds number scales as the number of mesh points in one direction, raised to the power 4/3; see equation (11). With the largest attainable resolution being at present 4096^3 [18], it is impossible to reach Reynolds numbers of 10^6 and beyond. In many engineering applications of turbulence one needs to calculate flows at very large Reynolds numbers and one therefore uses large-eddy simulations. This involves some representation of the unresolved Reynolds stress in terms of other flow variables. This approach can be rather uncertain. Unlike engineering applications, where such models can be tested against measurements, this is usually not possible in astrophysics, due to a large number of additional complications (strong stratification, magnetic fields, rotation, etc) that are hard to realize in the laboratory. The best one can therefore hope for is a rigorous comparison of large-eddy simulations with DNS. Examples of this are discussed in section 6.

One of the simplest subgrid scale models is the Smagorinsky model [124]. This approach is strictly dissipative, i.e. the Reynolds stress of the unresolved velocity fluctuations, denoted here by primes, is modeled by a viscous stress of the form

$$\overline{u_i' u_j'} = -2(C_S \Delta x)^2 \rho |\mathsf{S}| \mathsf{S}_{ij}, \tag{42}$$

where C_S is the Smagorinsky constant (between 0.1 and 0.2) [125–127], and the rate-of-strain tensor S was defined in equation (32), and is here applied to the resolved motions $\overline{\boldsymbol{u}}$, i.e. excluding the subgrid scale motions. Another approach, which cannot be classified as large-eddy simulation, consists in using hyperviscosity. In spectral space, the viscosity operator $-\nu k^2$ is simply replaced by $-\nu_n k^{2n}$, where $n > 1$ is the order of hyperviscosity. Unlike the Smagorinsky model, the results from this approach are known not to converge to the original Navier–Stokes equations, but the hope is that in the inertial range the flow is unaffected by the unphysical form of the diffusion operator. This is indeed the case, as was demonstrated in [104].

4.5. Turbulence simulations using Godunov/PPM-type schemes

The Godunov scheme is a conservative numerical scheme for solving partial differential equations. In this method, the

conservative variables are considered as piecewise constant over the mesh cells at each time step and the time evolution is determined by the exact solution of the Riemann shock tube problem at the intercell boundaries. This scheme consists of first defining a piecewise constant approximation of the solution at the next time step. The resulting scheme is usually first-order accurate in space. This approximation corresponds to a finite volume method representation whereby the discrete values represent averages of the state variables over the cells. Exact relations for the averaged cell values can be obtained from the integral conservation laws. Next, the solution for the local Riemann problem is obtained at the cell interfaces. This is the only physical step of the whole procedure. The discontinuities at the interfaces are resolved as a superposition of waves satisfying locally the conservation equations. The original Godunov method is based upon the exact solution of Riemann problems. However, approximate solutions can be applied as an alternative. Finally, the state variables are averaged after one time step. The state variables obtained after the second step are averaged over each cell defining a new piecewise constant approximation resulting from the wave propagation during the time step.

Nowadays one uses often higher-order Godunov schemes for astrophysical applications. One such method is the piecewise parabolic method that is also referred to as PPM. Examples of such codes include Athena [128], Pluto [129], Nirvana [130], Ramses [131], Flash [132], and Enzo [133]. Such codes have been used for many astrophysical applications including supersonic, isotropic homogeneous turbulence [134].

4.6. Analyzing and modeling turbulence with wavelets

Wavelets are sometimes used both to analyze and to model turbulence. In particular the wavelet technique has been used for extracting coherent vortices out of turbulent flows. The aim is to retain only the essential degrees of freedom responsible for the transport. It is intriguing that with this technique one can actually retain nearly all velocity structure and dissipation information in turbulent flows using a relatively small selection of wavelets with non-zero amplitudes [135]; see also [136]. This method is related to the so-called proper orthogonal decomposition of turbulent flows [137]. This decomposition is statistically based and permits the extraction of spatio-temporal structures that are judged essential according to predetermined criteria. It is not only useful in the analysis and synthesis of data from simulations and experiments, but it also allows the construction of low-order models from the Navier–Stokes equations. Finally, let us note that the wavelet representation has been applied with success to simulations of resistive drift-wave turbulence in magnetized plasma Hasegawa–Wakatani system [138].

5. Extra ingredients to turbulence in astrophysical flows

5.1. Passive scalars: mixing and dust dynamics

One of the simplest additional ingredients in fluid dynamics in general, and in turbulence physics in particular, are passive scalars. The passive scalar concentration per unit mass, θ, is governed by the equation

$$\frac{\partial}{\partial t}(\rho\theta) = -\frac{\partial}{\partial x_j}\left(\rho u_j\theta - \rho\kappa_\theta\frac{\partial\theta}{\partial x_j}\right), \qquad (43)$$

where κ_θ is a diffusion coefficient for the passive scalar concentration. This equation describes the transport of chemicals in a gas. Additional source and sink terms could be included to model production and destruction of chemicals. The non-conservative form of this equation can be written as

$$\frac{\mathrm{D}\theta}{\mathrm{D}t} = -\frac{1}{\rho}\boldsymbol{\nabla}\cdot(\rho\kappa_\theta\boldsymbol{\nabla}\theta), \qquad (44)$$

where we have made use of the continuity equation (34). For $\kappa_\theta = 0$, this equation gives $\mathrm{D}\theta/\mathrm{D}t = 0$, which shows that the concentration per unit mass is unchanged at each point comoving with the flow.

Another class of scalars are inertial particles that are advected by their own velocity $\boldsymbol{u}_\mathrm{p}$ rather than the velocity of the gas $\boldsymbol{u}$. The evolution equation of $\boldsymbol{u}_\mathrm{p}$ is similar to that of $\boldsymbol{u}$, except that it lacks the pressure gradient term and the Lorentz force. However, such particles are strictly speaking active particles, because of the mutual coupling between the two velocity fields. Only in the limit of sufficiently light particles can the back-reaction on $\boldsymbol{u}$ be neglected.

In astrophysics one often finds the condensation of heavier elements into solid dust. Their evolution is described as a passive scalar or as passively advected particles. The inclusion of inertia can sometimes become important, because inertial particles have a tendency to accumulate in anti-cyclonic vortices [139–143].

5.2. Active scalars: stratification and convection

In this context, the term 'active' refers to the property that the scalar quantity can affect the momentum equation, for example by exerting a pressure gradient force. An example is the advection–diffusion equation for the energy density of low-energetic cosmic rays [144, 145]. Another example concerns temperature or specific entropy, which affect the momentum equation by locally changing the relation between pressure and density. In the presence of a gravity force, $\boldsymbol{F} = \rho\boldsymbol{g}$, this can lead to an Archimedian buoyancy force. Furthermore, with $\boldsymbol{g} \neq 0$ a new wave mode can exist known as gravity waves (not to be confused with gravitational waves of the space–time metric in general relativity; see comment at the end of section 3.7). The restoring force comes from the linearized buoyancy term, $(\delta\rho/\rho_0)g \approx (\delta p/p_0 + \delta s/c_p)g$. Since the restoring force is related to gravity, these wave modes are often referred to as g-modes, in contrast to p-modes or sound waves, whose restoring force is related to the pressure gradient. If pressure fluctuations may be neglected the essential terms are

$$\frac{\partial u_z}{\partial t} = \cdots + \delta s\ g/c_p, \qquad (45)$$

$$\frac{\partial\delta s}{\partial t} = \cdots - u_z\frac{\partial\overline{s}}{\partial z}, \qquad (46)$$
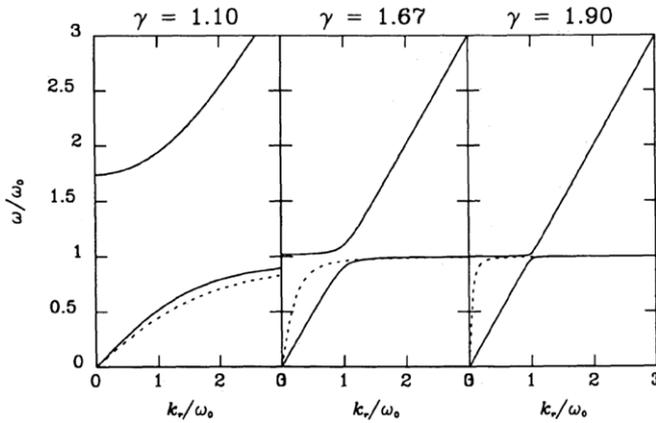
Figure 8. Dispersion relation $\omega = \omega(k_r)$, for $k_z = 0$ with $k_r = (k_x^2 + k_y^2)^{1/2}$ being the horizontal wavenumber, for different values of the ratio of specific heats, γ, showing p-modes branch (upper branch) and g-models (lower branch) compared with the case where the anelastic approximation has been made (dashed line). Length is given in units of $H_0 = \gamma H_p/(1 - \gamma/2)$ and time in units of $T_0 = H_0/c_s$, and $\omega_0 = \sqrt{\gamma - 1}/(1 - \gamma/2)$ is the non-dimensional Brunt–Väisälä frequency. In the plot, the break point at $k_r/\omega_0 = 1$ corresponds to a critical horizontal wavelength of $\ell_{crit} = 2\pi\gamma H_p/\sqrt{\gamma - 1}$. For $\gamma = 5/3$ this means $\ell_{crit} \approx 12.8\,H_p$. Adapted from [147].

where $\bar{s}$ denotes the specific entropy of the background stratification. The oscillation frequency N_{BV} (for Brunt–Väisälä frequency) is given by

$$N_{BV}^2 = -\boldsymbol{g} \cdot \boldsymbol{\nabla}\bar{s}/c_p. \tag{47}$$

While this pair of equations represents the basic feedback loop correctly, it ignores the fact that buoyancy is only possible when there is lateral non-uniformity of density. Indeed, solving the proper dispersion relation reveals that on large scales the frequency increases linearly with wavenumber; see, e.g., [146] for a review. In figure 8 we show the dispersion relation as a function of the horizontal wavenumber, $k_r = (k_x^2 + k_y^2)^{1/2}$, for $k_z = 0$ and different values of the ratio of specific heats ranging from $\gamma = 1.1$ to 1.9. The p-modes correspond to the upper branch while the g-modes to the lower one. Also shown are the g-modes obtained using the anelastic approximation discussed in section 4.3. Note that this approximation yields correct results for γ close to one and for large horizontal wavenumbers, i.e. on scales that are small compared with the pressure scale height [147].

Given that gravity points downward, N_{BV}^2 is positive (i.e. the frequency is real) when the specific entropy increases in the upward direction. If it decreases with height, the system is unstable to the onset of convection with an approximate growth rate given by $\text{Im}|N_{BV}|$. Here we have omitted viscous and diffusive effects that could slow down the growth and even stabilize the system. This is quantified by the value of the Rayleigh number that will be defined and discussed in more detail in section 6.7. However, in astrophysics viscosity and diffusivity are comparatively small and one uses just the condition $\boldsymbol{g} \cdot \boldsymbol{\nabla}\bar{s} > 0$ for instability. This is known as the Schwarzschild criterion and corresponds to saying that the Rayleigh number is positive (convection is discussed in more detail in section 6.7).

In the presence of strong vertical density stratification, the convection flow tends to develop an interconnected network of downdraft lanes, with isolated tube-like stronger downdrafts at network vertices. With depth, the downdrafts merge and the network size increases [148]; cf also figures 3 and 4. At large Reynolds numbers the flow is of course turbulent, but with the intensity of turbulence strongly influenced by stratification effects: Because ascending flows are strongly divergent, turbulence is suppressed there, while in downflows, which are converging, turbulent intensity is enhanced.

In the Sun, the Prandtl number, $Pr = \nu/\chi$, is far below unity (around 10^{-5}). This means that velocity or vorticity structures can be much thinner than temperature structures. As a consequence, thin vortex tubes can develop within downdrafts. The dynamical pressure associated with vortex tubes allows locally a lower gas pressure and hence a lower density, making vortex tubes buoyant. As a result, the downdraft speed is slowed down ('vortex braking') [149, 150]. This is a particular property of low Prandtl number dynamics which, at the same time, requires compressibility.

Compressibility leads to yet another interesting effect in convection. The pressure gradient associated with driving the horizontal expansion of upwelling motions works in all directions, and in particular also in the downward direction. This tends to brake the upwellings. This phenomenon is known as buoyancy braking [151].

Another important effect caused by compressibility is the production of vorticity by the baroclinic term, i.e. the curl of $\rho^{-1}\boldsymbol{\nabla}p$. The curl of this term is finite if the surfaces of constant ρ and p are inclined relative to each other. Another way of writing this term is using the thermodynamic relation for the differential of enthalpy, $dH = T\,dS + V\,dp$. With this we can write the pressure gradient term in terms of specific enthalpy, specific entropy s and specific volume ρ^{-1} as

$$-\rho^{-1}\boldsymbol{\nabla}p = -\boldsymbol{\nabla}h + T\boldsymbol{\nabla}s. \tag{48}$$

This formula shows that the baroclinic term is just given by

$$\boldsymbol{\nabla} \times \left(-\rho^{-1}\boldsymbol{\nabla}p\right) = \boldsymbol{\nabla}T \times \boldsymbol{\nabla}s. \tag{49}$$

This relation will become useful later in connection with the Taylor–Proudman theorem and ideas to understanding departures from it. The baroclinic term vanishes under isothermal ($T = $ const), isentropic (s = const) or barotropic [$p = p(\rho)$] conditions. In all these cases, equation (48) can be written purely as a gradient term, $-\boldsymbol{\nabla}\tilde{h}$, where $\tilde{h}$ is then called the pseudo-enthalpy and it is proportional to h which, in turn, is proportional to the temperature. In the irrotational case, $\boldsymbol{\omega} = \boldsymbol{0}$, the only nonlinearity comes from the $\frac{1}{2}u^2$ term in the reduced pressure.

5.3. Rotation and shear

It is often convenient to solve the governing equations in a rotating frame of reference. In that case, Coriolis and centrifugal forces as well as possibly the Poincaré force have to be included on the right-hand side of the Navier–Stokes equation, so the equation takes the form

$$\frac{D\boldsymbol{u}}{Dt} = \cdots - 2\boldsymbol{\Omega}_0 \times \boldsymbol{u} - \boldsymbol{\Omega}_0 \times (\boldsymbol{\Omega}_0 \times \boldsymbol{r}) - \dot{\boldsymbol{\Omega}}_0 \times \boldsymbol{r}, \tag{50}$$

where r is the position vector with respect to a point on the rotation axis and $\boldsymbol{\Omega}_0 = \text{const}$ is the angular velocity vector of the reference frame. The Poincaré force, $\dot{\boldsymbol{\Omega}}_0 \times r$ can drive flows and even turbulence in precessing bodies with boundaries. This has been discussed in attempts to explain the flows that drive the geodynamo [152–155].

An important effect of the Coriolis force is to suppress variations of the azimuthal velocity in the axial direction. This can be seen by taking the curl of the Coriolis term,

$$\boldsymbol{\nabla} \times (-2\boldsymbol{\Omega}_0 \times \boldsymbol{u}) = 2\Omega_0 \left(\frac{\partial \boldsymbol{u}_\perp}{\partial z} - \hat{\boldsymbol{z}} \boldsymbol{\nabla} \cdot \boldsymbol{u}_\perp \right), \quad (51)$$

where $\boldsymbol{u}_\perp = \boldsymbol{u} - (\boldsymbol{u} \cdot \hat{z})\hat{z}$ is the velocity in the direction perpendicular to the rotation axis and $\hat{z}$ is the unit vector along the direction of $\boldsymbol{\Omega}_0$. Taking the curl of the evolution equation for $\partial \boldsymbol{u}/\partial t$ in cylindrical polar coordinates, (R, ϕ, z), and projecting on the ϕ component, yields

$$\hat{\boldsymbol{\phi}} \cdot \frac{\mathrm{D}\boldsymbol{\omega}}{\mathrm{D}t} = 2\Omega_0 \frac{\partial u_\phi}{\partial z} - \hat{\boldsymbol{\phi}} \cdot (\boldsymbol{\nabla} T \times \boldsymbol{\nabla} s) + F_\phi^{\text{visc}}, \quad (52)$$

where F_ϕ^{visc} is the ϕ component of the viscous force. This shows that, when rotation is important, i.e. Ω_0 is large, $\partial u_\phi/\partial z$ must be small.

Of course, the physics is independent of the coordinate system one is working in. If one is working in the inertial (non-rotating) frame, there is no Coriolis force, but one can then write $u_\phi = R\Omega$, where $\Omega = \Omega(R, \phi, z)$ is now the local angular velocity, which is not to be confused with $\boldsymbol{\Omega}_0$. If the velocity has only an azimuthal component, $\boldsymbol{u} = \hat{\boldsymbol{\phi}} R\Omega$, one can write the curl of the $\boldsymbol{u} \cdot \boldsymbol{\nabla} \boldsymbol{u}$ term as

$$\boldsymbol{\nabla} \times (-\boldsymbol{u} \cdot \boldsymbol{\nabla} \boldsymbol{u}) = R \frac{\partial \Omega^2}{\partial z}. \quad (53)$$

We will return to the astrophysical consequences of this in section 7.3 when we discuss the angular velocity of the Sun.

5.4. Active vectors: magnetic fields and dynamos

An important vector field to be included in the fluid equations is the magnetic field, $\boldsymbol{B}$. It is an active vector because the Lorentz force, $\boldsymbol{J} \times \boldsymbol{B}$, backreacts through the momentum equation, so

$$\rho \frac{\mathrm{D}\boldsymbol{u}}{\mathrm{D}t} = \cdots + \boldsymbol{J} \times \boldsymbol{B}, \quad (54)$$

where $\boldsymbol{J}$ is the current density. One makes here the assumption that there is no net charge in the fluid, i.e. the density of positive and negative charge carriers balances everywhere, and the currents are produced by the sum of the fluxes of counterflowing positive and negative charge carriers. The $\boldsymbol{B}$ field is solenoidal and its evolution is governed by the Faraday equation,

$$\frac{\partial \boldsymbol{B}}{\partial t} = -\boldsymbol{\nabla} \times \boldsymbol{E}, \quad \text{with} \quad \boldsymbol{\nabla} \cdot \boldsymbol{B} = 0, \quad (55)$$

where $\boldsymbol{E}$ is given by Ohm's law,

$$-\boldsymbol{E} = \boldsymbol{u} \times \boldsymbol{B} - \boldsymbol{J}/\sigma, \quad (56)$$

and σ is the electric conductivity. Its inverse is related to the magnetic diffusivity, $\eta = (\mu_0 \sigma)^{-1}$, and it has the same dimension as the kinematic viscosity ν. Their ratio is the magnetic Prandtl number $Pr_M = \nu/\eta$.

Ampere's equation is used to express the current density in terms of the magnetic field via

$$\boldsymbol{J} = \boldsymbol{\nabla} \times \boldsymbol{B}/\mu_0, \quad (57)$$

where μ_0 is the vacuum permeability. Equation (57) is an approximation to the full Faraday equation which includes also the displacement current. Neglecting it corresponds to filtering out electromagnetic waves, which is justified at finite electric conductivity and velocities small compared with the speed of light.

Inserting equation (56) into equation (55) we obtain the induction equation in the form

$$\frac{\partial \boldsymbol{B}}{\partial t} = \boldsymbol{\nabla} \times (\boldsymbol{u} \times \boldsymbol{B} - \boldsymbol{J}/\sigma). \quad (58)$$

In its 'uncurled' form this equation reads

$$\frac{\partial \boldsymbol{A}}{\partial t} = \boldsymbol{u} \times \boldsymbol{B} - \boldsymbol{J}/\sigma - \boldsymbol{\nabla}\phi, \quad (59)$$

where ϕ is the electrostatic potential. By evaluating the time derivative of $\boldsymbol{A} \cdot \boldsymbol{B}$ and integrating over space we obtain the evolution equation for magnetic helicity,

$$\frac{\mathrm{d}}{\mathrm{d}t} \int \boldsymbol{A} \cdot \boldsymbol{B} \, \mathrm{d}V = -2\sigma^{-1} \int \boldsymbol{J} \cdot \boldsymbol{B} \, \mathrm{d}V - \oint \boldsymbol{F}_H \cdot \mathrm{d}\boldsymbol{S}, \quad (60)$$

where $\boldsymbol{F}_H = \boldsymbol{E} \times \boldsymbol{A} + \phi\boldsymbol{B}$ is the flux of magnetic helicity.

Magnetic fields constitute an additional form of energy, $E_M = \int \boldsymbol{B}^2/(2\mu_0) \, \mathrm{d}V$, whose evolution is given by

$$\frac{\mathrm{d}}{\mathrm{d}t} \int \frac{\boldsymbol{B}^2}{2\mu_0} \, \mathrm{d}V = -\int \boldsymbol{u} \cdot (\boldsymbol{J} \times \boldsymbol{B}) \, \mathrm{d}V - \sigma^{-1} \int \boldsymbol{J}^2 \, \mathrm{d}V$$

$$- \oint \boldsymbol{F}_M \cdot \mathrm{d}\boldsymbol{S}, \quad (61)$$

where $\boldsymbol{F}_M = \boldsymbol{E} \times \boldsymbol{B}/\mu_0$ is the Poynting flux. Equation (40) for the evolution of the total energy density can be generalized correspondingly by adding $\boldsymbol{B}^2/2\mu_0$ underneath the time derivative and $\boldsymbol{F}_M$ underneath the divergence term.

In this connection it might be useful to emphasize that in numerical simulations one hardly uses the full energy equation in that form if the magnetic energy becomes comparable to or in excess of the thermal energy. Normally one would calculate the thermal pressure from the internal energy, but in the magnetically dominated case this becomes a small residual between total, kinetic and magnetic energies, and so this calculation becomes exceedingly inaccurate.

Another comment regarding simulations is here in order. A commonly encountered difficulty is to preserve solenoidality of $\boldsymbol{B}$. One method is to use a staggered mesh and to evaluate the right-hand side of equation (55) such that the numerical evaluation of the curl produces zero divergence to machine accuracy. Another method is to use $\boldsymbol{A}$ as dependent variable, which also preserves $\boldsymbol{\nabla} \cdot \boldsymbol{B} = 0$, and it also allows for

a straightforward calculation of the magnetic helicity. Yet another method is to write

$$\boldsymbol{B} = \boldsymbol{\nabla}\alpha \times \boldsymbol{\nabla}\beta, \tag{62}$$

where α and β are the Euler potentials [156]. However, this method only works in the strictly ideal case, in which case the evolution equations are just

$$\mathrm{D}\alpha/\mathrm{D}t = \mathrm{D}\beta/\mathrm{D}t = 0. \tag{63}$$

This approach is now quite popular in smoothed particle hydrodynamics calculations, because then the values of α and β are just kept fixed at each Lagrangian particle [157, 158]. Unfortunately, this method cannot even approximately capture non-ideal effects. As a consequence, dynamo action (see below) is not possible in this approach and energy spectra of MHD turbulence with imposed field become too shallow [159]. Finally, there is the possibility of divergence cleaning, which requires the solution of a Poisson-type equation for the correction term to the numerically obtained $\boldsymbol{B}$ field. This approach is analogous to calculating the pressure under the constraint that $\boldsymbol{\nabla} \cdot \boldsymbol{u} = 0$ or $\boldsymbol{\nabla} \cdot \rho\boldsymbol{u} = 0$; see section 4.3. The disadvantage here is that this approach may introduce an unphysical nonlocality as a consequence of invoking a Poisson-type equation.

The Lorentz force gives rise to various restoring forces that lead to additional wave forms including Alfvén waves as well as fast and slow magnetosonic waves. The slow magnetosonic waves are particularly important in the presence of shear and rotation, because those waves can be destabilized to give rise to the magneto-rotational instability. This will be discussed in more detail in section 6.11.

One of the other new features allowed by the addition of magnetic fields is the possibility of self-excited dynamo action, i.e. the spontaneous conversion of kinetic energy into magnetic energy by work done against the Lorentz force. This is an important process in astrophysics. Magnetic fields observed in planets and stars with outer convection zones are clear examples where dynamo action is required to sustain magnetic fields against ohmic decay and to explain field reversals on time scales short compared with the resistive time. Galaxies and clusters of galaxies also harbor magnetic fields. Many spiral galaxies show magnetic fields with a large-scale design that is approximately axisymmetric. One prominent exception is a galaxy with the name M81, where the field is non-axisymmetric with a strong $m = 1$ component, i.e. the field is proportional to $\mathrm{e}^{\mathrm{i}m\phi}$, where ϕ is the azimuthal angle. Observations give direct indications about the turbulent nature of galactic disks, so the magnetic field must be maintained against turbulent decay in the vertical direction along the axis. The relevant time scale is only about 10^7 yr. In the present review we discuss dynamos only insofar as they are directly connected with understanding or clarifying astrophysical turbulence.

Details regarding dynamo theory as well as magnetic fields in solar-like stars and galaxies have recently been reviewed in [11, 85, 160]. One of the important recent developments concerns the realization that the evolution of the large-scale

magnetic field can be constrained decisively by magnetic helicity evolution; see equation (60). This has to do with the fact that large-scale magnetic fields tend to be helical. This point will be taken up briefly in section 7.2, but for a more thorough discussion we refer to [11] for a recent review.

In the incompressible case with constant density $\rho = \rho_0$, it is convenient to write the MHD equations using Elsasser variables $\boldsymbol{z}_\pm = \boldsymbol{u} \pm \boldsymbol{B}/\sqrt{\mu_0\rho_0}$, because then the evolution equations take a form similar to the usual Navier–Stokes equations, i.e.

$$\frac{\partial \boldsymbol{z}_\pm}{\partial t} + \boldsymbol{z}_\mp \cdot \boldsymbol{\nabla}\boldsymbol{z}_\pm = -\boldsymbol{\nabla}\Pi + \nu\nabla^2\boldsymbol{z}_\pm, \qquad \boldsymbol{\nabla} \cdot \boldsymbol{z}_\pm = 0. \tag{64}$$

Here, $\nu = \eta$ has been assumed for simplicity and $\Pi = (p + \boldsymbol{B}^2/2\mu_0)/\rho$ is a pressure that ensures that $\boldsymbol{\nabla} \cdot \boldsymbol{z}_\pm = 0$.

5.5. Radiation: optically thick and thin

Radiation transport describes the coupling to the photon field. As far as the dynamics is concerned, the radiative flux gives rise to a radiation force that can, for example, cause levitation of the gas by radiation. The radiative energy flux divergence enters the energy equation and describes local heating and cooling. Thus, the momentum and specific entropy equations are amended as follows:

$$\rho\frac{\mathrm{D}\boldsymbol{u}}{\mathrm{D}t} = \cdots + \frac{\rho\kappa}{c}\boldsymbol{F}_{\mathrm{rad}}, \tag{65}$$

$$\rho T\frac{\mathrm{D}s}{\mathrm{D}t} = \cdots - \boldsymbol{\nabla} \cdot \boldsymbol{F}_{\mathrm{rad}}. \tag{66}$$

Here, κ is the opacity, i.e. the photon cross-section per unit mass. The cross-section per unit volume is $\rho\kappa$, which is also the inverse mean free path of photons, $\ell = (\rho\kappa)^{-1}$. If the mean free path is small compared with other relevant length scales, a diffusion approximation may be used for $\boldsymbol{F}_{\mathrm{rad}}$, which means that it is proportional to the negative gradient of the radiation energy density, $\boldsymbol{F}_{\mathrm{rad}} = -\frac{1}{3}\ell c\boldsymbol{\nabla}(aT^4)$, and so it points in the direction of the negative temperature gradient. The transition layer between optically thin and thick is an important region in astrophysics, because it marks the effective surface of an otherwise extended body. In this transition region the diffusion approximation is no longer valid and proper equations for the radiation intensity have to be solved to obtain $\boldsymbol{F}_{\mathrm{rad}}$; see [119, 161].

6. Simulations of turbulence

Astrophysical turbulence is frequently caused by instabilities. However, many instabilities imply the presence of anisotropies. For example, in convection the vertical direction is a preferred one, while in the case of the magneto-rotational instability the velocity gradient matrix associated with the shear governs the anisotropy. In the presence of magnetic fields, the otherwise isotropic turbulence becomes at least locally anisotropic, because at every patch in the turbulent flow the direction of the local mean-field imprints anisotropy on all smaller scales within this patch. On the other hand, much
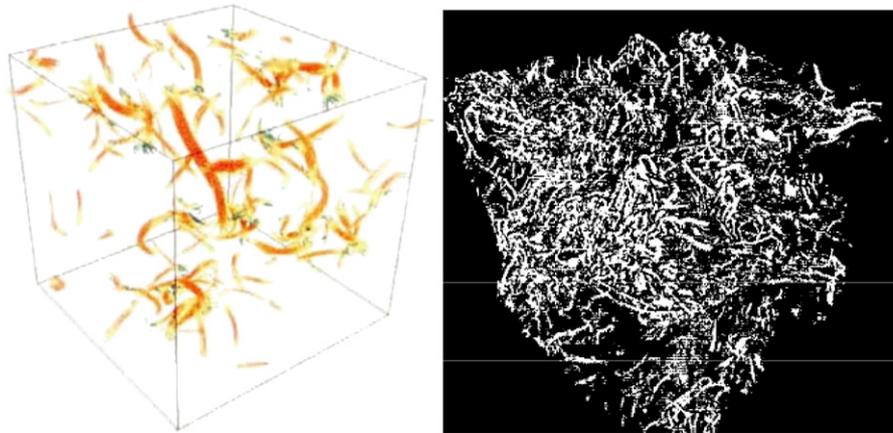
Figure 9. Examples of vortex tubes in homogeneous turbulence. Courtesy of Zhen-Su She (left figure) [177] and Paul Woodward (right figure) [179].

of turbulence theory is concerned with isotropic turbulence. Computationally, isotropic turbulence can be modeled by adopting an imposed forcing function. Common applications of isotropically forced turbulence include simulations of turbulent star formation, as well as turbulent mixing and dynamo processes. We begin by discussing some general aspects of isotropic turbulence simulations.

6.1. General aspects

The concept of isotropic turbulence is a convenient and useful theoretical idealization. Computationally, isotropy does not lead to any significant simplification, except that periodic boundary conditions are possible and in many ways advantageous. Isotropic turbulence needs to be forced by an isotropic body force, unless an isotropic instability can be identified that would drive turbulence. The thermal instability would be an example of an instability without preferred direction, but simulations have not shown that it can lead to sustained turbulence [162, 163]. The Jeans instability is another example, which is particularly relevant to the problem of star formation through strong compressions by the turbulence in the interstellar medium. This problem is frequently tackled using smoothed particle hydrodynamics [164, 165], while mesh-based techniques have explored mostly the case of forced supersonic turbulence [166, 167] and have only recently incorporated the effects of self-gravity, augmented with so-called sink particles to account for the production of high density cores that cannot be resolved with a fixed mesh [168–171].

In order to study more basic properties of turbulence one often resorts to a random forcing function to simulate the effects of an instability with a well-defined forcing strength and a well-defined length scale of the driving. Plane waves with randomly changing orientation are an obvious possibility for driving turbulence. To make the forcing divergence-free, one uses only transversal waves.

The idea of simulating turbulence on the computer developed during the 1970s. Almost all simulations in those days utilized pseudo-spectral methods, i.e. spatial derivatives are calculated in Fourier space by multiplication with i$\mathbf{k}$, but

all nonlinear terms are calculated in real space. The main advantage of such methods is the small discretization error. Furthermore, this technique also allows an efficient solution of the Poisson-like equation for the pressure if one makes the incompressible or the anelastic approximation, i.e. $\nabla \cdot \mathbf{u} = 0$ or $\nabla \cdot \rho\mathbf{u} = 0$, respectively.

Spectral methods have the disadvantage that one cannot easily deal with arbitrary boundary conditions. Also, the Fourier transformation is a nonlocal operation which is not optimal when using many processors. These are reasons why sometimes finite difference methods are used instead. Finite difference methods are normally not as accurate as spectral methods unless one uses a higher-order scheme (e.g. fourth and sixth order schemes are common choices). On the other hand, many astrophysical flows develop shocks for which there are a number of other dedicated methods (Riemann solvers, approximate Riemann solvers, monotonicity schemes, Godunov schemes and Neumann–Richtmyer artificial viscosities [115, 172]). These methods are frequently generalized to mesh refinement methods that allow increased accuracy in specific locations of the flow. Finally, there are also Lagrangian methods of which smooth particle hydrodynamics is an example [165, 173–175]. A promising new Lagrangian method has been presented in [176].

6.2. Hydrodynamic turbulence

When simulations became able to resolve turbulence with around 128^3 meshpoints, it became evident that much of the flow is governed by a tangle of vortices; see, e.g., [177–179]. The left-hand panel of figure 9 shows examples of such vortices. Their thickness is related to the viscous scale while their length was often expected to be comparable with the integral scale. However, in subsequent years simulations at increasingly higher Reynolds numbers seem to reveal that the vortex turbulence becomes a less prominent feature of otherwise nebulous looking structures of variable density (see the right-hand panel of figure 9).

Incompressible forced turbulence simulations have been carried out at resolutions up to 4096^3 meshpoints [18]. Surprising results from this work include a strong bottleneck
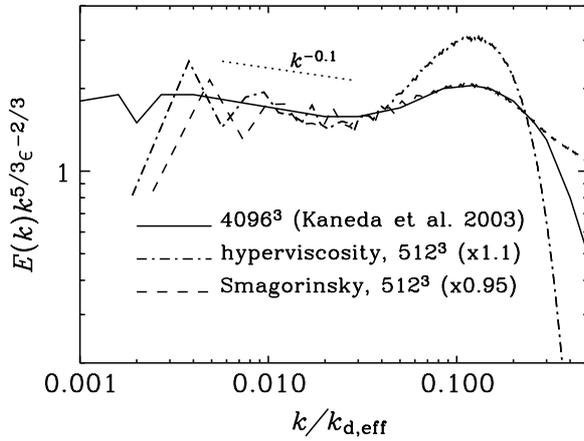
Figure 10. Comparison of energy spectra of the 4096^3 meshpoints run [18] (solid line) and 512^3 meshpoints runs with hyperviscosity (dashed–dotted line) and Smagorinsky viscosity (dashed line). (In the hyperviscous simulation we use $\nu_3 = 5 \times 10^{-13}$.) The Taylor microscale Reynolds number of the Kaneda simulation is 1201, while the hyperviscous simulation of [180] has an approximate Taylor microscale Reynolds number of $340 < Re_\lambda < 730$. For the Smagorinsky simulation the value of Re_λ is slightly smaller. Courtesy of Nils E Haugen [19].

effect [20] near the dissipative subrange, and possibly a strong inertial range correction of about $k^{-0.1}$ to the usual $k^{-5/3}$ inertial range spectrum, so that the spectrum is $k^{-1.77}$. Note that the She–Leveque correction (17) is only $k^{-0.03}$, so that the spectrum is $k^{-1.70}$. Similarly strong inertial range corrections have also been seen in simulations using a Smagorinsky subgrid scale model [19] (512^3 meshpoints, dashed line in figure 10). Here we also show the results of simulations with hyperviscosity, i.e. the $\nu\nabla^2$ diffusion operator has been replaced by a $\nu_3\nabla^6$ operator [180] (512^3 meshpoints, dashed–dotted line). Hyperviscosity greatly exaggerates the bottleneck effect, but it does not seem to affect the inertial range significantly; see figure 10.

The nature of the $k^{-0.1}$ correction factor is currently not understood. It might be an artifact resulting from applying a forcing function at a scale close to the scale of the box [8]. Alternatively, the presence of a bottleneck might also lead to the emergence of a dip just before the bottleneck. In either case this would not be a true $k^{-0.1}$ correction in the entire inertial range.

In virtually all astrophysical settings the relevant Reynolds numbers are very large and the bottleneck is hardly important, because it is located at very small length scales. However, this is not the case in simulations which show the bottleneck as a pronounced feature. There are several important issues here. Firstly, simulations at resolutions of 256^3 meshpoints give hardly any indication of a bottleneck effect, and only at resolutions of 1024^3 meshpoints and above does it really develop its full strength. For this reason the bottleneck effect has been studied more seriously only in recent years. Secondly, the bottleneck effect can affect certain aspects of a simulation in a way that is not yet asymptotically meaningful. An example is the small-scale dynamo effect that is discussed below.

6.3. Supersonic turbulence

In the interstellar medium the gas can condense into more concentrated regions called molecular clouds. These clouds are so cold that molecules can form, which explains their name. Because of low temperature in the range 10–100 K, the flows in these clouds can become highly supersonic. This in turn leads to even stronger mass concentrations that can become gravitationally unstable and form stars. This is why supersonic turbulence is commonly studied in connection with star formation [167, 181].

With increasing Mach number, density fluctuations begin to become important. In fact, in supersonic turbulence with an isothermal equation of state it has been demonstrated that the standard deviation of the (linear) density, σ_{linear}, grows linearly with the Mach number [166, 182, 183]

$$\sigma_{\text{linear}} = \gamma Ma, \qquad (67)$$

where the Mach number is defined as $Ma = u_{\text{rms}}/c_s$. The density obeys a log-normal distribution, i.e. the probability density function, $p(\ln \rho)$, with $\int p(\ln \rho)\,d\ln \rho = 1$, is given by

$$p(\ln \rho) = \frac{1}{\sqrt{2\pi\sigma^2}}\exp\left[-\frac{1}{2}(\ln \rho - \overline{\ln \rho})/\sigma^2\right], \qquad (68)$$

where σ is the standard deviation of the logarithmic density, which is related to the Mach number like [166]

$$\sigma = \ln(1 + \gamma^2 Ma^2), \qquad (69)$$

again with $\gamma \approx 1/2$ to good accuracy.

As indicated in section 2.1 the spectra of $\boldsymbol{u}$, $\rho^{1/2}\boldsymbol{u}$ and $\rho^{1/3}\boldsymbol{u}$ begin to differ from each other at larger Mach number. Observations of the line-of-sight velocity dispersion of molecular clouds in the Perseus cluster also show that in the highly supersonic case the velocity spectrum is not far from $k^{-1.8}$ [184], and thus deviates clearly from the characteristic spectrum of shock turbulence [185]. However, the density weighted spectra tend to become shallower. In particular, the spectra of $\rho^{1/3}\boldsymbol{u}$ are very close to $k^{-5/3}$ [13]; see figure 11. This appears to be connected with the fact that the kinetic energy flux, i.e. the quantity that is constant throughout the inertial range at scale l, is given by $\rho u_l^3/l$. This idea goes back to an early paper by Lighthill [12].

6.4. Hydromagnetic turbulence

The gas in many astrophysical settings is partially or fully ionized and hence electrically conducting. This means that the effects of magnetic fields cannot be neglected. The full extent of associated behavior is not yet well understood, nor is there unambiguous evidence for universal and asymptotic scaling behavior in the limit of large fluid and magnetic Reynolds numbers [186]. However, using decay simulations at moderate magnetic Reynolds numbers, three types of behavior have been identified [187], depending essentially on the ratio of the initial magnetic to kinetic energy densities. The purpose of this section is to discuss the expected properties in these three regimes.
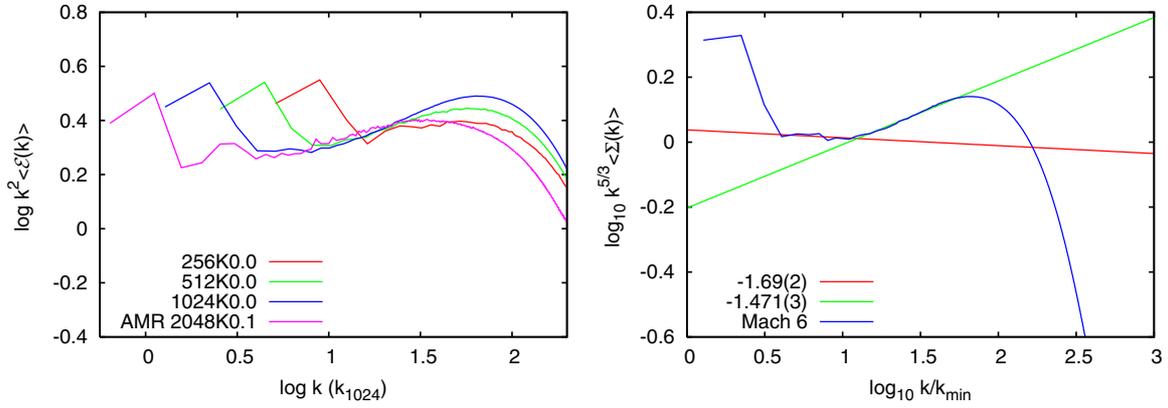
Figure 11. Left: time-averaged velocity spectra compensated by k^2 from uniform grid PPM simulations at resolutions 256^3, 512^3, 1024^3, and from an adaptive mesh refinement simulation with effective resolution of 2048^3 grid points. The spectra demonstrate convergence for the inertial range of scales. Right: time-averaged spectrum of $\rho^{1/3}\boldsymbol{u}$ compensated by $k^{5/3}$. The straight lines represent the least-squares fits to the data within a suitable intermediate range of wavenumbers. Courtesy of Alexei Kritsuk [13].

It is convenient to introduce here the Alfvén speed $v_A = B_{rms}/\sqrt{\mu_0 \rho_0}$ associated with the random magnetic field B_{rms}. The case of sub-equipartition random fields with $v_A < u_{rms}$ was studied by Iroshnikov [188] and Kraichnan [189] who argued that the turbulence can still be treated as isotropic and that the flux of energy ϵ down the turbulent cascade will be modified by Alfvénic interactions and replaced by the geometric mean of energy flux and Alfvén speed, i.e.

$$\epsilon \to (\epsilon v_A)^{1/2}. \tag{70}$$

The dimensional argument used in equation (8) for the energy spectrum of Kolmogorov turbulence gets correspondingly modified and is then of the form

$$E(k) = C_{IK}(\epsilon v_A)^{1/2} k^{-3/2}. \tag{71}$$

In the case of strong magnetic fields, $v_A \gg u_{rms}$, the turbulence becomes highly anisotropic, so the spectrum $E(k_\perp, k_\parallel)$ depends on the wavenumbers parallel ($k_\parallel$) and perpendicular ($k_\perp$) to the local direction of the field. In this limit the turbulence can be treated as wave turbulence using weak turbulence theory [190], which leads to

$$E(k_\perp, k_\parallel) \sim k_\perp^{-2}. \tag{72}$$

In the intermediate case, the kinetic energy of the turbulence is comparable to that of the magnetic field. This regime is referred to as *strong* turbulence—not because the field is strong, but because the $\boldsymbol{u} \cdot \boldsymbol{\nabla} \boldsymbol{u}$ nonlinearity cannot be neglected. The flow is still anisotropic, and energy is cascaded in $k_\perp$ at a rate ϵ. The resulting energy spectrum is [191–194], i.e.

$$E(k_\perp, k_\parallel) = C_{GS} \epsilon^{2/3} k_\perp^{-5/3}. \tag{73}$$

In the following we present a more detailed phenomenology that highlights the essential physics behind the various regimes.

We consider as governing equations the MHD equations written for the Elsasser variables $\boldsymbol{z}_\pm$, see equation (64), and denote by $z_{k_\perp}$ the modulus of $\boldsymbol{z}_\pm$ at wavenumber $k_\perp$. In all cases the energy spectrum is given by

$$E(k_\perp, k_\parallel) \sim z_{k_\perp}^2 / k_\perp, \tag{74}$$

and the spectral energy flux is then given by an expression of the form

$$\epsilon = z_{k_\perp}^2 / \tau_{casc}, \tag{75}$$

where τ_{casc} is the cascade time. The main difference between the various regimes lies in the form of the τ_{casc}; see also [11, 195].

For strong magnetic fields, interactions are being accomplished by wave packets traveling in opposite directions. The duration of the interactions is given by

$$\tau_A = (v_A k_\parallel)^{-1}, \tag{76}$$

where $k_\parallel^{-1}$ is the longitudinal extent of such a packet. The fractional change in a wave packet is given by the ratio

$$\chi = \tau_A / \tau_{NL} \tag{77}$$

of Alfvén time to the nonlinear interaction time

$$\tau_{NL} = (z_{k_\perp} k_\perp)^{-1}. \tag{78}$$

However, because the sign of each interaction is random, the net effect grows only like the square root of the number of interactions. Therefore, the effective fractional change associated with each interaction is only χ^2. This means that the effective cascade time is $\tau_{casc} = \tau_A/\chi^2$. By contrast, in the strong turbulence regime the Alfvén and nonlinear times are equal, i.e. $\chi = 1$, and the cascade time is therefore just $\tau_{casc} = \tau_{NL}$. Since the $z_{k_\perp}$ in equation (74) enters also in the expression for τ_{casc}, the resulting spectra are qualitatively different. For weak turbulence we have

$$\epsilon = \frac{z_{k_\perp}^2}{\tau_{casc}} = z_{k_\perp}^2 \frac{(z_{k_\perp} k_\perp)^2}{v_A k_\parallel},$$

$$\text{so} \quad E(k_\perp, k_\parallel) \sim \frac{z_{k_\perp}^2}{k_\perp} \sim (\epsilon v_A k_\parallel)^{1/2} k_\perp^{-2}, \tag{79}$$

while for strong turbulence we have

$$\epsilon = \frac{z_{k_\perp}^2}{\tau_{casc}} = z_{k_\perp}^2 (z_{k_\perp} k_\perp),$$

$$\text{so} \quad E(k_\perp, k_\parallel) \sim \frac{z_{k_\perp}^2}{k_\perp} \sim \epsilon^{2/3} k_\perp^{-5/3}. \tag{80}$$

19

Table 1. Summary of the essential properties of the three regimes of MHD turbulence.

|	Iroshnikov–Kraichnan (isotropic, sub-equip.)	Strong turbulence (critically balanced)	Weak turbulence (wave turbulence)
$v_A/u_{rms} \sim \chi^{-1}$	<1	~ 1	>1
τ_{casc}	$\chi^{-2}\tau_A$ (with $k_\perp = k_\parallel$)	$\chi^{-1}\tau_A (= \tau_{NL})$	$\chi^{-2}\tau_A$
ϵ	$z_k^4 k/v_A$	$z_{k_\perp}^3 k_\perp$	$z_{k_\perp}^4 k_\perp^2/v_A k_\parallel$
$k_\perp/k_\parallel$	1	$\propto k_\perp^{1/3}$	$\to \infty$
$E(k_\perp, k_\parallel)$	$(\epsilon v_A)^{1/2} k^{-3/2}$	$\epsilon^{2/3} k_\perp^{-5/3}$	$(\epsilon v_A k_\parallel)^{1/2} k_\perp^{-2}$
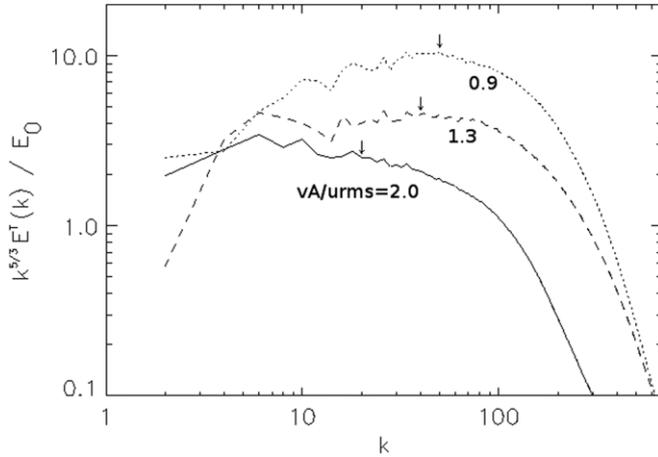
Figure 12. Total energy spectra compensated by $k^{5/3}$ and averaged over $\Delta t = 0.5$ (1.5 to 2 turnover times) about the maximum of dissipation for three runs: solid line for super-equipartition initial fields ($v_A/u_{rms} \approx 2.0$), dashed for equipartition initial fields ($v_A/u_{rms} \approx 1.3$) and dots for sub-equipartition initial fields ($v_A/u_{rms} \approx 0.9$). The three arrows indicate the magnetic Taylor scale. Note that the three spectra follow noticeably different spectral laws and possibly different scale-dependence for their time scales as well. In all cases the numerical resolution is 2048^3. Courtesy of E Lee *et al* [187].

In the latter case, because of $\tau_{NL} = \tau_A$, we have $k_\perp/k_\parallel = v_A/z_{k_\perp} = (v_A/\epsilon)k_\perp^{1/3}$, so the degree of anisotropy increases toward smaller scales until we have $k_\parallel \to \infty$. For weak turbulence we have $k_\parallel \to 0$, so the turbulence is fully anisotropic at all scales. Finally, for even weaker magnetic fields, the weak turbulence formalism again applies, except that now the turbulence is isotropic, i.e. we put $k_\perp = k_\parallel = k$ and thus recover equation (71). Table 1 summarizes the essential properties in the three regimes.

Using up to 2048^3 simulations of decaying MHD turbulence with different initial field strength, Lee *et al* [187] showed that all three scalings are indeed possible. In figure 12 we show compensated power spectra for three runs with different initial field strengths with $v_A/u_{rms} \approx 0.9$, 1.3 and 2.0, that are consistent with the regimes of Iroshnikov–Kraichnan turbulence, strong turbulence and weak turbulence, respectively.

6.5. Dynamo action

In the absence of an externally imposed magnetic field, it is possible that the field-free state is unstable to the dynamo instability, which leads to a conversion of kinetic to magnetic
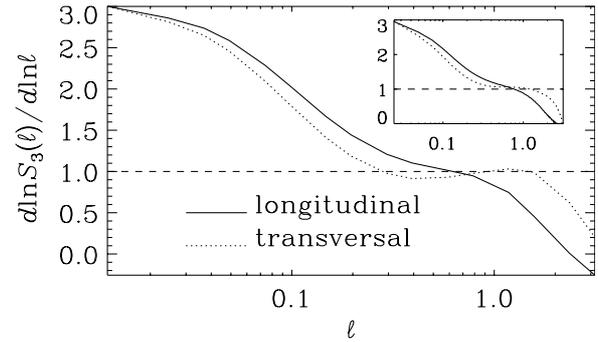

Figure 13. Third order structure function, as defined in equation (16), for hydromagnetic runs with 512^3 meshpoints [196]. The inset gives the result for 256^3 meshpoints. The scaling for transversal structure functions (dotted lines) tends to be better than for the longitudinal ones (solid lines). The statistics for the 256^3 runs is somewhat better than for the shorter 512^3 runs. Courtesy of Nils E Haugen [196].

energy. If dynamo action occurs, the magnetic field will grow exponentially to become dynamically important. The precise outcome regarding energy spectra and structure functions is still uncertain, but there is mounting evidence that in the inertial range they are similar to those in the purely hydrodynamic case [104, 196, 197]; see figures 13 and 14. However, the largest resolutions obtained in MHD simulations so far are still only between 1536^3 [198] and 2048^3 mesh points [187], and it is not necessarily surprising that there is no evidence for a clear bottleneck effect, although the spectra have always been seen to be slightly shallower than $k^{-5/3}$ and closer to $k^{-3/2}$ [196, 199–202]. However, it has been argued that, compared with fluid turbulence, MHD turbulence is more nonlocal in spectral space [186]. The anticipated spectral bump would be more spread out, which might explain the absence of a bottleneck at the resolutions available so far, and that much larger resolution would be needed to see it. For supersonic MHD turbulence with dynamo action there is evidence that the mixed longitudinal structure functions of Politano and Pouquet [28] in equation (18) scale linearly with r, provided the Elsasser variables are scaled with a $\rho^{1/3}$ factor [203, 204].

In the absence of helicity and with full isotropy, a successful dynamo (positive growth rate in the linear regime or finite amplitude in the nonlinear regime) is referred to as small-scale dynamo. This refers to the nature of the dynamo process rather than just the typical scale of the magnetic field. For example, a small-scale magnetic field that is just the result of shredding of an imposed large-scale field is not the result of any dynamo process. On the other hand, in the presence of
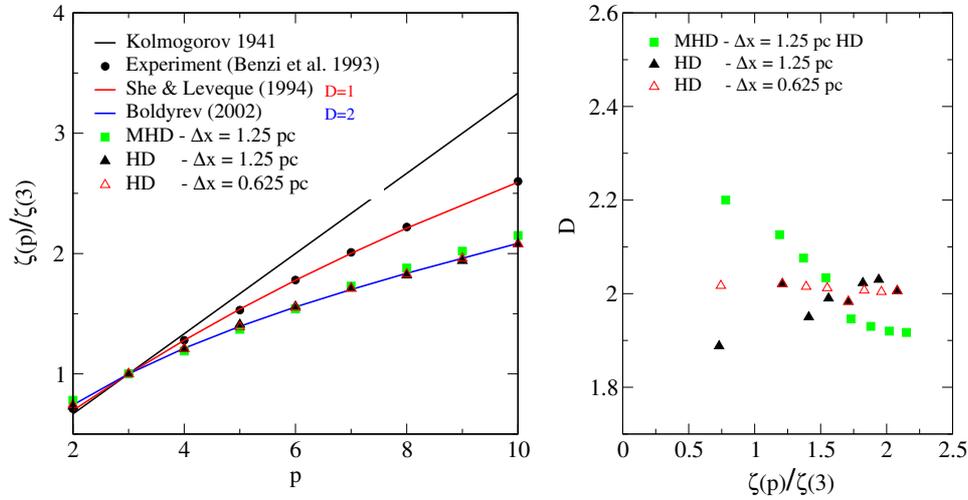
Figure 14. Structure function exponents for interstellar turbulence simulations (left) and fractal dimension of the dissipative structures (right) from simulations. Courtesy of Miguel de Avillez [197].
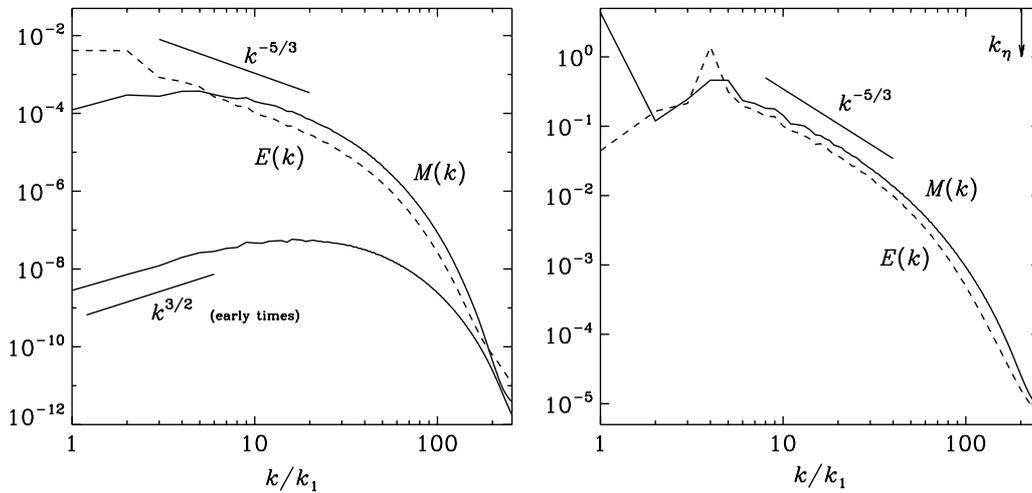
Figure 15. Kinetic and magnetic energy spectra in a turbulence simulation without net helicity (left) and with net helicity (right) for a magnetic Prandtl number of unity and a mesh size of 512^3 meshpoints. Note the pronounced peak of $M(k)$ at $k = k_1$ in the case with helicity. Adapted from [11] and [205], respectively.

helicity, or with anisotropy combined with a mean shear flow, there is the possibility of large-scale dynamo action.

6.6. Large-scale and small-scale dynamos

A typical large-scale dynamo produces magnetic energy on a scale larger than the scale of the energy-carrying eddies. A small-scale dynamo is one that generates magnetic energy on scales smaller than the scale of the energy-carrying eddies. The difference between large-scale and small-scale dynamos is demonstrated in figure 15 where we compare kinetic and magnetic energy spectra of turbulent dynamos with [205] and without [11] helicity. Flows with a large-scale helical pattern of alternating sign, such as the Taylor–Green flow [206, 207], may be considered as an intermediate case between large-scale and small-scale dynamos.

In the following we use the magnetic Reynolds number, defined analogously to the fluid Reynolds number in

equation (11) by replacing ν by η:

$$Re_M = u_{\rm rms}/\eta k_{\rm f}. \qquad (81)$$

The ratio between kinematic viscosity and magnetic diffusivity is referred to as the magnetic Prandtl number, $Pr_M = \nu/\eta$. The onset of a dynamo is characterized by $Re_M \geqslant Re_{M,\rm crit}$, where $Re_{M,\rm crit}$ is the critical value. An important difference between large-scale and small-scale dynamos is the different dependence of $Re_{M,\rm crit}$ on Pr_M. Establishing an asymptotic dependence of $Re_{M,\rm crit}$ on Pr_M is important because, even though the computing power will increase, it will still not be possible to simulate realistic values of Pr_M in the foreseeable future. Schekochihin *et al* [208] have compared the results from two independent codes and show that there is a sharp increase in $Re_{M,\rm crit}$ with decreasing Pr_M; see figure 16 (where the two quantities are denoted as Rm$_c$ and Pm). Such a result was first derived analytically [209], well before it was seen also in simulations.
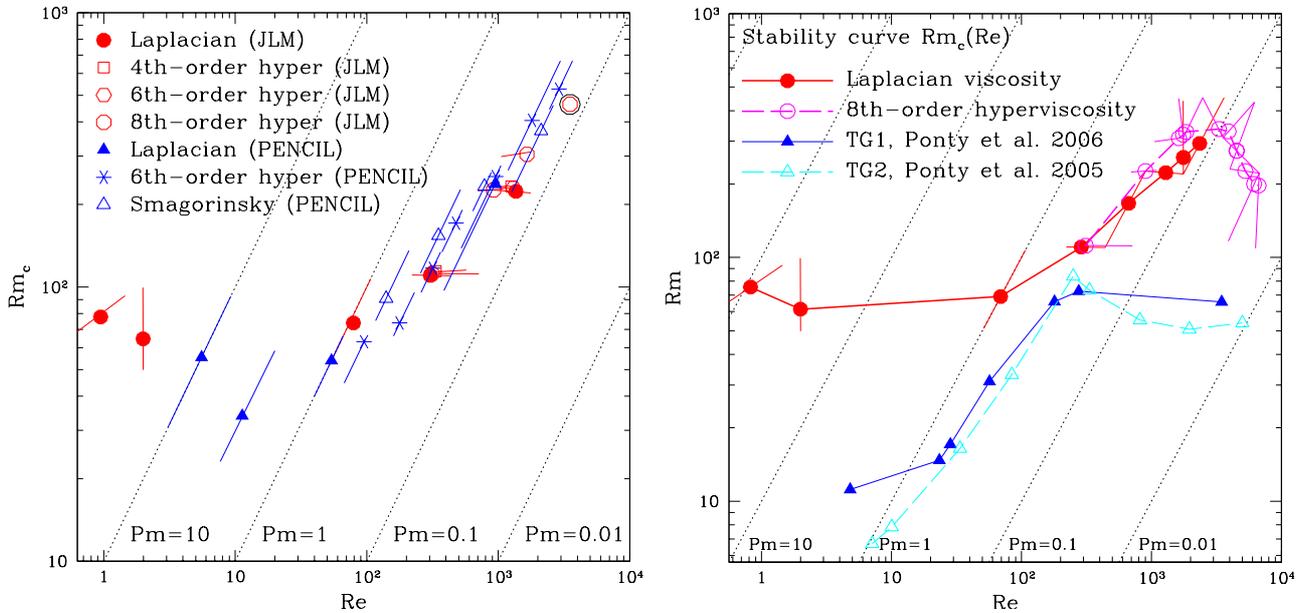
Figure 16. Dependence of R_{crit} on Re. The plot on the left-hand side compares the results from spectral simulations with those of meshpoint methods. The plot on the right-hand side shows the results of the most recent simulations with magnetic Prandtl numbers down to 0.06 and compares with the case of the Taylor–Green flow [206, 207]. 'JLM' refers to simulations done with the incompressible spectral code written by J L Maron: runs with Laplacian viscosity, 4th-, 6th- and 8th-order hyperviscosity (resolutions 64^3 to 256^3). In this set of simulations, hyperviscous runs were done at the same values of η as the Laplacian runs, so the difference between the results for these runs is nearly imperceptible. 'PENCIL' refers to weakly compressible simulations done with the PENCIL code: runs with Laplacian viscosity, 6th-order hyperviscosity, and Smagorinsky large-eddy viscosity (resolutions 64^3 to 512^3). Courtesy of A A Schekochihin [208].

The reason for the increase in $Re_{M,\text{crit}}$ with increasing Re has been explained by Boldyrev and Cattaneo [210] as being related to the fact that when $Re_M < Re$, the resistive scale (i.e. where the magnetic power spectrum peaks in the kinematic regime) shifts from the dissipative subrange into the inertial range. In the inertial range the velocity field is no longer smooth, but it is rough in the sense that the exponent ζ_1 (see section 2.4) in the scaling of velocity differences over distance r is less than 1 [210]. For $\zeta_1 < 1$, the velocity field becomes non-differentiable in the sense that velocity gradients diverge like $r^{\zeta_1 - 1}$. The smaller ζ_1, the rougher the velocity field, while $\zeta_1 = 1$ corresponds to a smooth velocity field.

More recent work [211, 212] suggests that the threshold for small-scale dynamos is particularly high *only* in the range $0.06 \lesssim Pr_M \lesssim 0.2$, because then the resistive scale lies within the range where the kinetic energy spectrum shows the bottleneck with $\zeta_1 \to 0$, corresponding to an extremely rough velocity field with very large critical magnetic Reynolds number. However, when $Pr_M \lesssim 0.06$, the resistive scale lies beyond the bump of the bottleneck, i.e. well inside the inertial range, and there the critical magnetic Reynolds number is again somewhat smaller. Resolving this issue conclusively requires a numerical resolution well in excess of 1024^3 meshpoints, as well as long run times, which is only now beginning to become feasible. We may therefore expect further developments in this area in the near future.

If there is large-scale dynamo action, the magnetic field grows preferentially at scales large compared with the energy-carrying scale. This process is non-local in spectral space [213], although it has also been shown that an externally applied magnetic field produces mainly local interactions

[214]. On the other hand, large-scale dynamo action depends on velocity and magnetic field correlations at the energy-carrying scale (rather than the resistive scale). The onset of this type of large-scale dynamo action is essentially independent of Pr_M and occurs when $Re_M > Re_{M,\text{crit}} \approx 1$. The independence of the saturation strength of the large-scale dynamo on the microscopic resistivity is demonstrated in figure 17, where we show spectra of kinetic and magnetic energies for different values of Pr_M.

6.7. Turbulent convection and stratification

In certain layers of a star the opacity of the gas can become so large that the energy flux can no longer be transported by radiative diffusion, but by convection. A phenomenological theory called mixing-length theory allows one to make reasonable estimates for the expected turbulent velocity. As mentioned in section 3.2, the convective energy flux is approximately equal to the ρu_{rms}^3. This gives a good estimate for the convective velocity in a star.

The basics of the convection instability was discussed in section 5.2. A necessary condition for convection is that the specific entropy decreases with height, i.e. $N_{\text{BV}}^2 < 0$; see equation (47). In addition, viscosity and thermal diffusion have to be small enough compared with the height of the unstable layer, d, and the Brunt–Väisälä frequency, N_{BV}. This is quantified by the Rayleigh number,

$$Ra = \frac{d^4}{\nu \chi}(-N_{\text{BV}}^2)_0, \tag{82}$$

which has to be above a certain critical value for the onset of convection. Here, the subscript 0 refers to the requirement
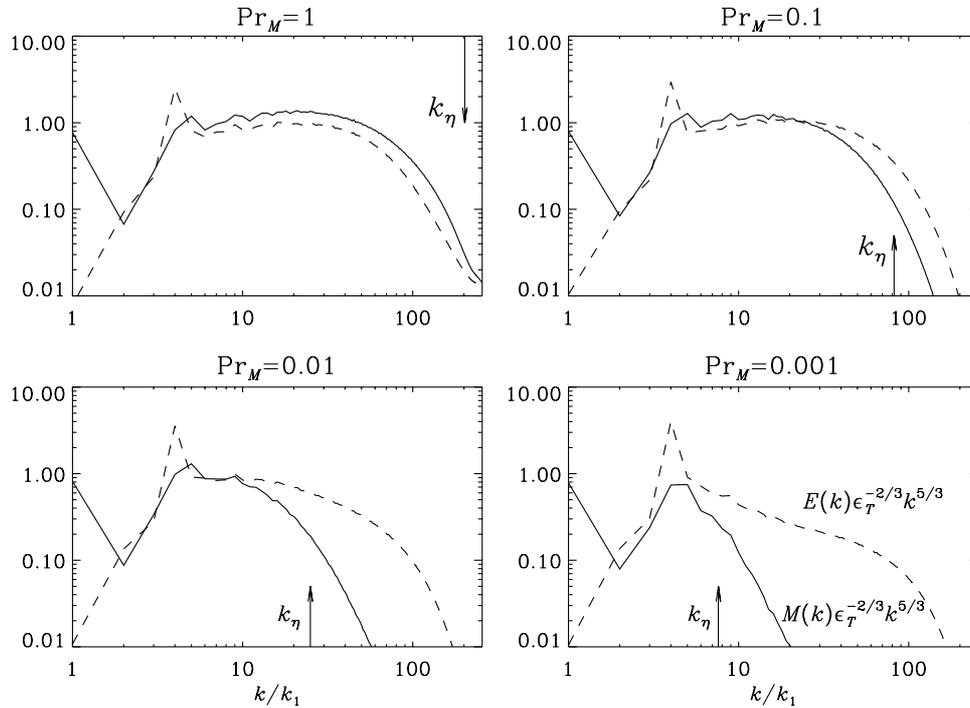
Figure 17. Compensated kinetic and magnetic energy spectra in the saturated regime for $Pr_M = 1$ with $Re = 450$, $Pr_M = 10^{-1}$ with $Re = 1200$, $Pr_M = 10^{-2}$ with $Re = 2300$ and $Pr_M = 10^{-3}$ with $Re = 4400$. The spectra are compensated by $\epsilon_T^{-2/3} k^{5/3}$, where ϵ_T is the sum of kinetic and magnetic energy dissipation rates. The ohmic dissipation wavenumber, $k_\eta = (\epsilon_M/\eta^3)^{1/4}$, is indicated by an arrow. The viscous dissipation wavenumbers are 180, 290, 350 and 430 for $Pr_M = 1$, 10^{-1}, 10^{-2} and 10^{-3}, respectively. Adapted from [205].

that the specific entropy gradient has to be calculated for the associated hydrostatic equilibrium solution, and not for the already convectively unstable solution. Such solutions are not normally presented in the literature. Also, the thickness of the outer layers of the Sun would be much smaller in the hydrostatic reference state. It is therefore not common to quote Rayleigh numbers in astrophysics, except in idealized simulations whose hydrostatic reference solutions tend to be polytropes where the initial density is related to the initial temperature via $\rho \sim T^n$, where n is the polytropic index. Unlike the incompressible case, where the Rayleigh number is based on the background gradient of temperature, in the compressible case it is based on the gradient of specific entropy for the associated hydrostatic solution [52].

If the value of the Rayleigh number is increased sufficiently beyond the critical value, the flow becomes turbulent. Simulations of turbulent convection have been provided by many different groups, both in the incompressible approximation [215–217] as well as in the fully compressible case [148, 218, 219]. Typical Rayleigh numbers that are currently reached in simulations are around 10^6. With rotation the onset of convection is delayed correspondingly, which enables one to reach somewhat larger Rayleigh numbers in such cases.

The Nusselt number is another commonly used quantity in incompressible and laboratory convection. In that case it gives the ratio of the total heat flux to that transported by heat conduction alone, using the same boundary conditions. However, unlike laboratory convection, where the temperatures at top and bottom are usually kept fixed, in

many compressible simulations with a polytropic background solution the energy flux at the bottom is actually prescribed. One compares therefore normally with the radiative solution with a linear temperature profile that has the same top and bottom temperatures as the convective solution. One also subtracts out the flux that is transported by the adiabatic stratification alone [151]. Again, this value is nowadays not normally quoted for compressible simulation. For many purposes, a more useful characterization of the turbulence is the resulting value of the Reynolds number.

Another important difference to laboratory convection is the absence of boundaries in astrophysical convection. Convectively unstable layers are the result of a particular dependence of opacity on temperature and density. This has frequently been modeled using prescribed spatial profiles of the radiative conductivity. In this way one can model convection in an unstable layer, sandwiched between two stable layers [220]. This makes the dynamics near the transition layer softer and allows the flow to overshoot into the stably stratified layers. This leads to the excitation of gravity waves in the stably stratified layers [220–225].

Convective flows can well support dynamo action. As an example we mention here the result of a convection simulation with horizontal shear which leads gradually to the development of a large-scale magnetic field [226]. A result of such calculations is shown in figure 18, where we visualize the toroidal field component at an early time when only small-scale fields have been produced, and at a later time when also a large-scale field is present.

The presence of large-scale fields is often characterized by energy spectra. However, because of stratification it only
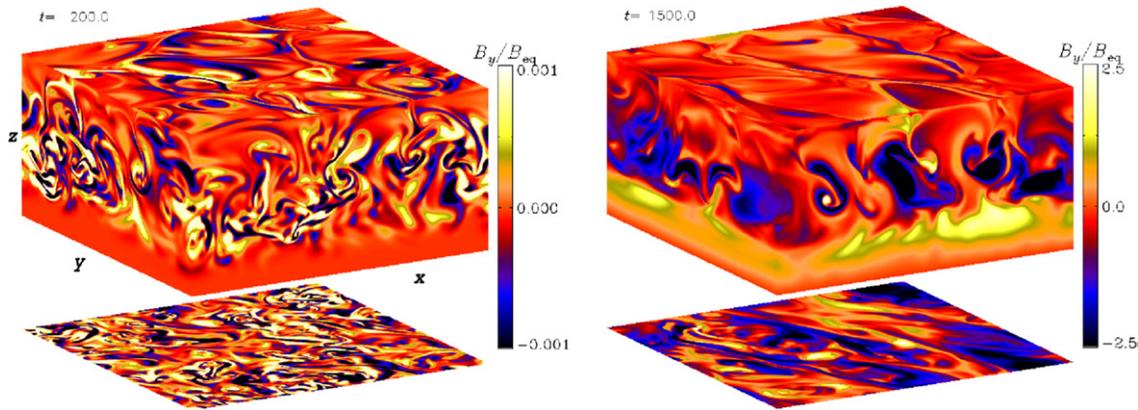
Figure 18. Snapshots of B_y in the early phase (left) and saturated phase (right) of the dynamo. The sides of the box show the periphery of the domain whereas the top and bottom slices show B_y at top and bottom of the convectively unstable layer, respectively. Courtesy of Petri J Käpylä [226].

makes sense to look at horizontal spectra taken at a specific depth. If the mean magnetic field depends mainly on depth, the horizontal magnetic energy spectra will peak at wavenumber zero, which can only be seen if one plots the spectral energy versus linear wavenumber; see, for example, figure 12 of [226].

6.8. Global hydromagnetic dynamo simulations

Simulations of global convection have demonstrated the generation of differential rotation and magnetic fields [227, 228]. However, with parameters relevant to the Sun such models have not yet produced large-scale magnetic fields similar to those in the Sun [55, 121]. This is plausibly explained by the relevant dynamo numbers for coherent large-scale field generation being still too small. In that case, only small-scale magnetic fields are generated, while the threshold for large-scale field generation has still not been reached. This is different when the rotation rate of the sphere is increased to several times the solar value [229]. As an example we show here the results for a sphere that has a stratification similar to that of the Sun, but it is rotating about 3 times as fast; see figure 19.

The rapid rotation is primarily responsible for producing the typical convection patterns that are elongated in the direction of the rotation axis. This effect is especially obvious at low latitudes, outside the inner tangent cylinder, i.e. the cylinder that is tangent with the bottom of the convection zone. The resulting convection pattern is often referred to as banana cells, a concept that was widely discussed in the 1980s [230], but there has never been observational evidence supporting this type of flow pattern for the Sun. Banana cells occur as a consequence of rapid rotation, which is also responsible for cylindrical angular velocity contours. Although this does not apply to the Sun, it may well apply to some stars that rotate much more rapidly than the Sun.

Simulations of rapidly rotating convection [56, 229] show that in the region with strong banana cell convection, there is strong large-scale dynamo action with pronounced toroidal flux belts on one or both hemispheres; see figure 19. This is partially reminiscent of the magnetic activity in the Sun, although it would be premature to draw any conclusions from

this given that at present there is no explicit evidence of banana cell convection in the Sun.

We mention here another line of research. Instead of convection driving the flow one can apply an artificial forcing function. This has the advantage of producing a flow pattern whose typical scale can be controlled. In particular, it is possible to achieve turbulent scales that are small compared with the radial extent of the domain, so as to produce a well-defined scale separation [231, 232]. With such simulations it has been possible to focus entirely on the nature of the dynamo in spherical shell geometries and to isolate its physics from many other effects that may still be important. It turns out that even in the absence of global shear, oscillatory large-scale fields can be generated [232, 233]. Such solutions show equatorward migration and are quite different in nature from oscillatory solutions of $\alpha\Omega$ type. It is quite possible that these solutions have nothing to do with those in the solar dynamo, but it serves as a reminder that the variety of possibilities may be much larger than what is usually discussed.

6.9. Interaction between convection and shear

Simulations of rotating convection in spherical shells demonstrate that there is equatorward acceleration of the mean flow. This phenomenon is generally referred to as differential rotation and will be discussed in more detail in section 7.3. In addition, one sees that the convection pattern itself moves differentially across the surface. However, a more detailed inspection reveals that at the equator the convection pattern can actually move still somewhat faster than the mean flow. This has been revealed both by linear theory [234–236] and by nonlinear simulations [237], and may explain a phenomenon seen at the solar surface which shows that magnetic tracers move at speeds faster than the speed of the plasma. In fact, even very young sunspots tend to move not only faster than the plasma at the surface, but they move also faster than the gas at any other place in the Sun, as seen by global helioseismology; see figure 4 of [238].

There is at present no universally accepted theory for the enhanced rotation speed of magnetic tracers on the Sun. It has, however, been pointed out that the enhanced
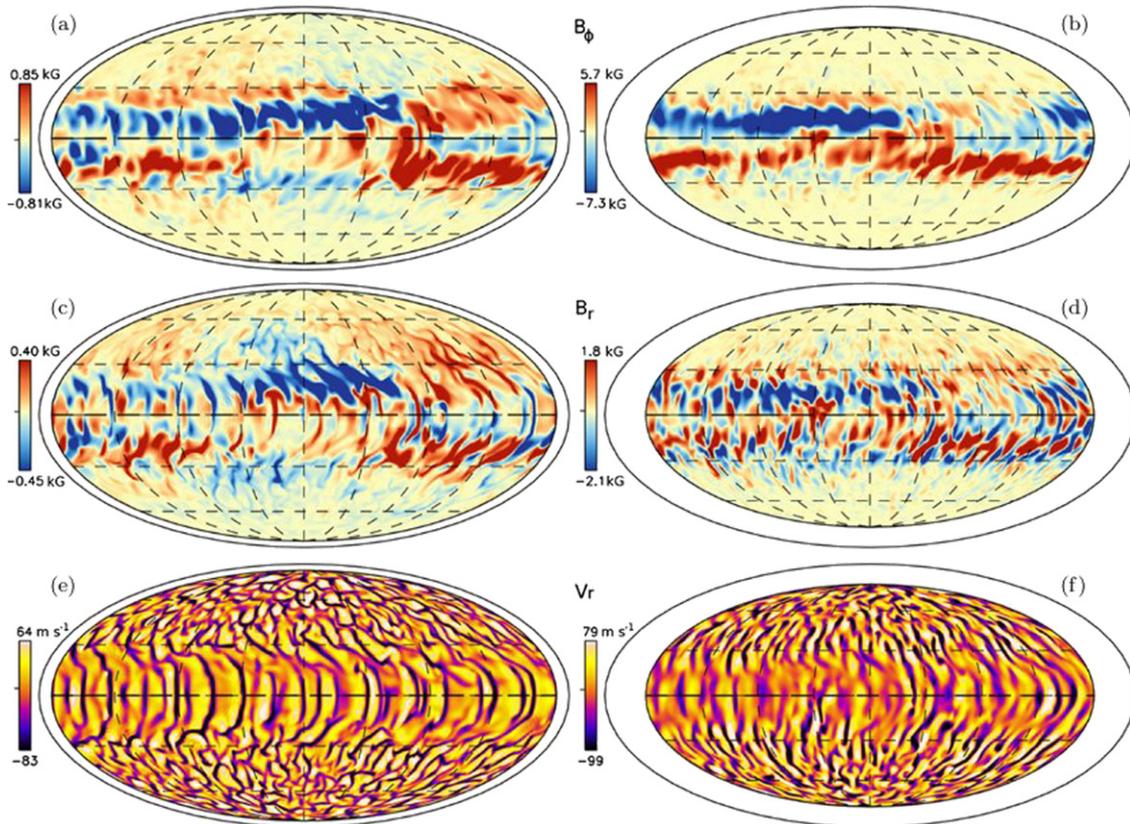
Figure 19. Toroidal and radial magnetic field (first and second row) together with radial velocity (bottom row) near the top of the convective shell (left column at $r/R = 0.95$) and in the middle (right column at $r/R = 0.85$). The mean magnetic field is approximately antisymmetric about the equator. The radial velocity shows flow patterns elongated along the rotation axis (so-called banana cells). The resolution is $96 \times 256 \times 512$ mesh points or collocation points in the radial, latitudinal and longitudinal directions, respectively. The magnetic Reynolds number based on the thickness of the convective shell and without dividing by 2π is 86 and the Coriolis number, i.e. the ratio of vorticity from the mean rotation to the rms vorticity of the turbulence, is about 3. Courtesy of Benjamin P Brown [229].

pattern speed of magnetic tracers might be understandable if the observed magnetic field (including that responsible for producing sunspots) was generated in a layer not too far below the surface [239]. This proposal would be in conflict with the generally adopted view according to which the magnetic field responsible for the solar cycle is generated near or even below the bottom of the convection zone of the Sun.

6.10. Granulation, convection and solar abundances

Simulations of solar granulation have reached a high level of realism and have proved to be a viable and feasible alternative to earlier one-dimensional models for calculating diagnostic spectra in visible light. Strictly one-dimensional models always needed to incorporate ill-determined parametrizations of what is known as micro- and macro-turbulence. New realistic three-dimensional simulations of solar convection [49–51, 240–243] lead to diagnostic spectra that can be fitted to observed spectra without invoking these ill-known parametrizations. The use of 3D models also results in abundances derived from different spectral features (e.g. molecular and atomic lines) being more consistent.

Initial efforts to derive updated solar abundances based on 3D models resulted in new abundance estimates for the heavier elements in the Sun that were as low as only 60% of previous

estimates [244]. It should be noted, however, that even though these abundances are often referred to as '3D abundances', 3D effects were *not* the main cause of the systematic lowering of the abundance estimates, which were instead a combined result of updated oscillator strengths, different line fitting procedures, and choices made when estimating collision cross sections important for non-LTE corrections for some spectral lines. This was elucidated by an independent analysis by a different group [50, 243], who confirmed that 3D effects improve the consistency but do not give rise to a significant systematic abundance effect for the important heavy elements.

The abundances of the heavier elements determine the opacity of the gas and thereby the detailed radial structure of the Sun. On the other hand, the radial dependence of the sound speed and density in the Sun can be determined independently through helioseismology [59, 60, 63, 245, 246], and helioseismology can thus provide important constraints on the heavy element abundances in the solar interior. (It may in the future be possible to also determine the Sun's deep interior composition by exploiting neutrinos from the CN cycle and the p–p chain to determine the primordial solar core abundances of C and N at an interesting level of precision [247].) In the convection zone the gradual ionization of carbon, nitrogen and oxygen with depth influences the equation of state, and helioseismic measurements of the effective ratio of specific

heats of the gas can thus provide constraints on the abundance of these elements also there [62, 248].

The significant downward revision of solar abundances proposed in [242] and even the somewhat more moderate revisions proposed more recently by the same group [51] turned out to be difficult to reconcile with observational constraints from helioseismology, despite many different attempts to do so; cf [62] and references therein. However, the downward revisions recommended by [50] are only about half as large and are in fact consistent with helioseismic estimates of the heavy element abundance in the solar convection zone, $Z = 0.167$; see table 2 of [248].

Due to gravitational settling the abundances of all elements differ somewhat between the convection zone and the radiative interior [249]. Because of rapid mixing the abundance levels are constant in the convection zone, but below the convection zone the chemical abundances vary with radius in a manner that is influenced by how turbulence in the convection zone generates weak overshooting motions in the radiative zone, which result in a slow mixing over depth of chemical elements [250].

There was always a small departure in sound speed between models and helioseismic observations in a narrow region just below the convection zone. With the revised abundance estimates by [242] this departure increased from about 0.3% to about 1.2% [62, 251], while with the abundances recommended by [50] the discrepancy is of the order 0.6%. Even the smallest of these discrepancies is many times larger than the helioseismic measurement uncertainties, and one should thus worry less about the particular size of the discrepancy in any one case, and more about the very existence of the discrepancy. In general terms, the lack of a detailed quantitative understanding of the overshoot of convection below the bottom of the convection zone and the associated slow mixing seems to be a likely reason for the discrepancy [61].

An important additional observational constraint on slow mixing below the convection zone comes from the depletion of lithium in the Sun. Lithium is destroyed at temperatures that are reached about one pressure scale height (corresponding to about 1% of the solar mass) below the convection zone, and the observed depletion (a factor of about 160) implies that mixing down to that temperature takes place on a time scale considerably shorter than the age of the Sun, but still very large compared with convection zone turnover times [61, 252]. Lithium depletion in other stars is now known to be essentially consistent with the behavior expected from the differences in age and structure deduced from standard stellar evolution theory [252].

### 6.11. Turbulence from the magneto-rotational instability

In the presence of shear and rotation, the slow magnetosonic waves develop a long wavelength instability, where $\omega^2 < 0$ for $v_A^2 k^2 < 2q\Omega^2$. Here, $q = -\mathrm{d}\ln\Omega/\mathrm{d}\ln r$ quantifies the radial gradient of the angular velocity. This is called the magneto-rotational instability (MRI). It is particularly simple to analyze if the magnetic field is vertical, in which case the
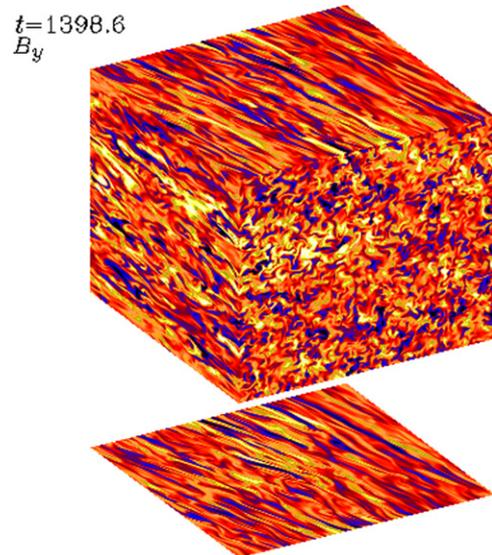
Figure 20. Toroidal magnetic field component displayed on the periphery of the computational domain (color coded). The size of the box is 2π in all three directions and the mesh size is 512^3 meshpoints. The gas is isothermal with a constant sound speed of $c_s = 5\Omega/k_1$. Viscosity and magnetic diffusivity are $\nu = \eta = 2.5 \times 10^{-4}\Omega/k_1^2$. Note that the magnetic field develops long thin structures aligned at some angle relative to the toroidal direction. Adapted from [253].

instability is purely axisymmetric. However, the same growth rates are obtained in the nonaxisymmetric case, if B points in the streamwise direction [86].

In the axisymmetric case the instability takes the form of so-called channel flows. In three dimensions the flow experiences strong shearing and hence small length scales in the cross-stream direction. This leads to the flow breaking up into what we loosely call fully developed turbulence. An example of such a flow is shown in figure 20, where periodic boundary conditions have been used in the vertical and azimuthal directions, and shearing-periodic boundary conditions in the cross-stream direction. No net magnetic flux has been applied [253]. Numerical simulations show, however, that the MRI is no longer excited when the magnetic Prandtl number is less than a critical value of the order of unity [254, 255]. A strong sensitivity on the magnetic Prandtl number has also been found for magnetized Taylor–Couette flow [256–260]. At present it is still unclear whether there is a real problem with the MRI in accretion disks when the magnetic Prandtl number is small. This issue may well be connected with the difficulty to excite small-scale dynamos at low magnetic Prandtl numbers [208–212]. On the other hand, astrophysical dynamos are large-scale dynamos, and they do not suffer from that particular difficulty [205, 261]. It would therefore be important to perform new MRI simulations in cases where large-scale dynamos are possible, i.e. in the presence of vertical density stratification, which can then lead to an α effect [262, 263]. In another recent study it has been shown that even without stratification, large-scale dynamo action is possible when pseudo-vacuum boundary conditions are used at top and bottom of the rotating shearing box [264]. A similar generation of mean fields has also been
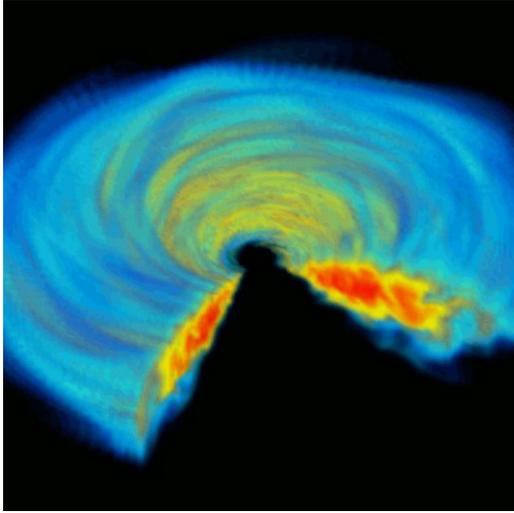
Figure 21. Visualization of the logarithmic density of an accretion torus around a black hole. Courtesy of John F Hawley [277].

found without rotation [239, 265–267]. Possible candidates for explaining the origin of large-scale fields in this case include the incoherent α-shear dynamo [268, 269] and the shear-current effect [270, 271]. For the latter effect to work, it is necessary that one of the off-diagonal components of the magnetic diffusivity tensor has a suitable sign, which may, however, not be the case [267, 272–274].

The MRI is generally thought to be responsible for driving turbulence in accretion disks, where $q = 3/2$. A more accurate representation of accretion disks is obtained with the inclusion of vertical and radial density stratification. The former case can be treated within the shearing-box approximation [275, 276] while the latter requires a global treatment [277–280]. In figure 21 we show a visualization of the logarithmic density of an accretion torus around a black hole.

An important diagnostic quantity of accretion disk simulations is the dimensionless turbulent disk viscosity, $\alpha_{SS} = \nu_t/c_s H$. Here, the subscripts SS refer to Shakura and Sunyaev [281], who employed this parametrization of turbulent viscosity ν_t in terms of local sound speed c_s and pressure scale height H. In the simulations, ν_t is normally estimated by the mean total horizontal stress, $\overline{\Pi}_{R\phi} = \overline{b_R b_\phi/\mu_0 - \rho u_R u_\phi}$, divided by the mean rate of strain resulting from the differential rotation, $\rho R \partial\Omega/\partial R$, where cylindrical coordinates, (R, ϕ, z), have been employed.

In comparison with local shearing box simulations, an important difference is that global simulations are capable of producing about 10 times larger values of α_{SS}. This is an immediate consequence of the larger field strength in global simulations rather than a difference in the intrinsic properties of local versus global disk simulations [277]. Another important outcome of global disk simulations is the fact that $\overline{\Pi}_{R\phi}$ is finite at the innermost marginally stable orbit. This is a property that is not normally taken into account in analytic models and continues to be debated in the literature [282, 283].

A number of new simulations have emerged in recent years. A major step was the combination of dust dynamics with self-gravity in the shearing box approximation [284, 285].

One of the remarkable results is the rapid formation of nearly Earth-sized bodies from boulders (figure 22). Even though the mass of what one might call protoplanet is growing, this body is also shedding mass during encounters with ambient material as it flows by. One might speculate that what is missing is the effect of radiative cooling of the protoplanet. This would allow the newly accreted material to lose entropy, become denser, and hence fall deeper into its potential well.

The main reason the simulations presented in [284] produce rapid growth is connected with the occurrence of sufficiently strong compressions caused by the turbulence. Once the compression is strong enough, self-gravity takes over and leads to a fully developed nonlinear collapse.

6.12. Effects of thermal and gravitational instabilities

A thermal instability may arise if a cooling term, $\Lambda(T)$, and a heating term, $\Gamma(T)$, are included on the right-hand side of the energy or entropy equation, i.e.

$$\rho T \frac{\mathrm{D}s}{\mathrm{D}t} = \cdots + \rho \Gamma(T) - \rho^2 \Lambda(T). \tag{83}$$

It is convenient to abbreviate the combination of the two terms on the right-hand side by $\rho \mathcal{L}$, where $\mathcal{L} = \Gamma - \rho \Lambda$. This allows us to state a sufficient condition for stability [163, 286]

$$\left(\frac{\partial \mathcal{L}}{\partial T}\right)_p > 0 \quad \text{(stability)}. \tag{84}$$

This means that when the temperature is increased, the corresponding cooling increases, bringing the temperature down again to the original value. In the presence of thermal diffusion, with $\boldsymbol{F}_{rad} = -K\boldsymbol{\nabla}T \neq 0$, the system can always be stabilized at small scales, i.e. for large wavenumbers, where eventually the thermal diffusion rate becomes faster than the cooling rate. For $\Gamma = \text{const}$ and $\Lambda \propto T^\beta$, the dispersion relation $\omega(k)$, is on sufficiently large scales (small wavenumbers) of the form [163, 286].

$$\omega = c_{iso} k \sqrt{1 - \beta^{-1}}, \tag{85}$$

where $c_{iso} = c_s/\sqrt{\gamma}$ is the isothermal sound speed. Evidently, for $\beta < 1$ sound waves become destabilized (ω becomes imaginary).

Numerical simulations [162, 163] have not been able to confirm alternative findings [287] that the thermal instability can lead to sustained turbulence. This is demonstrated in figure 23, which shows (here in the presence of shear) that the thermal instability leads to the development of patches with low temperature (100 K compared with 10 000 K outside those patches), but over time these patches merge until eventually a stable equilibrium is reached where a few big patches continue to coexist.

Another instability where sound waves are destabilized is the Jeans instability. Here the dispersion relation can be written in the form [288–291]

$$\omega^2 = c_s^2 k^2 - 4\pi G \rho, \tag{86}$$
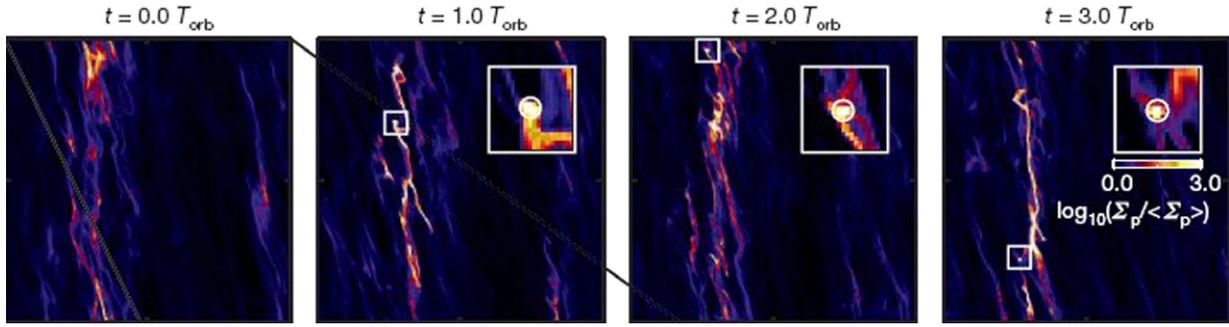
Figure 22. Simulations showing the total column density (gas plus all particle sizes) in the horizontal plane. The insets show the column density in logarithmic scale centered around the most massive cluster in the simulation. Time is given in terms of the number of orbits after turning on self-gravity. Courtesy of Anders Johansen [284].
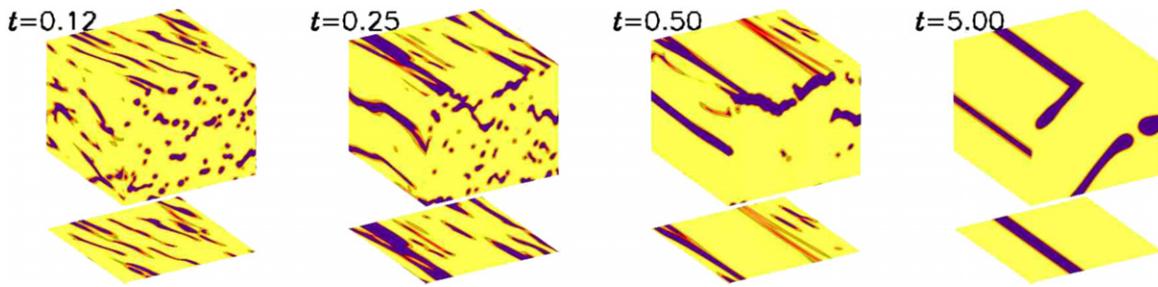
Figure 23. Visualization of $\ln T$ on the periphery of the box at different times, for $\nu = \chi = 5 \times 10^{-4}$ Gyr km^2 s^{-2} and 256^3 mesh points. $\langle \rho \rangle \approx 1.74 \times 10^{-24}$ g cm^{-3}, $\langle p \rangle \approx 24.2 \times 10^{-14}$ dyn and $\langle T \rangle \approx 8200$ K. Here $\Omega = 100$ Gyr^{-1} and $S = -\Omega$. For this run $k_F/k_1 = 32$ and $n_\rho/(c_s k_F) = 1.5$. The growth rate is about 190 Gyr^{-1}, which is somewhat larger than for the corresponding non-shearing run. Note that the initially produced structures are quickly sheared out. Adapted from [163].

where ρ is the local density of the gas. So, again, large scales become unstable. In an asymptotically thin layer such as an accretion disks or galaxies, the dispersion relation becomes [292]

$$\omega^2 = c_s^2 k^2 - 4\pi G \Sigma |\mathbf{k}|, \qquad (87)$$

where Σ is the local surface density. In the context of local accretion disk models, simulations suggest that this process can indeed lead to sustained turbulence [87, 293–295]. In simulations of star formation [181, 296–298], the Jeans instability leads to a continuous production of gravitationally bound structures corresponding to protostars. The stars that form have a broad distribution of masses, determined mainly by the statistics of mass fragmentation in supersonic MHD-turbulence [166]. The fraction of stars that are heavier than about 8 solar masses eventually (after a delay of up to a few tens of Myr) explode as supernovae. These supernovae contribute to sustaining the turbulence in the interstellar medium that ultimately causes additional generations of stars to be born [79, 197].

6.13. Supernova-driven turbulence

Interstellar turbulence is an example of astrophysical turbulent flows where the driving is usually modeled by a distributed body force. As discussed in section 3.4, the blast waves of supernova explosions provide energy input to the surrounding gas. These explosions drive gas flows with temperatures of around 10^8 K, but they also lead to strong compressions where

the gas cools rapidly to about 10^4 K. When the temperature is between 100 and 10^4 K the gas may, depending as details of the cooling curve $\Lambda(T)$, be thermally unstable [286]. This contributes to keeping the gas in the interstellar medium preferentially in one of two distinct temperature regimes (the so-called cold and warm phases; see section 6.12). The hot phase at temperatures $>10^6$ K is a direct result of heating by supernova explosions combined with a low cooling efficiency of the interstellar medium at that temperature. This is also borne out by various simulations [299–301]. Simulations show that the filling factor of the hot gas ($T > 10^6$ K) grows with height from 0.2–0.3 at the midplane to about 0.5–0.6 at a height of about 300 pc [299]. However, this result depends on the degree of correlation of supernovae in space and can reach 0.6 at the midplane for completely uncorrelated supernovae, as in an early analytic model [302]. Simulations have also been able to demonstrate that significant amounts of vorticity are being produced if the flow is sufficiently supersonic and if the baroclinic term is important [303, 304]. The presence of vorticity is advantageous for dynamo action; in fact, no dynamos have yet been found when the turbulence is irrotational [305].

There is now mounting evidence that for large Mach numbers the energy ratio of compressive to solenoidal velocities approaches 1/2 [166, 179, 306–309]. This can be explained if the mean square values of longitudinal and transversal velocity derivatives were equal, i.e. $\langle u_{x,x}^2 \rangle = \langle u_{x,y}^2 \rangle$. Assuming isotropy and that mixed terms cancel, this implies $\langle (\nabla \cdot \mathbf{u})^2 \rangle \approx 3 \langle u_{x,x}^2 \rangle$ and $\langle \boldsymbol{\omega}^2 \rangle \approx 6 \langle u_{x,y}^2 \rangle$, giving a ratio of
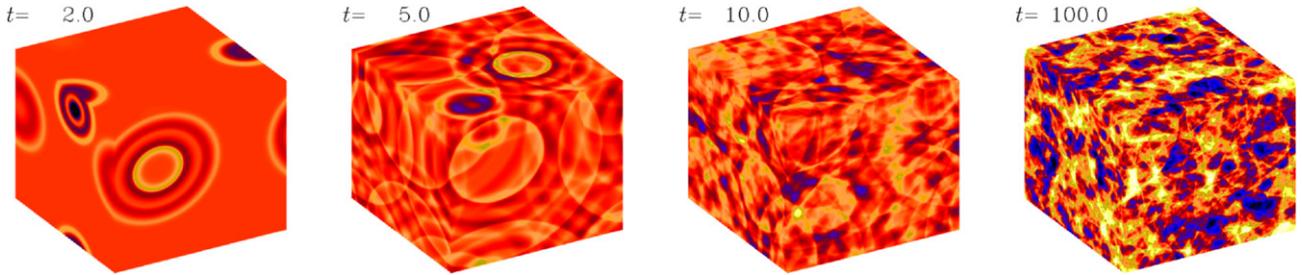
Figure 24. Visualization of $\ln \rho$ on the periphery of the box at different times, for $k_1 R = 0.2$, $Re = 50$, and 512^3 mesh points. Note that in the fully developed state individual expansion waves can hardly be recognized. Adapted from [305].

1/2 [307]. Whether or not this behavior is really universal needs to be seen. In the papers listed above the turbulence was forced with a substantial solenoidal component, so the issue of vorticity production was not addressed. In the following we discuss the opposite limit, where only compressive modes are driven and where no vorticity is produced.

6.14. Irrotational turbulence

Turbulence is usually thought of as being an ensemble of interacting eddies. If one associates eddies with vortices, then 'irrotational' turbulence must be a contradiction in terms. Nevertheless, irrotational turbulence can be regarded as an idealization that can serve its purpose in illustrating the difference to regular (vortical) turbulence.

Irrotational turbulence means that $\boldsymbol{\omega} = \boldsymbol{\nabla} \times \boldsymbol{u} = 0$. As explained in section 4.1, the $\boldsymbol{u} \times \boldsymbol{\omega}$ nonlinearity is absent and the only nonlinearity comes from the $\frac{1}{2}\boldsymbol{u}^2$ term. This causes a significant modification of the turbulent cascade, which is one of the reason why irrotational turbulence may be a contradiction in terms. Because of compressibility, however, vorticity can in principle be generated via the viscous term. Taking the curl of $\frac{1}{\rho}\boldsymbol{\nabla} \cdot \boldsymbol{\tau}$ in equation (33), and assuming $\nu = \text{const}$, gives

$$\boldsymbol{\nabla} \times \left(\frac{1}{\rho}\boldsymbol{\nabla} \cdot \boldsymbol{\tau} \right) = \nu\nabla^2\boldsymbol{\omega} + \boldsymbol{\nabla} \times [2\nu\mathbf{S} \cdot \boldsymbol{\nabla}\ln(\rho\nu)]. \quad (88)$$

Here, the first term vanishes if $\boldsymbol{\omega} = \mathbf{0}$, but the second term does not. As mentioned in section 6.13, simulations show that this term remains small in the limit $\nu \to 0$ [305]. In figure 24 we show visualizations of the logarithmic density in a simulation, which shows that the initially highly ordered expansion waves turn rapidly into a complicated pattern. The flow is here driven by a forcing function $\boldsymbol{f} = -\boldsymbol{\nabla}\phi$, where ϕ is a scalar function consisting of randomly placed Gaussians that change in regular time intervals, Δt, such that $\Delta t u_{\text{rms}} k_{\text{f}} \approx 0.25$.

Given that viscosity always perturbs the zero vorticity state slightly, and because the vorticity equation is analogous to the induction equation, one must ask whether a small initial vorticity could increase owing to an instability. However, at the Reynolds numbers achieved so far in simulations, neither vorticity nor magnetic fields have been found to increase spontaneously [305]. The suggestion that purely irrotational turbulence cannot produce dynamo action may be related to the finding that in vortical supersonic turbulence the critical magnetic Reynolds number for small-scale dynamo action

shows a 'bimodal' behavior with Mach number: for Mach numbers below unity the critical magnetic Reynolds number is about 35 to 40, and above unity it is about 70 to 80 [307]. Note, however, that the flow is here not purely irrotational, and that the ratio of $\langle(\boldsymbol{\nabla} \cdot \boldsymbol{u})^2\rangle$ and $\langle\boldsymbol{\omega}^2\rangle$ is about 1/2; see the discussion in section 6.13.

The results concerning vorticity production may be of relevance for other flows that can be described by spherical expansion waves. One example concerns phase transition bubbles that are believed to be generated in connection with the electroweak phase transition in the early universe [310, 311]. Here the equation of state is that of a relativistic fluid, $p = \rho c^2/3$, where c is the speed of light. Thus, again, there is no baroclinic term and no obvious source of vorticity. However, the relativistic equation of state may be modified at small length scales, but it is not clear that this can facilitate significant vorticity production.

7. Collective effects of turbulence

In this section we denote the velocity by a capital $\boldsymbol{U}$. Overbars indicate averages over one or two coordinate directions. They are not therefore regarded as spatial filters that are often used in the theory of large-eddy simulations [312, 313]. The definition of averages in terms of coordinate averages is convenient for interpreting simulation data. Other definitions of averages are possible. In analytic studies ensemble averages are commonly used. Departures from these averages are denoted by lower case symbols, i.e. $\boldsymbol{u} = \boldsymbol{U} - \overline{\boldsymbol{U}}$ and $\boldsymbol{b} = \boldsymbol{B} - \overline{\boldsymbol{B}}$ denote the fluctuating components of the velocity and magnetic field vectors. We discuss the properties of various correlators such as $\overline{u_i u_j}$, $\overline{u_i b_j}$ and $\overline{b_i b_j}$.

In general turbulence is non-isotropic. This can lead to the possibility of non-trivial components of the correlations tensors $\overline{u_i u_j}$, $\overline{u_i b_j}$ and $\overline{b_i b_j}$. The effects of these correlations on the evolution of the mean flow, $\overline{\boldsymbol{U}}$, and the mean magnetic field, $\overline{\boldsymbol{B}}$, or the mean passive scalar concentration, $\overline{C}$, are referred to as collective or mean-field effects of the turbulence. Even in the special case where $\overline{u_i u_j}$ is a diagonal tensor there is at least the phenomenon of turbulent diffusion, which will now be illustrated in connection with the passive scalar field.

7.1. Turbulent passive scalar diffusion

The relevant dynamics comes from the nonlinearity. In order to keep the discussion simple, we neglect the diffusion term.

The evolution equation of the passive scalar density per unit volume, $C = \rho\theta$, is then

$$\frac{\partial C}{\partial t} = -\frac{\partial}{\partial x_j}(C U_j),\tag{89}$$

cf equation (43). Again, we define the average concentration per unit volume as $\overline{C}$ and write $C = \overline{C} + c$. The evolution equation of $\overline{C}$ is obtained by averaging equation (89), i.e.

$$\frac{\partial \overline{C}}{\partial t} = -\frac{\partial}{\partial x_j}(\overline{C}\,\overline{U}_j + \overline{cu_j}).\tag{90}$$

The problematic term here is $\overline{cu_j}$, and the hope is that it can be expressed in terms of mean fields such as $\overline{C}$ and $\overline{U}$.

In order to derive an expression for $\overline{cu_j}$, we consider its evolution equation,

$$\frac{\partial}{\partial t}\overline{cu_j} = \overline{\dot{c}u_j} + \overline{c\dot{u}_j},\tag{91}$$

where dots denote partial time derivatives. The evolution equation for c is obtained by subtracting equation (90) from equation (89), which yields

$$\frac{\partial c}{\partial t} = -\frac{\partial}{\partial x_j}(\overline{C}u_j + c\overline{U}_j + N_j^{(c)}),\tag{92}$$

where $N_j^{(c)} = cu_j - \overline{cu_j}$ denotes nonlinear terms. In the absence of rotation, shear, viscosity or other linear effects, the momentum equation takes the form

$$\frac{\partial u_j}{\partial t} = N_j^{(u)}.\tag{93}$$

Assuming incompressibility and no mean flow, $\overline{U} = 0$, we have

$$\frac{\partial}{\partial t}\overline{cu_j} = -\tilde{\kappa}_{ij}^{(c)}\frac{\partial \overline{C}}{\partial x_j} + T_j^{(cu)},\tag{94}$$

where $\tilde{\kappa}_{ij}^{(c)} = \overline{u_i u_j}$ and $\boldsymbol{T}^{(cu)} = -\overline{[\boldsymbol{\nabla}N^{(c)}]u} + \overline{cN^{(u)}}$ denotes a triple correlation term.

Clearly, in the statistically steady state the two terms on the right-hand side of equation (94) must balance to zero, suggesting that $\boldsymbol{T}^{(cu)}$ cannot be neglected, as is assumed in the commonly used first-order smoothing approximation, when it is applied to the case of vanishing diffusivity ($\kappa_\theta = 0$); see [314] for a more detailed discussion. When κ_θ is large, the microscopic diffusion term involving $\kappa_\theta \nabla^2\theta$ in equation (43) or $\kappa_C \nabla^2 C$ in equation (89) needs to be restored. Since it is applied to the small-scale field with typical wavenumber k_f, the inclusion of the κ_θ term corresponds essentially to adding $-\kappa_\theta k_f^2 \overline{cu_j}$ on the right-hand side of equation (94). (This can be treated more accurately in Fourier space; see [315] for a corresponding treatment in the magnetic case.)

The closure assumption used in the τ approximation consists of the assumption that the triple correlations can be expressed in terms of the quadratic correlation, i.e.

$$T_j^{(cu)} = -\overline{cu_j}/\tau \quad \text{(closure assumption)}.\tag{95}$$

Inserting this into equation (94) yields

$$\left(1 + \tau\frac{\partial}{\partial t}\right)\overline{cu_j} = -\kappa_{ij}^{(c)}\frac{\partial \overline{C}}{\partial x_j},\tag{96}$$

where $\kappa_{ij}^{(c)} = \tau\tilde{\kappa}_{ij}^{(c)}$ corresponds to the usual turbulent diffusivity. This equation shows that, in the statistically steady state, there is a flux of passive scalar concentration in the direction of the negative gradient of $\overline{C}$. Note that the effect described here works also when the turbulence is isotropic, i.e. when $\overline{u_i u_j} = \frac{1}{3}\delta_{ij}\overline{u^2}$. In that case we have $\kappa_{ij}^{(c)} = \kappa_t^{(c)}\delta_{ij}$, where $\kappa_t^{(c)}$ is the scalar turbulent diffusivity of the mean passive scalar concentration. By assuming $\tau = (u_{\text{rms}}k_f)^{-1}$ we obtain $\kappa_t = \frac{1}{3}u_{\text{rms}}k_f^{-1}$. On the other hand, if $Pe \ll 1$, $\kappa_t^{(c)}$ is small and increases linearly with Pe such that $\kappa_t = \frac{1}{3}Pe\,u_{\text{rms}}k_f^{-1}$.

The effect discussed above is known as turbulent diffusion. It is a very basic effect that characterizes an enhanced diffusion experienced by the mean concentration. It is present whenever the typical scale of the mean field is large compared with the scale of the turbulence. This is the requirement of scale separation that needs to be made in order for a multiplicative relation in terms of the product of κ_t and $\boldsymbol{\nabla}\overline{C}$ to be valid. On the other hand, if the scale of the turbulence is comparable with the system size, a local connection between flux and gradient becomes invalid, and nonlocal expressions must be considered [316].

Let us now contrast the τ approximation with the first-order smoothing approximation, where equation (92) is still used, but the $N_j^{(c)}$ term is now neglected. Again, assuming $\overline{U} = 0$ and integrating in time, we have

$$c(\boldsymbol{x}, t) = -\int_0^t \frac{\partial \overline{C}(\boldsymbol{x}, t')}{\partial x_j}u_j(\boldsymbol{x}, t')\,\mathrm{d}t'.\tag{97}$$

Thus,

$$\overline{cu_i} = -\int_0^t \overline{u_i(t)u_j(t')}\frac{\partial \overline{C}(t')}{\partial x_j}\,\mathrm{d}t',\tag{98}$$

where we have dropped the common $\boldsymbol{x}$ dependence of all variables for clarity. This expression would be identical to equation (96) in the special case where

$$\overline{u_i(t)u_j(t')} = -\overline{u_i u_j}\exp[-(t-t')/\tau] \quad \text{for } t > t'.\tag{99}$$

This type of agreement is restricted to the simplest case when there is no contribution from the momentum equation. Examples where such agreement is lost include cases with rotation or shear, as well as analogous cases with magnetic field where there can be contributions from the Lorentz force [11, 317].

The concept of turbulent diffusion carries over to vector fields such as the velocity itself and the magnetic field. In these cases one talks about turbulent viscosity, ν_t, and turbulent magnetic diffusivity, η_t. The relevant correlations are then $\overline{u_i u_j}$ and $\overline{u_i b_j}$ that are being expressed in terms of negative gradient terms, i.e.

$$\overline{u_i u_j} = -\nu_t\left(\frac{\partial \overline{U}_i}{\partial x_j} + \frac{\partial \overline{U}_j}{\partial x_i}\right),\tag{100}$$

$$\overline{u_i b_j} = -\eta_t\frac{\partial \overline{B}_j}{\partial x_i}.\tag{101}$$

This last formula is quite analogous to the passive scalar case discussed in equation (96),

$$\overline{u_i c} = -\kappa_{\mathrm{t}}^{(c)} \frac{\partial \overline{C}}{\partial x_i}, \qquad (102)$$

where we have dropped the time derivative of $\overline{u_i c}$. The term on the right-hand side of equation (100) is similar to the expression for microscopic diffusion, see equation (32). The correlation that enters in the mean induction equation is

$$\overline{\mathcal{E}}_i = (\overline{\boldsymbol{u} \times \boldsymbol{b}})_i = \epsilon_{ijk}\overline{u_j b_k} = -\eta_{\mathrm{t}}(\boldsymbol{\nabla} \times \overline{\boldsymbol{B}})_i = -\eta_{\mathrm{t}}\mu_0 \overline{J}_i, \qquad (103)$$

which gives a contribution similar to the microscopic diffusion term in equation (58).

7.2. The α effect

Turbulence does not always act just diffusively. There can be non-diffusive effects, especially if the turbulence lacks local isotropy or at least parity invariance. If the flow is statistically non-mirrorsymmetric (for example helical) interesting effects can occur in connection with the evolution of the mean magnetic field. In particular, there are terms proportional to the mean magnetic field itself, i.e.

$$\overline{\boldsymbol{u} \times \boldsymbol{b}} = \alpha\overline{\boldsymbol{B}} - \eta_{\mathrm{t}}\boldsymbol{\nabla} \times \overline{\boldsymbol{B}}. \qquad (104)$$

This is the famous α effect [15, 318, 319] that is often invoked in order to understand the generation of large-scale magnetic fields in astrophysical bodies. The possibility of magnetic field generation can be seen by inserting equation (104) into the mean induction equation,

$$\frac{\partial \overline{\boldsymbol{B}}}{\partial t} = \boldsymbol{\nabla} \times (\overline{\boldsymbol{u} \times \boldsymbol{b}} - \eta\boldsymbol{\nabla} \times \overline{\boldsymbol{B}}). \qquad (105)$$

One can look for solutions proportional to $\exp(\mathrm{i}\boldsymbol{k} \cdot \boldsymbol{x} + \lambda t)$ and find that

$$\lambda = \pm\alpha k - (\eta + \eta_{\mathrm{t}})k^2, \qquad (106)$$

where $k = |\boldsymbol{k}|$; see, e.g., [11] for details. This shows that exponentially growing solutions exist on sufficiently large scales, i.e. on sufficiently small wavenumbers, $k < \alpha/\eta_{\mathrm{T}}$. Here we have introduced the total magnetic diffusivity, $\eta_{\mathrm{T}} = \eta + \eta_{\mathrm{t}}$.

Although this topic already reached text book level several decades ago [15, 318, 319], it continues to be a field of intense research—especially with regards to nonlinear feedback. Basic aspects of the α effect can best be explained in the context of isotropic turbulence. In that case the following expression for α has been derived [320–322]

$$\alpha = -\tfrac{1}{3}\tau\langle\boldsymbol{\omega} \cdot \boldsymbol{u}\rangle + \tfrac{1}{3}\tau\langle\boldsymbol{j} \cdot \boldsymbol{b}\rangle/\rho, \qquad (107)$$

which shows that α is determined by the residual between kinetic helicity of the small-scale velocity, $\langle\boldsymbol{\omega} \cdot \boldsymbol{u}\rangle$, and the normalized small-scale current density, $\langle\boldsymbol{j} \cdot \boldsymbol{b}\rangle/\rho$.

The $\langle\boldsymbol{j} \cdot \boldsymbol{b}\rangle$ term contributes to the nonlinear saturation of the dynamo. This is because the α effect produces magnetic helicity both at large and small scales such as to obey the magnetic helicity equation; see section 5.4. While

this can lead to a dramatic reduction of α in periodic or closed domains [213, 323], the quenching effect may be less extreme in the astrophysically relevant case of open domains where magnetic helicity can be transported out of the domain by magnetic helicity fluxes [324, 325]. The theory of these fluxes [326] shows that there can be several contributions to the flux. One such contribution is along the contours of constant shear [327, 328], but recent work has cast some doubt on whether such shear-driven magnetic helicity fluxes really exist [329]. Other contributions can come from advection [330] and diffusion [233]. For further aspects regarding nonlinear dynamo theory we refer to a review dedicated to recent developments; see [11].

The presence of shear provides an additional induction effect that usually contributes to the dynamo. In order to estimate the relative importance of these effects, and to estimate whether a large-scale dynamo is excited, one needs to know the values of some relevant non-dimensional numbers that characterize the magnitude of α effect and shear,

$$C_\alpha = \alpha/\eta_{\mathrm{T}}k_{\mathrm{m}}, \qquad C_\Omega = \Delta\Omega/\eta_{\mathrm{T}}k_{\mathrm{m}}^2, \qquad (108)$$

where k_{m} is an estimate for the relevant wavenumber of the dynamo that fits into the domain and $\Delta\Omega$ is the absolute differential rotation. In the case of the Sun it is about 30% of the average angular velocity. Let us quantify the degree of helicity in the turbulence as $\epsilon_{\mathrm{f}} = \langle\boldsymbol{\omega} \cdot \boldsymbol{u}\rangle/k_{\mathrm{f}}u_{\mathrm{rms}}^2$, where $k_{\mathrm{f}} = \omega_{\mathrm{rms}}/u_{\mathrm{rms}}$, and assume $\eta_{\mathrm{t}} \gg \eta$, we find

$$C_\alpha \approx \epsilon_{\mathrm{f}}k_{\mathrm{f}}/k_{\mathrm{m}}. \qquad (109)$$

Thus, the efficiency of the α effect depends on how helical the turbulence is and on the amount of scale separation available. A so-called α^2 dynamo is possible when C_α exceeds a critical value of the order of unity.

Often C_α is too small, and then the presence of shear can help us to produce large-scale dynamo action. We assume that the shear is a significant fraction, $q = \Delta\Omega/\Omega$, of the mean angular velocity Ω which, in turn, is often expressed as the Coriolis number, $Co = 2\Omega/u_{\mathrm{rms}}k_{\mathrm{f}}$. We may then estimate

$$C_\Omega \approx \tfrac{3}{2}q\,Co\,(k_{\mathrm{f}}/k_{\mathrm{m}})^2. \qquad (110)$$

A large-scale dynamo of $\alpha\Omega$ type is excited when the product $C_\alpha C_\Omega$ exceeds another critical value which is also of the order of unity. For a homogeneous dynamo, the critical value of $C_\alpha C_\Omega$ for plane wave solutions is 2.

In conclusion, we see that the possibility of large-scale dynamo action depends critically on the scale separation ratio, $k_{\mathrm{f}}/k_{\mathrm{m}}$. It is therefore important that the domain is big enough to contain a significant number of turbulent eddies. Simulations have now confirmed the possibility of large-scale dynamo action in cases of forced turbulence, convective turbulence and for turbulence driven in turn by magnetic fields through the magneto-rotational instability.

7.3. Lambda effect

An effect somewhat analogous to the α effect is the Λ effect. It parametrizes the dependence of the Reynolds stress on the

mean angular velocity [331, 332] as

$$\overline{u_i u_j} = \Lambda_{ijk} \overline{\Omega}_k + \mathcal{N}_{ijkl} \frac{\partial \overline{U}_k}{\partial x_l}, \qquad (111)$$

where $\overline{\Omega} = \overline{U}_\phi / (r \sin \theta)$ is the *local* angular velocity (not the Ω_0 used earlier in connection with the transformation to a rigidly rotating frame of reference). The second term in equation (111) is just the tensorial form of the turbulent viscosity; see equation (100). The first one exists already in the presence of uniform rotation. It is this term, balanced against the resulting turbulent viscosity term, that drives and maintains non-uniformity in the mean angular velocity [333–335]. There are two important contributions to the Λ effect, a vertical and a horizontal one that quantify the $r\phi$ and $\theta\phi$ components of the Reynolds stress, respectively. In particular, we have, in spherical coordinates, (r, θ, ϕ),

$$\Lambda_{ijk} \Omega_k = \begin{pmatrix} 0 & 0 & V \sin \theta \\ 0 & 0 & H \cos \theta \\ V \sin \theta & H \cos \theta & 0 \end{pmatrix}. \qquad (112)$$

Here, V and H are functions of r and θ that depend on the anisotropy of the turbulence. Using the first-order smoothing approximation one finds [331, 332]

$$V = \tau (\overline{u_\phi^2} - \overline{u_r^2}), \qquad (113)$$

$$H = \tau (\overline{u_\phi^2} - \overline{u_\theta^2}). \qquad (114)$$

For small turbulent Taylor numbers, $Ta_{\mathrm{turb}} = \langle 2\Omega R^2/\nu_{\mathrm{t}} \rangle^2$, one finds for $H = 0$ and $V \neq 0$ that the Ω contours are purely radial, while for $V = 0$ and $H \neq 0$ the Ω contours are purely spoke-like. For $V = \nu_{\mathrm{t}}(\sin^2 \theta - 1)$ and $H = \nu_{\mathrm{t}} \sin^2 \theta$ one finds disk-shaped Ω contours. For $V = \nu_{\mathrm{t}}(\frac{5}{4} \sin^2 \theta - 1)$ and $H = \frac{5}{4} \nu_{\mathrm{t}} \sin^2 \theta$ one finds approximately spoke-like contours. However, those contours can change significantly with increasing values of Ta_{turb}, which leads to the development of cylindrical Ω contours. This is explained by the Taylor–Proudman theorem, as will be explained below.

The development of differential rotation is well established and is routinely seen in direct simulations of convective turbulence in rotating shells [55, 336, 337]. The existence of the Λ effect has been verified in local Cartesian simulations and the magnitude and spatial dependence have been determined [338]. Solutions of the equations for $\overline{U}$ have shown differential rotation roughly similar to what is found for the Sun using helioseismology. However, both DNS and solutions of the mean-field equations show a tendency toward Ω contours being constant along cylinders, which is not the case in the Sun. The cylindrical contours are the result of a feedback from the production of meridional circulation modifying the angular velocity contours. This leads to an approximate geostrophic balance, where

$$\overline{U} \cdot \nabla \overline{U} + \overline{\rho}^{\,-1} \nabla \overline{p} = 0. \qquad (115)$$

In the barotropic case, when ∇T and ∇s are parallel to each other, taking the curl of equation (115) yields

$\nabla \times (\overline{U} \cdot \nabla \overline{U}) = 0$. Assuming that the mean flow is purely toroidal, i.e. $\overline{U} = (0, 0, \overline{\Omega} r \sin \theta)$, we have

$$r \sin \theta \frac{\partial \overline{\Omega}^2}{\partial z} = 0. \qquad (116)$$

So, if viscous and inertial terms are small, which is indeed the case for rapid rotation, then $\partial \overline{\Omega}^2/\partial z$ must be small, so $\overline{\Omega}$ would be constant along cylinders [333]. This is also what is seen in mean-field models with Λ effect [339, 340].

It is generally believed that the main reason for $\overline{\Omega}$ not having cylindrical contours in the Sun is connected with the presence of the baroclinic term [123, 333]. The highest resolution simulations available today produce $\overline{\Omega}$ contours that are still too close to being constant along cylinders [55, 57, 121, 341–344]. These simulations do not quite reach the solar surface, so they cannot show the near-surface shear layer where the rotation rate drops by more than 20 nHz over the last 30 Mm just below the surface. Nevertheless, these simulations reproduce some important features of the Sun's differential rotation such as a more rapidly spinning equator.

Mean-field simulations using the Λ effect show surprisingly good agreement with the helioseismologically inferred $\overline{\Omega}$ pattern [340, 345], and they are also beginning to reproduce the near-surface shear layer; see figure 25. In these models it is indeed the baroclinic term that is responsible for causing the departure from cylindrical contours. This, in turn, is caused by an anisotropy of the turbulent heat conductivity which causes a slight enhancement in temperature and specific entropy at the poles. In the bulk of the convection zone the specific entropy is nearly constant while the temperature varies significantly in the vertical direction. It is therefore primarily the latitudinal specific entropy variation that determines the baroclinic term. This can be demonstrated by focusing on the contribution from the radial temperature and the latitudinal specific entropy gradients; see equations (49) and (53), i.e.

$$r \sin \theta \frac{\partial \overline{\Omega}^2}{\partial z} \approx -\hat{\phi} \cdot \overline{\nabla T \times \nabla s} \approx -\frac{1}{r} \frac{\partial \overline{T}}{\partial r} \frac{\partial \overline{s}}{\partial \theta} < 0. \qquad (117)$$

The inequality shows that negative values of $\partial \overline{\Omega}^2/\partial z$ require that the pole is slightly warmer than the equator ($\partial \overline{s}/\partial \theta < 0$). However, this effect is so weak that it cannot at present be observed. Allowing for these conditions in a simulation may require particular care in the treatment of the outer boundary conditions, or perhaps at the bottom of the convection zone in the tachocline. Given that the turbulent convective flux is proportional to $-\chi_{ij} \nabla_j \overline{s}$, a negative $\partial \overline{s}/\partial \theta$ can be produced from a positive enthalpy flux with a positive value of $\chi_{r\theta}$. This is indeed compatible with theory that predicts a rotational influence on the turbulence which makes χ_{ij} anisotropic [317, 346]. One expects

$$\chi_{ij} = \chi_{\mathrm{t}} \delta_{ij} + \chi_\Omega \epsilon_{ijk} \Omega_k^{(0)} + \chi_{\Omega\Omega} \Omega_i^{(0)} \Omega_j^{(0)}, \qquad (118)$$

where we have used superscripts (0) interchangeably with subscripts 0 to denote the rotation vector in a rotating frame of reference. In spherical polar coordinates we have $\Omega_0 = (\cos \theta, -\sin \theta, 0)$, so $\chi_{r\theta} = -\chi_{\Omega\Omega} \sin \theta \cos \theta \, \Omega_0^2$.
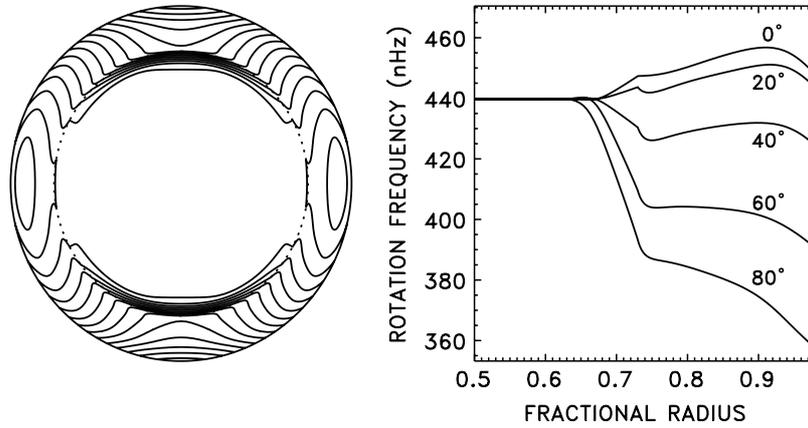
Figure 25. Contours (left) and radial profiles (right) of differential rotation in a model of the Sun. Note the presence of radial deceleration near the surface layers (fractional radius above 0.9). Adapted from [340].

Simulations confirm that $\chi_{\Omega\Omega}$ is negative, but only when the scale of the mean field is comparable to that of the fluctuating velocity field [317], which is somewhat unexpected. An alternative idea was advanced by Rempel [347], who was able to reproduce solar-like $\overline{\Omega}$ contours by imposing a suitable latitudinal $\overline{s}$ variation at the bottom of the convection zone.

In the discussion above we ignored in the last step the correlation between specific entropy and temperature fluctuations, i.e. a contribution from the term $\overline{\nabla T' \times \nabla s'}$ where primes denote fluctuations. Such correlations, if of suitable sign, might provide yet another explanation for a non-zero value of $\partial\overline{\Omega}^2/\partial z$.

It is in principle also possible that the differential rotation could entirely be driven by the baroclinic term [348, 349]. However, quantitative calculations showed that this effect on its own would be too small [332, 350].

7.4. Turbulent transport coefficients from simulations

In the past few years significant progress has been made in determining tensor components such as κ_{ij}, α_{ij} and η_{ijk} from local turbulence simulations. The recommended approach is what is referred to as the test-field method [351, 352]. This method is not to be confused with the test-field *model* that was introduced by Kraichnan [353] as a closure approach.

In the test-field method one solves numerically the evolution equation (92) for the fluctuations of the passive scalar concentration c, or a corresponding equation for fluctuations of the magnetic field b to obtain the magnetic transport coefficients. These equations are inhomogeneous in c or b and have terms of the form $\nabla \cdot (u\overline{C})$ or $\nabla \times (u \times \overline{B})$. Here the mean fields $\overline{C}$ and $\overline{B}$ are now replaced by test fields. The best studied cases are for periodic boundary conditions and then the test fields are taken to be $\overline{C}^{cx} = \cos kx$ or $\overline{C}^{sx} = \sin kx$, and similarly for the y and z directions. For each test field one evaluates the corresponding flux, $\overline{u_j c^{pq}}$, and computes

$$\kappa_{ij} = -\langle \cos kx_j \overline{\mathcal{F}}_i^{js} - \sin kx_j \overline{\mathcal{F}}_i^{jc} \rangle / k, \qquad (119)$$

for $i, j = x, y, z$. Here, angular brackets denote volume averages. Using this method it has now been possible to

compute the dependence of the coefficients κ_t, κ_Ω and $\kappa_{\Omega\Omega}$ in an equation analogous to equation (118), where χ has been replaced by κ. A similar equation can also be written down for the case where the anisotropy is caused by an applied magnetic field.

In the presence of a linear shear flow with $\overline{U}_{i,j} = $ const, it has proved advantageous to express κ_{ij} in terms of the tensors $\overline{\mathsf{S}}_{ij} = \frac{1}{2}(\overline{U}_{i,j} + \overline{U}_{j,i})$ and $\overline{\mathsf{A}}_{ij} = \frac{1}{2}(\overline{U}_{i,j} - \overline{U}_{j,i})$. The corresponding representation of κ_{ij} has been found to be of the form

$$\kappa_{ij} = \kappa_t\delta_{ij} + \kappa_{\mathsf{S}}\overline{\mathsf{S}}_{ij} + \kappa_{\mathsf{A}}\overline{\mathsf{A}}_{ij} + \kappa_{\mathsf{SS}}(\overline{\mathsf{S}}\,\overline{\mathsf{S}})_{ij} + \kappa_{\mathsf{AS}}(\overline{\mathsf{A}}\,\overline{\mathsf{S}})_{ij}. \qquad (120)$$

There are indications that, in addition to κ_t, only the coefficients κ_{S} and κ_{SS} are important, while κ_{A} and κ_{AS} are either small or become small at larger Peclet number [354].

The test-field method also allows one to compute turbulent transport coefficients where the assumption of scale separation is not obeyed, or where the mean quantities vary on time scales comparable to the turnover time of the turbulence. In those cases we have to replace the multiplications in equations (100)–(102) by convolutions with integral kernels of the corresponding transport coefficients, e.g.

$$\overline{u_i c}(x, t) = - \int \kappa_t^{(c)}(x, x', t, t') \frac{\partial\overline{C}(x', t')}{\partial x_i'} \, \mathrm{d}^3 x' \, \mathrm{d}t', \qquad (121)$$

and likewise for the other equations. If the system is homogeneous and statistically stationary, the kernels depend only on the differences $x - x'$ and $t - t'$. In such cases the convolution in real space becomes a multiplication in Fourier space. The test-field method yields directly the Fourier-transformed kernels if the test fields consist of sine and cosine functions [316], and if they are made time-dependent [355]. By changing the wavenumber and/or the frequency of the test fields one can then obtain the full wavenumber and frequency dependence of the Fourier-transformed kernel functions that enables one to compute the kernels in real space via Fourier transformation.

It turns out that, for a range of quite different physical circumstances, the k dependence can well be fitted to the form of a Lorentzian proportional to $[1 + (ak/k_f)^2]^{-1}$, where a is a fit parameter of the order of unity. The frequency

dependence can be fitted to a function whose Fourier transform corresponds to a multiplicative contribution to the kernel of the form $e^{-t/\tau}\cos\omega_0 t$, where ω_0 and τ^{-1} are fit parameters that are of the order of the inverse turnover time, $u_{rms}k_f$.

This type of analysis has been carried out both for turbulent transport coefficients of both passive scalars and magnetic fields. In the magnetic case there is, in addition to the turbulent magnetic diffusivity tensor, also the α tensor [267]. Using test fields proportional to sine and cosine functions, one can compute α and η_t simultaneously. It turns out that in the kinematic regime α and η_t reach asymptotic values for $Re_M > 1$ where $\alpha \approx \alpha_0$ and $\eta_t \approx \eta_{t0}$ with [356]

$$\alpha_0 = \tfrac{1}{3}\tau\langle\boldsymbol{\omega}\cdot\boldsymbol{u}\rangle, \quad \eta_{t0} = \tfrac{1}{3}\tau\langle\boldsymbol{u}^2\rangle,$$

$$\text{where} \quad \tau = (u_{rms}k_f)^{-1}. \tag{122}$$

Both show similar behavior as far as their wavenumber and frequency dependence is concerned [357].

Anisotropies of the flow yield anisotropies in the α and η tensors. In addition, since the magnetic field is an active vector, it backreacts on the flow and makes it anisotropic even if it was otherwise isotropic. It turns out that the α and η tensors are of the form

$$\alpha_{ij} = \alpha_1\delta_{ij} + \alpha_2\hat{B}_i\hat{B}_j, \qquad \eta_{ij} = \eta_1\delta_{ij} + \eta_2\hat{B}_i\hat{B}_j, \tag{123}$$

where we have assumed that only the unit vector of the mean field, $\hat{B} = \overline{B}/|\overline{B}|$, is crucial. Simulations with the test-field method have revealed that in the quenched state α_1 and α_2 have opposite sign [358]. The test-field method has been used to compute the dependence of η_t and η_t on Re_M in the nonlinearly saturated state for $\overline{B} \sim B_{eq}$, where B_{eq} is the field strength where magnetic and kinetic energies are in equilibrium. It turns out that at large Re_M the effects of α and η_t tend to balance each other. Furthermore, η_t does not show a sharp decline like Re_M^{-1}, as would be the case in two dimensions, but, even though Re_M is already around 600, there remains a weak decrease of η_t, without any obvious indications that this trend might level off (figure 26).

When the α and η tensors are multiplied by $\overline{B}$, the result is [358]

$$\alpha_{ij}\overline{B}_j - \mu_0\eta_{ij}\overline{J}_j = (\alpha_1 + \alpha_2 - \eta_2 k_m)\overline{B}_i - \eta_1\mu_0\overline{J}_i, \tag{124}$$

where $k_m = \mu_0\overline{J}\cdot\overline{B}/\overline{B}^2$ is an effective wavenumber of the mean field. This shows that the tensorial nature of α is unimportant in this context. However, this changes when considering passive vector equations that are equivalent to the induction equation, with a passive vector field $\tilde{B}$ that is similar to the actual magnetic field, but it has no effect on the motions. Such a passive vector field can display dynamo action and can continue to grow even when the underlying velocity field corresponds to that of a nonlinearly saturated dynamo. This phenomenon was first observed for turbulent convective dynamos [359] and then confirmed for laminar dynamos generating a mean field that is an eigenvector of the matrix $\hat{B}_i\hat{B}_j$ with vanishing eigenvalue. Thus, given that α_2/α_1 is negative, such fields remain unquenched for a velocity field or an α tensor that corresponds to a saturated dynamo [360].
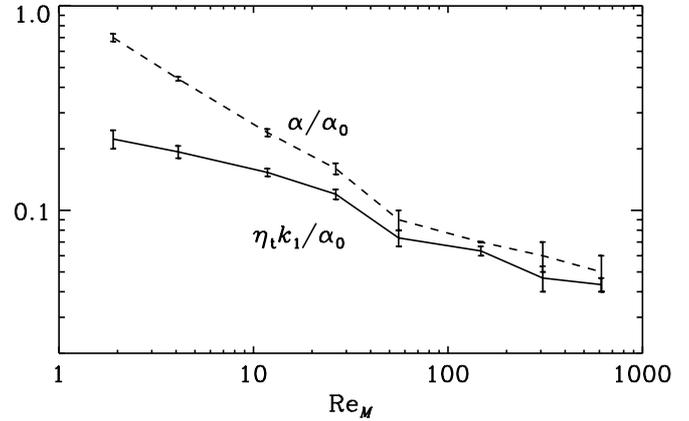

Figure 26. Re_M-dependence of α and $\tilde{\eta}_t$. Both curves are normalized by α_0. Adapted from [358].

8. Concluding remarks

Over the past few decades hydrodynamic and magnetohydrodynamic simulations have become a frequently used tool in astrophysics research. This trend is surely going to continue. As an example of the importance of turbulence considerations we mention here the well-established field of stellar structure, which has recently been the subject of intense debate, because fits to three-dimensional time-dependent turbulent model atmospheres have led (mostly due to non-3D effects!) to a significantly lower estimate of the solar abundance of heavier elements. Although this issue is not yet settled, it is clear that the results from three-dimensional turbulence simulations will continue to provide valuable input to the debate.

Even the radially symmetric (one-dimensional) models of stellar interiors are bound to be soon superseded or amended by higher-dimensional models. Clearly, the vast range of time and length scales between those of turbulent convection of stars and those of stellar structure and evolution necessitate a proper understanding of the collective or mean-field effects that are controlled by various correlators discussed in section 7. Obviously, we were only able to expose a small part of the many recent developments in this field. Quite frequently astrophysical turbulence involves magnetic fields, and often many more ingredients such as dust, chemicals, cosmic rays and coupling to radiation. Instead of simply neglecting such additional features, one may attempt to incorporate them into stellar evolution models using a mean-field approach. The transport properties depend on rotation, shear and magnetic field in ways that are reasonably well understood now. This is important, for example, in understanding the dependence of the lithium abundance of young stars on their rotation rate [361, 362].

Astrophysical turbulence concerns usually extreme parameter regimes: large Reynolds and/or Mach numbers, very large or very small Prandtl numbers, as well as extreme density and temperature contrasts. This motivates thorough studies of turbulence in regimes that are not otherwise addressed. This can either provide broader support for certain turbulence theories, or it can more clearly highlight problems that would be otherwise overlooked. In this sense astrophysical

turbulence research is not just the application of regular turbulence theory, but it can also provide complementary insights of broader relevance also for other research fields.

One of the aspects where astrophysical turbulence encounters an as yet unsettled issue is the question how compressibility really enters the theory. We have seen some ambiguity in the proper definition of the kinetic energy where, empirically, the spectrum of $\rho^{1/3} \boldsymbol{u}$ appears to be closest to the case of incompressible turbulence. There are several related issues in the context of mean-field theory. For example, the equation for the magnetic α effect in equation (107) contains a ρ factor, but since this equation was derived for the compressible case, it is not clear whether ρ should enter inside or outside the average of $\boldsymbol{j} \cdot \boldsymbol{b}$ when ρ is non-uniform or strongly fluctuating. Another occurrence of compressibility effects could be in the relation between the enthalpy flux and the specific entropy gradient. Finally, let us also mention here the issue of the baroclinic term, which can be important in the production of vorticity and shaping the form of the differential rotation contours in the Sun. There could potentially be systematic corrections resulting from the fluctuations of specific entropy and temperature. This and other effects might be responsible for causing a departure from cylindrical Taylor–Proudman contours of $\Omega(r, \theta)$ in the Sun.

There are several other quadratic correlation functions that need to be modeled more accurately. One is the current helicity flux involving terms of the form $\boldsymbol{E} \times \boldsymbol{J}$, for example. Other examples include Reynolds and Maxwell stresses and their dependence not only on the mean velocity, as discussed above, but also on the magnetic field. This quadratic nonlinearity means that the standard test-field method cannot be used, but possibly some kind of modification of it might work.

Acknowledgments

References

[1] Biskamp D 2003 *Magnetohydrodynamic Turbulence* (Cambridge: Cambridge University Press)

[2] Spiegel E A 1971 Convection in stars: I. Basic Boussinesq convection *Ann. Rev. Astron. Astrophys.* **9** 323–52

[3] Spiegel E A 1972 Convection in stars. II. Special effects *Ann. Rev. Astron. Astrophys.* **10** 261–304

[4] Busse F H 1978 Non-linear properties of thermal convection *Rep. Prog. Phys.* **41** 1929–67

[5] Spruit H C, Nordlund Å and Title A M 1990 Solar convection *Ann. Rev. Astron. Astrophys.* **28** 263–301

[6] Frisch U 1995 *Turbulence. The Legacy of A N Kolmogorov.* (Cambridge: Cambridge University Press)

[7] Goldstein M L, Roberts D A and Matthaeus W H 1995 Magnetohydrodynamic turbulence in the solar wind *Ann. Rev. Astron. Astrophys.* **33** 283–326

[8] Davidson P A 2004 *Turbulence: an Introduction for Scientists and Engineers* (Oxford: Oxford University Press)

[9] Elmegreen B G and Scalo J 2004 Interstellar turbulence: I. Observations and processes *Ann. Rev. Astron. Astrophys.* **42** 211–73

[10] Scalo J and Elmegreen B G 2004 Interstellar turbulence: II. Implications and effects *Ann. Rev. Astron. Astrophys.* **42** 275–316

[11] Brandenburg A and Subramanian K 2005 Astrophysical magnetic fields and nonlinear dynamo theory *Phys. Rep.* **417** 1–209

[12] Lighthill M J 1955 The effect of compressibility on turbulence *IAU Symp. (Cambridge, UK)* vol 2 (Amsterdam: North-Holland) pp 121–80

[13] Kritsuk A G, Norman M L, Padoan P and Wagner R 2007 The statistics of supersonic isothermal turbulence *Astrophys. J.* **665** 416–31

[14] Brandenburg A, Dobler W and Subramanian K 2002 Magnetic helicity in stellar dynamos: new numerical experiments *Astron. Nachr.* **323** 99–122

[15] Moffatt H K 1978 *Magnetic Field Generation in Electrically Conducting Fluids* (Cambridge: Cambridge University Press)

[16] Corrsin S 1951 On the spectrum of isotropic temperature fluctuations in an isotropic turbulence *J. Appl. Phys.* **22** 469–73

[17] Dobler W, Haugen N E, Yousef T A and Brandenburg A 2003 Bottleneck effect in three-dimensional turbulence simulations *Phys. Rev.* E **68** 026304

[18] Kaneda Y, Ishihara T, Yokokawa M, Itakura K and Uno A 2003 Energy dissipation rate and energy spectrum in high resolution direct numerical simulations of turbulence in a periodic box *Phys. Fluids* **15** L21–4

[19] Haugen N E L and Brandenburg A 2006 Hydrodynamic and hydromagnetic energy spectra from large eddy simulations *Phys. Fluids* **18** 075106

[20] Falkovich G 1994 Bottleneck phenomenon in developed turbulence *Phys. Fluids* **6** 1411–4

[21] Wyngaard J C 1968 Measurement of small-scale turbulence structure with hot wires *J. Phys. E: Sci. Instrum.* **1** 1105–8

[22] Benzi R, Ciliberto S, Tripiccione R, Baudet C, Massaioli F and Succi S 1993 Extended self-similarity in turbulent flows *Phys. Rev.* E **48** R29–R32

[23] She Z-S and Leveque E 1994 Universal scaling laws in fully developed turbulence *Phys. Rev. Lett.* **72** 336–9

[24] Boldyrev S 2002 Kolmogorov–Burgers model for star-forming turbulence *Astrophys. J.* **569** 841–5

[25] Boldyrev S, Nordlund Å and Padoan P 2002 Supersonic turbulence and structure of interstellar molecular clouds *Phys. Rev. Lett.* **89** 031102

[26] Boldyrev S, Nordlund Å and Padoan P 2002 Scaling relations of supersonic turbulence in star-forming molecular clouds *Astrophys. J.* **573** 678–84

[27] Politano H and Pouquet A 1995 Model of intermittency in magnetohydrodynamic turbulence *Phys. Rev.* E **52** 636–41

[28] Politano H and Pouquet A 1998 von Kármán–Howarth equation for magnetohydrodynamics and its consequences on third-order longitudinal structure and correlation functions *Phys. Rev.* E **57** R21–4

[29] Siefert M and Peinke J 2004 Different cascade speeds for longitudinal and transverse velocity increments of small-scale turbulence *Phys. Rev.* E **70** 015302

[30] Pearson B R, Yousef T A, Haugen N E L, Brandenburg A and Krogstad P-Å 2004 Delayed correlation between turbulent energy injection and dissipation *Phys. Rev.* E **70** 056301

[31] Miller J M, Raymond J, Fabian A, Steeghs D, Homan J, Reynolds C, van der Klis M and Wijnands R 2006 The magnetic nature of disk accretion onto black holes *Nature* **441** 953–5

[32] Parker E N 1958 Dynamics of the interplanetary gas and magnetic fields *Astrophys. J.* **128** 664–76

[33] Shore S N 1992 *An Introduction to Astrophysical Hydrodynamics* (San Diego, CA: Academic)

[34] Choudhuri A R 1998 *The Physics of Fluids and Plasmas: An Introduction for Astrophysicists* (Cambridge: Cambridge University Press)

[35] Phillips J L, Bame S J, Feldman W C, Gosling J T, Hammond C M, McComas D J, Goldstein B E and Neugebauer M 1995 ULYSSES solar wind plasma observations during the declining phase of solar cycle 22 *Adv. Space Res.* **16** 85–94

[36] Tu C-Y and Marsch E 1995 MHD structures, waves and turbulence in the solar wind: observations and theories *Space Sci. Rev.* **73** 1–210

[37] Smith C W, Hamilton K, Vasquez B J and Leamon R J 2006 Dependence of the dissipation range spectrum of interplanetary magnetic fluctuations on the rate of energy cascade *Astrophys. J. Lett.* **645** L85–8

[38] Howes G G, Dorland W, Cowley S C, Hammett G W, Quataert E, Schekochihin A A and Tatsuno T 2008 Kinetic simulations of magnetized turbulence in astrophysical plasmas *Phys. Rev. Lett.* **100** 065004

[39] Sahraoui F, Goldstein M L, Robert P and Khotyaintsev Y V 2009 Evidence of a cascade and dissipation of solar-wind turbulence at the electron gyroscale *Phys. Rev. Lett.* **102** 231102

[40] Matthaeus W H, Goldstein M L and Smith C 1982 Evaluation of magnetic helicity in homogeneous turbulence *Phys. Rev. Lett.* **48** 1256–9

[41] Matthaeus W H and Goldstein M L 1982 Measurement of the rugged invariants of magnetohydrodynamic turbulence in the solar wind *J. Geophys. Res.* **87** 6011–28

[42] Freeman J W 1988 Estimates of solar wind heating inside 0.3 AU *Geophys. Res. Lett.* **15** 88–91

[43] Smith C W, Matthaeus W H, Zank G P, Ness N F, Oughton S and Richardson J D 2001 Heating of the low-latitude solar wind by dissipation of turbulent magnetic fluctuations *J. Geophys. Res.* **106** 8253–72

[44] Biskamp D, Schwarz E and Drake J F 1996 Two-dimensional electron magnetohydrodynamic turbulence *Phys. Rev. Lett.* **76** 1264–7

[45] Schekochihin A A, Cowley S C, Dorland W, Hammett G W, Howes G G, Quataert E and Tatsuno T 2009 Astrophysical gyrokinetics: kinetic and fluid turbulent cascades in magnetized weakly collisional plasmas *Astrophys. J. Suppl.* **182** 310–77

[46] Galtier S and Buchlin E 2007 Multiscale Hall-magnetohydrodynamic turbulence in the solar wind *Astrophys. J.* **656** 560–6

[47] Alexandrova O, Carbone V, Veltri P and Sorriso-Valvo L 2008 Small-scale energy cascade of the solar wind turbulence *Astrophys. J.* **674** 1153–7

[48] van Noort M, Rouppe van der Voort L and Löfdahl M G 2005 Solar image restoration by use of multi-frame blind de-convolution with multiple objects and phase diversity *Sol. Phys.* **228** 191–215

[49] Asplund M 2005 New light on stellar abundance analyses: departures from LTE and homogeneity *Ann. Rev. Astron. Astrophys.* **43** 481–530

[50] Caffau E, Ludwig H-G, Steffen M, Ayres T R, Bonifacio P, Cayrel R, Freytag B and Plez B 2008 The photospheric solar oxygen project: I. Abundance analysis of atomic lines and influence of atmospheric models *Astron. Astrophys.* **488** 1031–46

[51] Asplund M, Grevesse N, Sauval A J and Scott P 2009 The chemical composition of the Sun *Ann. Rev. Astron. Astrophys.* **47** 481–522

[52] Brandenburg A, Chan K L, Nordlund Å and Stein R F 2005 Effect of the radiative background flux in convection *Astron. Nachr.* **326** 681–92

[53] Stein R F, Nordlund Å, Georgoviani D, Benson D and Schaffenberger W 2009 *Supergranulation-Scale Convection Simulations* (*Astronomical Society of the Pacific Conference Series* vol 416) (San Francisco, CA: Astron. Soc. Pacific) pp 421–6

[54] Busse F H 1970 Thermal instabilities in rapidly rotating systems. *J. Fluid Mech.* **44** 441–60

[55] Miesch M S, Elliott J R, Toomre J, Clune T L, Glatzmaier G A and Gilman P A 2000 Three-dimensional spherical simulations of solar convection: I. Differential rotation and pattern evolution achieved with laminar and turbulent states *Astrophys. J.* **532** 593–615

[56] Käpylä P J, Korpi M J, Brandenburg A, Mitra D and Tavakol R 2010 Convective dynamos in spherical wedge geometry *Astron. Nachr.* **331** 73–81

[57] Thompson M J, Christensen-Dalsgaard J, Miesch M S and Toomre J 2003 The internal rotation of the sun *Ann. Rev. Astron. Astrophys.* **41** 599–643

[58] Pevtsov A A, Canfield R C and Metcalf T R 1995 Latitudinal variation of helicity of photospheric magnetic fields *Astrophys. J. Lett.* **440** L109–12

[59] Deubner F-L and Gough D 1984 Helioseismology: oscillations as a daignostic of the solar interior *Ann. Rev. Astron. Astrophys.* **22** 593–619

[60] Gough D 1985 Inverting helioseismic data *Sol. Phys.* **100** 65–99

[61] Christensen-Dalsgaard J 2002 Helioseismology *Rev. Mod. Phys.* **74** 1073–129

[62] Basu S and Antia H M 2008 Helioseismology and solar abundances *Phys. Rep.* **457** 217–83

[63] Bahcall J N and Ulrich R K 1988 Solar models, neutrino experiments, and helioseismology *Rev. Mod. Phys.* **60** 297–372

[64] Schlattl H 2001 Three-flavor oscillation solutions for the solar neutrino problem *Phys. Rev.* D **64** 013009

[65] Christensen-Dalsgaard J, Di Mauro M P, Schlattl H and Weiss A 2005 On helioseismic tests of basic physics *Mon. Not. R. Astron. Soc.* **356** 587–95

[66] Mikheev S P and Smirnov A I 1986 Resonant amplification of neutrino oscillations in matter and solar-neutrino spectroscopy *Nuovo Cimento* C **9** 17–26

[67] Wolfenstein L 1978 Neutrino oscillations in matter *Phys. Rev.* D **17** 2369–74

[68] Gizon L, Duvall T L and Schou J 2003 Wave-like properties of solar supergranulation *Nature* **421** 43–4

[69] Spiegel E A and Zahn J-P 1992 The solar tachocline *Astron. Astrophys.* **265** 106–14

[70] Hughes D W, Rosner R and Weiss N O (ed) 2007 *The Solar Tachocline* (Cambridge: Cambridge University Press)

[71] Ossenkopf V and Mac Low M-M 2002 Turbulent velocity structure in molecular clouds *Astron. Astrophys.* **390** 307–26

[72] Larson R B 1979 Stellar kinematics and interstellar turbulence *Mon. Not. R. Astron. Soc.* **186** 479–90

[73] Larson R B 1981 Turbulence and star formation in molecular clouds *Mon. Not. R. Astron. Soc.* **194** 809–26

[74] Brunt C M and Heyer M H 2002 Interstellar turbulence: II. Energy spectra of molecular regions in the outer Galaxy *Astrophys. J.* **566** 289–301

[75] Brunt C M and Heyer M H 2002 Interstellar turbulence: I. Retrieval of velocity field statistics *Astrophys. J.* **566** 276–88

[76] Brunt C M, Heyer M H and Mac Low M-M 2009 Turbulent driving scales in molecular clouds *Astron. Astrophys.* **504** 883–90

[77] Rickett B J 1990 Radio propagation through the turbulent interstellar plasma *Ann. Rev. Astron. Astrophys.* **28** 561–605

[78] Boldyrev S and Gwinn C 2003 Scintillations and Lévy flights through the interstellar medium *Astrophys. J.* **584** 791–6

[79] de Avillez M A and Breitschwerdt D 2005 Global dynamical evolution of the ISM in star forming galaxies: I. High resolution 3D simulations: Effect of the magnetic field *Astron. Astrophys.* **436** 585–600

[80] Troland T H and Crutcher R M 2008 Magnetic fields in dark cloud cores: Arecibo OH Zeeman observations *Astrophys. J.* **680** 457–65

[81] Crutcher R M, Hakobian N and Troland T H 2009 Testing magnetic star formation theory *Astrophys. J.* **692** 844–55

[82] Crutcher R M 2009 *OH and CN Zeeman Observations of Magnetic Fields in Molecular Clouds* (*Revista Mexicana de Astronomia y Astrofisica Conference Series* vol 36) pp 107–12

[83] Yusef-Zadeh F, Morris M and Chance D 1984 Large, highly organized radio structures near the galactic centre *Nature* **310** 557–61

[84] Yusef-Zadeh F, Hewitt J W and Cotton W 2004 A 20 centimeter survey of the Galactic center region: I. Detection of numerous linear filaments *Astrophys. J. Suppl.* **155** 421–550

[85] Beck R, Brandenburg A, Moss D, Shukurov A and Sokoloff D 1996 Galactic magnetism: recent developments and perspectives *Ann. Rev. Astron. Astrophys.* **34** 155–206

[86] Balbus S A and Hawley J F 1998 Instability, turbulence, and enhanced transport in accretion disks *Rev. Mod. Phys.* **70** 1–53

[87] Cai K, Durisen R H, Boley A C, Pickett M K and Mejía A C 2008 The thermal regulation of gravitational instabilities in protoplanetary disks: IV. Simulations with envelope irradiation *Astrophys. J.* **673** 1138–53

[88] Frank J, King A and Raine D 1992 *Accretion Power in Astrophysics* (Cambridge: Cambridge University Press)

[89] Loken C, Roettiger K, Burns J O and Norman M 1995 Radio jet propagation and wide-angle tailed radio sources in merging galaxy cluster environments *Astrophys. J.* **445** 80–97

[90] Wik D R, Sarazin C L, Ricker P M and Randall S W 2008 The impact of galaxy cluster mergers on cosmological parameter estimation from surveys of the Sunyaev–Zel'dovich effect *Astrophys. J.* **680** 17–31

[91] Birkinshaw M 1999 The Sunyaev–Zel'dovich effect *Phys. Rep.* **310** 97–195

[92] Roettiger K, Burns J O and Stone J M 1999 A cluster merger and the origin of the extended radio emission in Abell 3667 *Astrophys. J.* **518** 603–12

[93] Roettiger K, Stone J M and Burns J O 1999 Magnetic field evolution in merging clusters of galaxies *Astrophys. J.* **518** 594–602

[94] Subramanian K, Shukurov A and Haugen N E L 2006 Evolving turbulence and magnetic fields in galaxy clusters *Mon. Not. R. Astron. Soc.* **366** 1437–54

[95] Jaffe W 1980 On the morphology of the magnetic field in galaxy clusters *Astrophys. J.* **241** 925–7

[96] Ruzmaikin A, Sokolov D and Shukurov A 1989 The dynamo origin of magnetic fields in galaxy clusters *Mon. Not. R. Astron. Soc.* **241** 1–14

[97] Goldman I and Rephaeli Y 1991 Turbulently generated magnetic fields in clusters of galaxies *Astrophys. J.* **380** 344–50

[98] Grasso D and Rubinstein H R 2001 Magnetic fields in the early Universe *Phys. Rep.* **348** 163–266

[99] Vachaspati T 2001 Estimate of the primordial magnetic field helicity *Phys. Rev. Lett.* **87** 251302

[100] Brandenburg A, Enqvist K and Olesen P 1996 Large-scale magnetic fields from hydromagnetic turbulence in the very early universe *Phys. Rev.* D **54** 1291–300

[101] Brandenburg A 2001 Magnetic mysteries *Science* **292** 2440–1

[102] Christensson M, Hindmarsh M and Brandenburg A 2001 Inverse cascade in decaying three-dimensional magnetohydrodynamic turbulence *Phys. Rev.* E **64** 056405

[103] Kang H S, Chester S and Meneveau C 2003 Decaying turbulence in an active-grid-generated flow and comparisons with large-eddy simulation *J. Fluid Mech.* **480** 129–60

[104] Haugen N E L and Brandenburg A 2004 Inertial range scaling in numerical turbulence with hyperviscosity *Phys. Rev.* E **70** 026405

[105] Biskamp D and Müller W-C 1999 Decay laws for three-dimensional magnetohydrodynamic turbulence *Phys. Rev. Lett.* **83** 2195–8

[106] Christensson M, Hindmarsh M and Brandenburg A 2005 Scaling laws in decaying helical hydromagnetic turbulence *Astron. Nachr.* **326** 393–9

[107] Banerjee R and Jedamzik K 2004 Evolution of cosmic magnetic fields: from the very early Universe, to recombination, to the present *Phys. Rev.* D **70** 123003

[108] Dolag K, Bartelmann M and Lesch H 2002 Evolution and structure of magnetic fields in simulated galaxy clusters *Astron. Astrophys.* **387** 383–95

[109] Dolag K, Grasso D, Springel V and Tkachev I 2005 Constrained simulations of the magnetic field in the local Universe and the propagation of ultrahigh energy cosmic rays *J. Cosmol. AstroPart Phys.* JCAP01(2005)009

[110] Tsagas C G 2005 Resonant amplification of magnetic seed fields by gravitational waves in the early universe *Phys. Rev.* D **72** 123509

[111] Caprini C and Durrer R 2006 Gravitational waves from stochastic relativistic sources: primordial turbulence and magnetic fields *Phys. Rev.* D **74** 063521

[112] Kahniashvili T, Campanelli L, Gogoberidze G, Maravin Y and Ratra B 2008 Gravitational radiation from primordial helical inverse cascade magnetohydrodynamic turbulence *Phys. Rev.* D **78** 123006

[113] Kahniashvili T, Gogoberidze G and Ratra B 2008 Gravitational radiation from primordial helical magnetohydrodynamic turbulence *Phys. Rev. Lett.* **100** 231301

[114] Turner N J, Blaes O M, Socrates A, Begelman M C and Davis S W 2005 The effects of photon bubble instability in radiation-dominated accretion disks *Astrophys. J.* **624** 267–88

[115] Richtmyer R D and Morton K W 1994 *Difference Methods for Initial-Value Problems* (New York: Interscience)

[116] Ogura Y and Phillips N A 1962 Scale analysis of deep and shallow convection in the atmosphere *J. Atmos. Sci.* **19** 173–9

[117] Gough D O 1969 The anelastic approximation for thermal convection *J. Atmos. Sci.* **26** 448–56

[118] Gilman P A and Glatzmaier G A 1981 Compressible convection in a rotating spherical shell: I. Anelastic equations: II. A linear anelastic model: III. Analytic model for compressible vorticity waves *Astrophys. J. Suppl.* **45** 335–88

[119] Nordlund Å 1982 Numerical simulations of the solar granulation: I. Basic equations and methods *Astron. Astrophys.* **107** 1–10

[120] Glatzmaier G A 1984 Numerical simulations of stellar convective dynamos: I. The model and method *J. Comput. Phys.* **55** 461–84

[121] Brun A S, Miesch M S and Toomre J 2004 Global-scale turbulent convection and magnetic dynamo action in the solar envelope *Astrophys. J.* **614** 1073–98

[122] Rogers T M and Glatzmaier G A 2005 Penetrative convection within the anelastic approximation *Astrophys. J.* **620** 432–41

[123] Brandenburg A, Moss D and Tuominen I 1992 Stratification and thermodynamics in mean-field dynamos *Astron. Astrophys.* **265** 328–44

[124] Smagorinsky J 1963 General circulation experiments with the primitive equations *Mon. Weather Rev.* **91** 99–164

[125] Scotti A, Meneveau C and Lilly D K 1993 Generalized Smagorinsky model for anisotropic grids *Phys. Fluids* **5** 2306–8

[126] Ansumali S, Karlin I V and Succi S 2004 Kinetic theory of turbulence modeling: smallness parameter, scaling and microscopic derivation of Smagorinsky model *Phys. A Stat. Mech. Appl.* **338** 379–94

[127] Lévêque E, Toschi F, Shao L and Bertoglio J-P 2007 Shear-improved Smagorinsky model for large-eddy simulation of wall-bounded turbulent flows *J. Fluid Mech.* **570** 491–502

[128] Stone J M, Gardiner T A, Teuben P, Hawley J F and Simon J B 2008 Athena: a new code for astrophysical MHD *Astrophys. J. Suppl.* **178** 137–77

[129] Teşileanu O, Mignone A and Massaglia S 2008 Simulating radiative astrophysical flows with the PLUTO code: a non-equilibrium, multi-species cooling function *Astron. Astrophys.* **488** 429–40

[130] Gressel O and Ziegler U 2007 Shearingbox-implementation for the central-upwind, constraint-transport MHD-code NIRVANA *Comput. Phys. Commun.* **176** 652–9

[131] Teyssier R 2002 Cosmological hydrodynamics with adaptive mesh refinement. A new high resolution code called RAMSES *Astron. Astrophys.* **385** 337–64

[132] Fryxell B, Olson K, Ricker P, Timmes F X, Zingale M, Lamb D Q, MacNeice P, Rosner R, Truran J W and Tufo H 2000 FLASH: an adaptive mesh hydrodynamics code for modeling astrophysical thermonuclear flashes *Astrophys. J. Suppl.* **131** 273–334

[133] O'Shea B W, Nagamine K, Springel V, Hernquist L and Norman M L 2005 Comparing AMR and SPH cosmological simulations: I. Dark matter and adiabatic simulations *Astrophys. J. Suppl.* **160** 1–27

[134] Porter D H, Pouquet A and Woodward P R 1992 Three-dimensional supersonic homogeneous turbulence—a numerical study *Phys. Rev. Lett.* **68** 3156–9

[135] Farge M 1992 Wavelet transforms and their applications to turbulence *Ann. Rev. Fluid Mech.* **24** 395–457

[136] Okamoto N, Yoshimatsu K, Schneider K, Farge M and Kaneda Y 2007 Coherent vortices in high resolution direct numerical simulation of homogeneous isotropic turbulence: a wavelet viewpoint *Phys. Fluids* **19** 115109

[137] Berkooz G, Holmes P and Lumley J L 1993 The proper orthogonal decomposition in the analysis of turbulent flows *Ann. Rev. Fluid Mech.* **25** 539–75

[138] Bos W J T, Futatani S, Benkadda S, Farge M and Schneider K 2008 The role of coherent vorticity in turbulent transport in resistive drift-wave turbulence *Phys. Plasmas* **15** 072305

[139] Barge P and Sommeria J 1995 Did planet formation begin inside persistent gaseous vortices? *Astron. Astrophys.* **295** L1–L4

[140] Tanga P, Babiano A, Dubrulle B and Provenzale A 1996 Forming planetesimals in vortices *Icarus* **121** 158–70

[141] Hodgson L S and Brandenburg A 1998 Turbulence effects in planetesimal formation *Astron. Astrophys.* **330** 1169–74

[142] Johansen A, Andersen A C and Brandenburg A 2004 Simulations of dust-trapping vortices in protoplanetary discs *Astron. Astrophys.* **417** 361–74

[143] Inaba S and Barge P 2006 Dusty vortices in protoplanetary disks *Astrophys. J.* **649** 415–27

[144] Berezinskii V S, Bulanov S V, Dogiel V A and Ptuskin V S 1990 *Astrophysics of Cosmic Rays* (Amsterdam: North-Holland)

[145] Hanasz M and Lesch H 2003 Incorporation of cosmic ray transport into the ZEUS MHD code. Application for studies of Parker instability in the ISM *Astron. Astrophys.* **412** 331–9

[146] Stein R F and Leibacher J 1974 Waves in the solar atmosphere *Ann. Rev. Astron. Astrophys.* **12** 407–35

[147] Brandenburg A 1988 Hydrodynamic Green's functions for atmospheric oscillations *Astron. Astrophys.* **203** 154–61

[148] Stein R F and Nordlund Å 1989 Topology of convection beneath the solar surface *Astrophys. J. Lett.* **342** L95–8

[149] Brandenburg A, Jennings R L, Nordlund Å, Rieutord M, Stein R F and Tuominen I 1996 Magnetic structures in a dynamo simulation *J. Fluid Mech.* **306** 325–52

[150] Brummell N H, Hurlburt N E and Toomre J 1996 Turbulent compressible convection with rotation: I. Flow structure and evolution *Astrophys. J.* **473** 494–513

[151] Hurlburt N E, Toomre J and Massaguer J M 1984 Two-dimensional compressible convection extending over multiple scale heights *Astrophys. J.* **282** 557–73

[152] Malkus W V R 1968 Precession of the Earth as the cause of geomagnetism *Science* **160** 259–64

[153] Loper D E 1975 Torque balance and energy budget for the precessionally driven dynamo *Phys. Earth Planet. Inter.* **11** 43–60

[154] Vanyo J P 1991 A geodynamo powered by luni-solar precession *Geophys. Astrophys. Fluid Dyn.* **59** 209–34

[155] Tilgner A 2005 Precession driven dynamos *Phys. Fluids* **17** 034104

[156] Stern D P 1970 Euler potentials *Am. J. Phys.* **38** 494–501

[157] Rosswog S and Price D 2007 MAGMA: a three-dimensional, Lagrangian magnetohydrodynamics code for merger applications *Mon. Not. R. Astron. Soc.* **379** 915–31

[158] Kotarba H, Lesch H, Dolag K, Naab T, Johansson P H and Stasyszyn F A 2009 Magnetic field structure due to the global velocity field in spiral galaxies *Mon. Not. R. Astron. Soc.* **397** 733–47

[159] Brandenburg A 2010 Magnetic field evolution in simulations with Euler potentials *Mon. Not. R. Astron. Soc.* **401** 347–54

[160] Solanki S K, Inhester B and Schüssler M 2006 The solar magnetic field *Rep. Prog. Phys.* **69** 563–668

[161] Mihalas D 1978 *Stellar Atmospheres* (San Francisco, CA: Freeman)

[162] Kritsuk A G and Norman M L 2002 Thermal instability-induced interstellar turbulence *Astrophys. J. Lett.* **569** L127–31

[163] Brandenburg A, Korpi M J and Mee A J 2007 Thermal instability in shearing and periodic turbulence *Astrophys. J.* **654** 945–54

[164] Bonnell I A, Bate M R and Zinnecker H 1998 On the formation of massive stars *Mon. Not. R. Astron. Soc.* **298** 93–102

[165] Bate M R and Burkert A 1997 Resolution requirements for smoothed particle hydrodynamics calculations with self-gravity *Mon. Not. R. Astron. Soc.* **288** 1060–72

[166] Padoan P and Nordlund Å 2002 The stellar initial mass function from turbulent fragmentation *Astrophys. J.* **576** 870–9

[167] Vázquez-Semadeni E, Ballesteros-Paredes J and Klessen R S 2003 A holistic scenario of turbulent molecular cloud evolution and control of the star formation efficiency: first tests *Astrophys. J. Lett.* **585** L131–4

[168] Krumholz M R, McKee C F and Klein R I 2004 Embedding Lagrangian sink particles in Eulerian grids *Astrophys. J.* **611** 399–412

[169] Krumholz M R, Klein R I and McKee C F 2007 Radiation-hydrodynamic simulations of collapse and fragmentation in massive protostellar cores *Astrophys. J.* **656** 959–79

[170] Jappsen A-K, Low M-M M, Glover S C O, Klessen R S and Kitsionas S 2009 Star formation at very low metallicity: V. The greater importance of initial conditions compared to metallicity thresholds *Astrophys. J.* **694** 1161–70

[171] Padoan P and Nordlund Å 2009 The star formation rate of supersonic MHD turbulence arXiv:0907.0248

[172] Stone J M and Norman M L 1992 ZEUS-2D: A radiation magnetohydrodynamics code for astrophysical flows in two space dimensions. I - The hydrodynamic algorithms and tests *Astrophys. J. Suppl.* **80** 753–90

[173] Monaghan J J 1992 Smoothed particle hydrodynamics *Ann. Rev. Astron. Astrophys.* **30** 543–74

[174] Springel V and Hernquist L 2002 Cosmological smoothed particle hydrodynamics simulations: the entropy equation *Mon. Not. R. Astron. Soc.* **333** 649–64

[175] Steinmetz M 1996 GRAPESPH: cosmological smoothed particle hydrodynamics simulations with the special-purpose hardware GRAPE *Mon. Not. R. Astron. Soc.* **278** 1005–17

[176] Springel V 2010 E pur si muove: Galilean-invariant cosmological hydrodynamical simulations on a moving mesh *Mon. Not. R. Astron. Soc.* **401** 791–851

[177] She Z-S, Jackson E and Orszag S A 1990 Intermittent vortex structures in homogeneous isotropic turbulence *Nature* **344** 226–8

[178] Vincent A and Meneguzzi M 1991 The spatial structure and statistical properties of homogeneous turbulence *J. Fluid Mech.* **225** 1–20

[179] Porter D H, Pouquet A and Woodward P R 1994 Kolmogorov-like spectra in decaying three-dimensional supersonic flows *Phys. Fluids* **6** 2133–42

[180] Haugen N E, Brandenburg A and Dobler W 2004 Simulations of nonhelical hydromagnetic turbulence *Phys. Rev.* E **70** 016308

[181] Mac Low M-M and Klessen R S 2004 Control of star formation by supersonic turbulence *Rev. Mod. Phys.* **76** 125–94

[182] Padoan P, Nordlund Å and Jones B J T 1997 The universality of the stellar initial mass function *Mon. Not. R. Astron. Soc.* **288** 145–52

[183] Padoan P and Nordlund Å 1999 A super-Alfvénic model of dark clouds *Astrophys. J.* **526** 279–94

[184] Padoan P, Juvela M, Kritsuk A and Norman M L 2006 The power spectrum of supersonic turbulence in Perseus *Astrophys. J. Lett.* **653** L125–8

[185] Kadomtsev B B and Petviashvili V I 1973 Acoustic turbulence *Sov. Phys. Dokl.* **18** 115–6

[186] Beresnyak A and Lazarian A 2009 Comparison of spectral slopes of magnetohydrodynamic and hydrodynamic turbulence and measurements of alignment effects *Astrophys. J.* **702** 1190–8

[187] Lee E, Brachet M E, Pouquet A, Mininni P D and Rosenberg D 2010 Lack of universality in decaying magnetohydrodynamic turbulence *Phys. Rev.* E **81** 016318

[188] Iroshnikov P S 1964 Turbulence of a conducting fluid in a strong magnetic field *Sov. Astron.* **7** 566–71

[189] Kraichnan R H 1965 Inertial-range spectrum of hydromagnetic turbulence *Phys. Fluids* **8** 1385–7

[190] Galtier S, Nazarenko S V, Newell A C and Pouquet A 2000 A weak turbulence theory for incompressible magnetohydrodynamics *J. Plasma Phys.* **63** 447–88

[191] Goldreich P and Sridhar S 1995 Toward a theory of interstellar turbulence: II. Strong Alfvénic turbulence *Astrophys. J.* **438** 763–75

[192] Goldreich P and Sridhar S 1997 Magnetohydrodynamic turbulence revisited *Astrophys. J.* **485** 680–8

[193] Sridhar S and Goldreich P 1994 Toward a theory of interstellar turbulence: I. Weak Alfvénic turbulence *Astrophys. J.* **432** 612–21

[194] Lithwick Y, Goldreich P and Sridhar S 2007 Imbalanced strong MHD turbulence *Astrophys. J.* **655** 269–74

[195] Lithwick Y and Goldreich P 2003 Imbalanced weak magnetohydrodynamic turbulence *Astrophys. J.* **582** 1220–40

[196] Haugen N E L, Brandenburg A and Dobler W 2003 Is nonhelical hydromagnetic turbulence peaked at small scales? *Astrophys. J. Lett.* **597** L141–4

[197] de Avillez M A and Breitschwerdt D 2007 The generation and dissipation of interstellar turbulence: results from large-scale high-resolution simulations *Astrophys. J. Lett.* **665** L35–8

[198] Pouquet A, Baerenzung J, Pietarila Graham J, Mininni P, Politano H and Ponty Y 2009 Modeling of anisotropic turbulent flows with either magnetic fields or imposed rotation arXiv:0904.4860

[199] Boldyrev S 2005 On the spectrum of magnetohydrodynamic turbulence *Astrophys. J. Lett.* **626** L37–40

[200] Boldyrev S 2006 Spectrum of magnetohydrodynamic turbulence *Phys. Rev. Lett.* **96** 115002

[201] Mason J, Cattaneo F and Boldyrev S 2006 Dynamic alignment in driven magnetohydrodynamic turbulence *Phys. Rev. Lett.* **97** 255002

[202] Perez J C and Boldyrev S 2008 On weak and strong magnetohydrodynamic turbulence *Astrophys. J. Lett.* **672** L61–4

[203] Kritsuk A G, Ustyugov S D, Norman M L and Padoan P 2009 Simulating supersonic turbulence in magnetized molecular clouds *J. Phys.: Conf. Ser.* **180** 012020

[204] Kritsuk A G, Ustyugov S D, Norman M L and Padoan P 2009 *Simulations of Supersonic Turbulence in Molecular Clouds: Evidence for a New Universality* (*Astronomical Society of the Pacific Conference Series* vol 406) (San Francisco, CA: Astron. Soc. Pacific) pp 15–22

[205] Brandenburg A 2009 Large-scale dynamos at low magnetic Prandtl numbers *Astrophys. J.* **697** 1206–13

[206] Ponty Y, Mininni P D, Montgomery D C, Pinton J-F, Politano H and Pouquet A 2005 Numerical study of dynamo action at low magnetic Prandtl numbers *Phys. Rev. Lett.* **94** 164502

[207] Ponty Y, Mininni P D, Pinton J-F, Politano H and Pouquet A 2007 Dynamo action at low magnetic Prandtl numbers: mean flow versus fully turbulent motions *New J. Phys.* **9** 296

[208] Schekochihin A A, Haugen N E L, Brandenburg A, Cowley S C, Maron J L and McWilliams J C 2005 The onset of a small-scale turbulent dynamo at low magnetic Prandtl numbers *Astrophys. J. Lett.* **625** L115–8

[209] Rogachevskii I and Kleeorin N 1997 Intermittency and anomalous scaling for magnetic fluctuations *Phys. Rev.* E **56** 417–26

[210] Boldyrev S and Cattaneo F 2004 Magnetic-field generation in Kolmogorov turbulence *Phys. Rev. Lett.* **92** 144501

[211] Iskakov A B, Schekochihin A A, Cowley S C, McWilliams J C and Proctor M R E 2007 Numerical demonstration of fluctuation dynamo at low magnetic Prandtl numbers *Phys. Rev. Lett.* **98** 208501

[212] Schekochihin A A, Iskakov A B, Cowley S C, McWilliams J C, Proctor M R E and Yousef T A 2007 Fluctuation dynamo and turbulent induction at low magnetic Prandtl numbers *New J. Phys.* **9** 300

[213] Brandenburg A 2001 The inverse cascade and nonlinear alpha-effect in simulations of isotropic helical hydromagnetic turbulence *Astrophys. J.* **550** 824–40

[214] Alexakis A, Bigot B, Politano H and Galtier S 2007 Anisotropic fluxes and nonlocal interactions in magnetohydrodynamic turbulence *Phys. Rev.* E **76** 056313

[215] Kerr R M 1996 Rayleigh number scaling in numerical convection *J. Fluid Mech.* **310** 139–79

[216] Julien K, Legg S, McWilliams J and Werne J 1996 Rapidly rotating turbulent Rayleigh–Benard convection *J. Fluid Mech.* **322** 243–73

[217] Hartlep T, Tilgner A and Busse F H 2003 Large scale structures in Rayleigh–Bénard convection at high Rayleigh numbers *Phys. Rev. Lett.* **91** 064501

[218] Cattaneo F, Brummell N H, Toomre J, Malagoli A and Hurlburt N E 1991 Turbulent compressible convection *Astrophys. J.* **370** 282–94

[219] Stein R F and Nordlund Å 1998 Simulations of solar granulation: I. General properties *Astrophys. J.* **499** 914–33

[220] Hurlburt N E, Toomre J and Massaguer J M 1986 Nonlinear compressible convection penetrating into stable layers and producing internal gravity waves *Astrophys. J.* **311** 563–77

[221] Dintrans B and Brandenburg A 2004 Identification of gravity waves in hydrodynamical simulations *Astron. Astrophys.* **421** 775–82

[222] Dintrans B, Brandenburg A, Nordlund Å and Stein R F 2005 Spectrum and amplitudes of internal gravity waves excited by penetrative convection in solar-type stars *Astron. Astrophys.* **438** 365–76

[223] Rogers T M and Glatzmaier G A 2005 Gravity waves in the Sun *Mon. Not. R. Astron. Soc.* **364** 1135–46

[224] Rogers T M, MacGregor K B and Glatzmaier G A 2008 Non-linear dynamics of gravity wave driven flows in the solar radiative interior *Mon. Not. R. Astron. Soc.* **387** 616–30

[225] Belkacem K, Samadi R, Goupil M J, Dupret M A, Brun A S and Baudin F 2009 Stochastic excitation of nonradial modes. II. Are solar asymptotic gravity modes detectable? *Astron. Astrophys.* **494** 191–204

[226] Käpylä P J, Korpi M J and Brandenburg A 2008 Large-scale dynamos in turbulent convection with shear *Astron. Astrophys.* **491** 353–62

[227] Gilman P A 1983 Dynamically consistent nonlinear dynamos driven by convection in a rotating spherical shell: II. Dynamos with cycles and strong feedbacks *Astrophys. J. Suppl.* **53** 243–68

[228] Glatzmaier G A 1985 Numerical simulations of stellar convective dynamos: II. Field propagation in the convection zone *Astrophys. J.* **291** 300–7

[229] Brown B P, Browning M K, Brun A S, Miesch M S and Toomre J 2010 Persistent magnetic wreaths in a rapidly rotating Sun *Astrophys. J.* **711** 424–38

[230] Hart J E, Toomre J, Deane A E, Hurlburt N E, Glatzmaier G A, Fichtl G H, Leslie F, Fowlis W W and Gilman P A 1986 Laboratory experiments on planetary and stellar convection performed on Spacelab 3 *Science* **234** 61–4

[231] Mitra D, Tavakol R, Brandenburg A and Moss D 2009 Turbulent dynamos in spherical shell segments of varying geometrical extent *Astrophys. J.* **697** 923–33

[232] Mitra D, Tavakol R, Käpylä P J and Brandenburg A 2010 Oscillatory migrating magnetic fields in helical turbulence in spherical domains *Astrophys. J. Lett.* **719** L1–L4

[233] Mitra D, Candelaresi S, Chatterjee P, Tavakol R and Brandenburg A 2010 Equatorial magnetic helicity flux in simulations with different gauges. *Astron. Nachr.* **331** 130–5

[234] Green C A and Kosovichev A G 2006 Traveling convective modes in the Sun's subsurface shear layer *Astrophys. J. Lett.* **641** L77–L80

[235] Green C A and Kosovichev A G 2007 Magnetic effect on wave-like properties of solar supergranulation *Astrophys. J. Lett.* **665** L75–8

[236] Busse F H 2007 Convection in the presence of an inclined axis of rotation with applications to the Sun *Sol. Phys.* **245** 27–36

[237] Brandenburg A 2007 Near-surface shear layer dynamics *IAU Symp.* vol 239 ed T Kuroda *et al* pp 457–66

[238] Benevolenskaya E E, Hoeksema J T, Kosovichev A G and Scherrer P H 1999 The interaction of new and old magnetic fluxes at the beginning of Solar Cycle 23 *Astrophys. J. Lett.* **517** L163–6

[239] Brandenburg A 2005 The case for a distributed solar dynamo shaped by near-surface shear *Astrophys. J.* **625** 539–47

[240] Allende Prieto C, Lambert D L and Asplund M 2001 The forbidden abundance of oxygen in the Sun *Astrophys. J. Lett.* **556** L63–6

[241] Asplund M, Grevesse N, Sauval A J, Allende Prieto C and Kiselman D 2004 Line formation in solar granulation: IV. [O I], O I and OH lines and the photospheric O abundance *Astron. Astrophys.* **417** 751–68

[242] Asplund M, Grevesse N and Sauval A J 2005 The solar chemical composition *Cosmic Abundances as Records of Stellar Evolution and Nucleosynthesis* (*Astronomical Society of the Pacific Conference Series* vol 336) ed T G Barnes III and F N Bash (San Francsico, CA: Astron. Soc. Pacific) pp 25–38

[243] Caffau E, Maiorca E, Bonifacio P, Faraggiana R, Steffen M, Ludwig H-G, Kamp I and Busso M 2009 The solar photospheric nitrogen abundance. Analysis of atomic transitions with 3D and 1D model atmospheres *Astron. Astrophys.* **498** 877–84

[244] Anders E and Grevesse N 1989 Abundances of the elements - meteoritic and solar *Geochim. Cosmochimi. Acta* **53** 197–214

[245] Bahcall J N, Pinsonneault M H and Basu S 2001 Solar models: current epoch and time dependences, neutrinos, and helioseismological properties *Astrophys. J.* **555** 990–1012

[246] Bahcall J N, Serenelli A M and Basu S 2006 10,000 standard solar models: a Monte Carlo simulation *Astrophys. J. Suppl.* **165** 400–31

[247] Haxton W C and Serenelli A M 2008 CN cycle solar neutrinos and the Sun's primordial core metallicity *Astrophys. J.* **687** 678–91

[248] Antia H M and Basu S 2006 Determining solar abundances using helioseismology *Astrophys. J.* **644** 1292–8

[249] Richard O, Vauclair S, Charbonnel C and Dziembowski W A 1996 New solar models including helioseismological constraints and light-element depletion *Astron. Astrophys.* **312** 1000–11

[250] Rempel M 2004 Overshoot at the base of the solar convection zone: a semianalytical approach *Astrophys. J.* **607** 1046–64

[251] Bahcall J N, Basu S, Pinsonneault M and Serenelli A M 2005 Helioseismological implications of recent solar abundance determinations *Astrophys. J.* **618** 1049–56

[252] Meléndez J, Ramírez I, Casagrande L, Asplund M, Gustafsson B, Yong D, Do Nascimento J D, Castro M and Bazot M 2010 The solar, exoplanet and cosmological lithium problems *Astrophys. Space Sci.* **328** 193–200

[253] Brandenburg A, Dintrans B and Haugen N E L 2004 Shearing and embedding box simulations of the magnetorotational

instability *MHD Couette Flows: Experiments and Models* ed R Rosner *et al*; AIP Conf. Proc. **733** 122–36

[254] Fromang S and Papaloizou J 2007 MHD simulations of the magnetorotational instability in a shearing box with zero net flux: I. The issue of convergence *Astron. Astrophys.* **476** 1113–22

[255] Fromang S, Papaloizou J, Lesur G and Heinemann T 2007 MHD simulations of the magnetorotational instability in a shearing box with zero net flux: II. The effect of transport coefficients *Astron. Astrophys.* **476** 1123–32

[256] Rüdiger G, Schultz M and Shalybkov D 2003 Linear magnetohydrodynamic Taylor–Couette instability for liquid sodium *Phys. Rev.* E **67** 046312

[257] Hollerbach R and Rüdiger G 2005 New type of magnetorotational instability in cylindrical Taylor–Couette flow *Phys. Rev. Lett.* **95** 124501

[258] Stefani F, Gundrum T, Gerbeth G, Rüdiger G, Schultz M, Szklarski J and Hollerbach R 2006 Experimental evidence for magnetorotational instability in a Taylor–Couette flow under the influence of a helical magnetic field *Phys. Rev. Lett.* **97** 184502

[259] Stefani F, Gundrum T, Gerbeth G, Rüdiger G, Szklarski J and Hollerbach R 2007 Experiments on the magnetorotational instability in helical magnetic fields *New J. Phys.* **9** 295

[260] Rüdiger G, Hollerbach R, Gellert M and Schultz M 2007 The azimuthal magnetorotational instability (AMRI) *Astron. Nachr.* **328** 1158–61

[261] Mininni P D 2007 Inverse cascades and α effect at a low magnetic Prandtl number *Phys. Rev.* E **76** 026316

[262] Brandenburg A, Nordlund Å, Stein R F and Torkelsson U 1995 Dynamo-generated turbulence and large-scale magnetic fields in a Keplerian shear flow *Astrophys. J.* **446** 741–54

[263] Brandenburg A and Sokoloff D 2002 Local and nonlocal magnetic diffusion and alpha-effect tensors in shear flow turbulence *Geophys. Astrophys. Fluid Dyn.* **96** 319–44

[264] Käpylä P J and Korpi M J 2010 Magnetorotational instability driven dynamos at low magnetic Prandtl numbers arXiv:1004.2417

[265] Yousef T A, Heinemann T, Schekochihin A A, Kleeorin N, Rogachevskii I, Iskakov A B, Cowley S C and McWilliams J C 2008 Generation of magnetic field by combined action of turbulence and shear *Phys. Rev. Lett.* **100** 184501

[266] Yousef T A, Heinemann T, Rincon F, Schekochihin A A, Kleeorin N, Rogachevskii I, Cowley S C and McWilliams J C 2008 Numerical experiments on dynamo action in sheared and rotating turbulence *Astron. Nachr.* **329** 737–49

[267] Brandenburg A, Rädler K-H, Rheinhardt M and Käpylä P J 2008 Magnetic diffusivity tensor and dynamo effects in rotating and shearing turbulence *Astrophys. J.* **676** 740–51

[268] Vishniac E T and Brandenburg A 1997 An incoherent alpha–Omega dynamo in accretion disks *Astrophys. J.* **475** 263–74

[269] Proctor M R E 2007 Effects of fluctuation on $\alpha\Omega$ dynamo models *Mon. Not. R. Astron. Soc.* **382** L39–L42

[270] Rogachevskii I and Kleeorin N 2003 Electromotive force and large-scale magnetic dynamo in a turbulent flow with a mean shear *Phys. Rev.* E **68** 036301

[271] Rogachevskii I and Kleeorin N 2004 Nonlinear theory of a 'shear-current' effect and mean-field magnetic dynamos *Phys. Rev.* E **70** 046310

[272] Brandenburg A 2005 Turbulence and its parameterization in accretion discs *Astron. Nachr.* **326** 787–97

[273] Rädler K-H and Stepanov R 2006 Mean electromotive force due to turbulence of a conducting fluid in the presence of mean flow *Phys. Rev.* E **73** 056311

[274] Rüdiger G and Kitchatinov L L 2006 Do mean-field dynamos in nonrotating turbulent shear-flows exist? *Astron. Nachr.* **327** 298–303

[275] Wisdom J and Tremaine S 1988 Local simulations of planetary rings *Astron. J.* **95** 925–40

[276] Hawley J F, Gammie C F and Balbus S A 1995 Local three-dimensional magnetohydrodynamic simulations of accretion disks *Astrophys. J.* **440** 742–63

[277] Hawley J F 2000 Global magnetohydrodynamical simulations of accretion tori *Astrophys. J.* **528** 462–79

[278] Machida M, Hayashi M R and Matsumoto R 2000 Global simulations of differentially rotating magnetized disks: formation of low-β filaments and structured coronae *Astrophys. J. Lett.* **532** L67–L70

[279] Machida M and Matsumoto R 2003 Global three-dimensional magnetohydrodynamic simulations of black hole accretion disks: x-ray flares in the plunging region *Astrophys. J.* **585** 429–42

[280] De Villiers J-P, Hawley J F and Krolik J H 2003 Magnetically driven accretion flows in the Kerr metric: I. Models and overall structure *Astrophys. J.* **599** 1238–53

[281] Shakura N I and Sunyaev R A 1973 Black holes in binary systems. Observational appearance *Astron. Astrophys.* **24** 337–55

[282] Krolik J H and Hawley J F 2002 Where is the inner edge of an accretion disk around a black hole? *Astrophys. J.* **573** 754–63

[283] Beckwith K, Hawley J F and Krolik J H 2008 Where is the radiation edge in magnetized black hole accretion discs? *Mon. Not. R. Astron. Soc.* **390** 21–38

[284] Johansen A, Oishi J S, Low M-M M, Klahr H, Henning T and Youdin A 2007 Rapid planetesimal formation in turbulent circumstellar disks *Nature* **448** 1022–5

[285] Johansen A, Oishi J S, Mac Low M-M, Klahr H, Henning T and Youdin A 2007 Supplementary Information for 'Rapid planetesimal formation in turbulent circumstellar discs' arXiv:0708.3893

[286] Field G B 1965 Thermal instability *Astrophys. J.* **142** 531–67

[287] Inutsuka S and Koyama H 2007 Dynamics of a Multi-Phase Interstellar Medium *SINS—Small Ionized and Neutral Structures in the Diffuse Interstellar Medium* (*Astronomical Society of the Pacific Conference Series* vol 365) ed M Haverkorn and W M Goss (San Francisco, CA: Astron. Soc. Pacific) pp 162–5

[288] Truelove J K, Klein R I, McKee C F, Holliman J H II, Howell L H and Greenough J A 1997 The Jeans condition: a new constraint on spatial resolution in simulations of isothermal self-gravitational hydrodynamics *Astrophys. J. Lett.* **489** L179

[289] Jeans J H 1902 The stability of a spherical nebula *R. Soc. Lond. Phil. Trans. Ser.* A **199** 1–53

[290] Bonnor W B 1956 Boyle's Law and gravitational instability *Mon. Not. R. Astron. Soc.* **116** 351–9

[291] Bromm V and Larson R B 2004 The first stars *Ann. Rev. Astron. Astrophys.* **42** 79–118

[292] Binney J and Tremaine S 1987 *Galactic Dynamics* (Princeton, NJ: Princeton University Press)

[293] Gammie C F 2001 Nonlinear outcome of gravitational instability in cooling, gaseous disks *Astrophys. J.* **553** 174–83

[294] Durisen R H, Boss A P, Mayer L, Nelson A F, Quinn T and Rice W K M 2007 Gravitational instabilities in gaseous protoplanetary disks and implications for giant planet formation *Protostars and Planets V* (Tucson, AZ: University of Arizona Press) pp 607–22

[295] Klessen R S and Hennebelle P 2009 Accretion-driven turbulence as universal process: galaxies molecular clouds, and protostellar disks *Astron. Astrophys.* **520** A17

[296] Bate M R, Bonnell I A and Bromm V 2003 The formation of a star cluster: predicting the properties of stars and brown dwarfs *Mon. Not. R. Astron. Soc.* **339** 577–99

[297] Padoan P, Nordlund Å, Kritsuk A G, Norman M L and Li P S 2007 Two regimes of turbulent fragmentation and the stellar initial mass function from primordial to present-day star formation *Astrophys. J.* **661** 972–81

[298] Bonnell I A, Clark P and Bate M R 2008 Gravitational fragmentation and the formation of brown dwarfs in stellar clusters *Mon. Not. R. Astron. Soc.* **389** 1556–62

[299] Korpi M J, Brandenburg A, Shukurov A, Tuominen I and Nordlund Å 1999 A supernova-regulated interstellar medium: simulations of the turbulent multiphase medium *Astrophys. J. Lett.* **514** L99–L102

[300] de Avillez M A and Breitschwerdt D 2004 Volume filling factors of the ISM phases in star forming galaxies: I. The role of the disk-halo interaction *Astron. Astrophys.* **425** 899–911

[301] Mac Low M-M, Balsara D S, Kim J and de Avillez M A 2005 The distribution of pressures in a supernova-driven interstellar medium: I. Magnetized medium *Astrophys. J.* **626** 864–76

[302] McKee C F and Ostriker J P 1977 A theory of the interstellar medium—three components regulated by supernova explosions in an inhomogeneous substrate *Astrophys. J.* **218** 148–69

[303] Korpi M, Brandenburg A, Shukurov A and Tuominen I 1999 Vortical motions driven by supernova explosions *Interstellar Turbulence* ed J Franco and A Carraminana (Cambridge: Cambridge University Press) pp 127–31

[304] Del Sordo F and Brandenburg A 2010 Vorticity production through rotation, shear and baroclinicity arXiv:1008.5281

[305] Mee A J and Brandenburg A 2006 Turbulence from localized random expansion waves *Mon. Not. R. Astron. Soc.* **370** 415–9

[306] Porter D H, Woodward P R and Pouquet A 1998 Inertial range structures in decaying compressible turbulent flows *Phys. Fluids* **10** 237–45

[307] Haugen N E L, Brandenburg A and Mee A J 2004 Mach number dependence of the onset of dynamo action *Mon. Not. R. Astron. Soc.* **353** 947–52

[308] Kritsuk A G, Ustyugov S D, Norman M L and Padoan P 2010 Self-organization in turbulent molecular clouds: compressional versus solenoidal modes *ASP Conf. Ser.* **429** 15–21 (arXiv:0912.0546)

[309] Pan L and Scannapieco E 2010 Mixing in supersonic turbulence *Astrophys. J.* **721** 1765–82

[310] Ignatius J, Kajantie K, Kurki-Suonio H and Laine M 1994 Growth of bubbles in cosmological phase transitions *Phys. Rev.* D **49** 3854–68

[311] Kajantie K and Kurki-Suonio H 1986 Bubble growth and droplet decay in the quark-hadron phase transition in the early Universe *Phys. Rev.* D **34** 1719–38

[312] Mason P J and Thomson D J 1987 Large-eddy simulations of the neutral-static-stability planetary boundary layer *Q. J. R. Meteorol. Soc.* **113** 413–43

[313] Sullivan P P, McWilliams J C and Moeng C-H 1994 A subgrid-scale model for large-eddy simulation of planetary boundary-layer flows *Boundary-Layer Meteorol.* **71** 247–76

[314] Brandenburg A, Käpylä P J and Mohammed A 2004 Non-Fickian diffusion and tau approximation from numerical turbulence *Phys. Fluids* **16** 1020–7

[315] Sur S, Subramanian K and Brandenburg A 2007 Kinetic and magnetic α-effects in non-linear dynamo theory *Mon. Not. R. Astron. Soc.* **376** 1238–50

[316] Brandenburg A, Rädler K-H and Schrinner M 2008 Scale dependence of alpha effect and turbulent diffusivity *Astron. Astrophys.* **482** 739–46

[317] Brandenburg A, Svedin A and Vasil G M 2009 Turbulent diffusion with rotation or magnetic fields *Mon. Not. R. Astron. Soc.* **395** 1599–606

[318] Parker E N 1979 *Cosmical Magnetic Fields: their Origin and their Activity* (Oxford: Clarendon)

[319] Krause F and Raedler K H 1980 *Mean-Field Magnetohydrodynamics and Dynamo Theory* (Oxford: Pergamon)

[320] Pouquet A, Frisch U and Leorat J 1976 Strong MHD helical turbulence and the nonlinear dynamo effect *J. Fluid Mech.* **77** 321–54

[321] Blackman E G and Field G B 2002 New dynamical mean-field dynamo theory and closure approach *Phys. Rev. Lett.* **89** 265007

[322] Rädler K-H, Kleeorin N and Rogachevskii I 2003 The mean electromotive force for MHD turbulence: the case of a weak mean magnetic field and slow rotation *Geophys. Astrophys. Fluid Dyn.* **97** 249–74

[323] Cattaneo F and Hughes D W 1996 Nonlinear saturation of the turbulent α effect *Phys. Rev.* E **54** R4532–5

[324] Kleeorin N, Moss D, Rogachevskii I and Sokoloff D 2000 Helicity balance and steady-state strength of the dynamo generated galactic magnetic field *Astron. Astrophys.* **361** L5–L8

[325] Blackman E G and Field G B 2000 Coronal activity from dynamos in astrophysical rotators *Mon. Not. R. Astron. Soc.* **318** 724–32

[326] Subramanian K and Brandenburg A 2006 Magnetic helicity density and its flux in weakly inhomogeneous turbulence *Astrophys. J. Lett.* **648** L71–4

[327] Vishniac E T and Cho J 2001 Magnetic helicity conservation and astrophysical dynamos *Astrophys. J.* **550** 752–60

[328] Subramanian K and Brandenburg A 2004 Nonlinear current helicity fluxes in turbulent dynamos and alpha quenching *Phys. Rev. Lett.* **93** 205001

[329] Hubbard A and Brandenburg A 2010 Magnetic helicity flux in the presence of shear arXiv:1006.3549

[330] Shukurov A, Sokoloff D, Subramanian K and Brandenburg A 2006 Galactic dynamo and helicity losses through fountain flow *Astron. Astrophys.* **448** L33–6

[331] Ruediger G 1980 Reynolds stresses and differential rotation: I. On recent calculations of zonal fluxes in slowly rotating stars *Geophys. Astrophys. Fluid Dyn.* **16** 239–61

[332] Ruediger G 1989 *Differential Rotation and Stellar Convection. Sun and the Solar Stars* (New York: Gordon and Breach)

[333] Kitchatinov L L and Ruediger G 1995 Differential rotation in solar-type stars: revisiting the Taylor-number puzzle *Astron. Astrophys.* **299** 446–52

[334] Durney B R 1993 On the solar differential rotation—meridional motions associated with a slowly varying angular velocity *Astrophys. J.* **407** 367–79

[335] Durney B R 1989 On the behavior of the angular velocity in the lower part of the solar convection zone *Astrophys. J.* **338** 509–27

[336] Gilman P A and Miller J 1986 Nonlinear convection of a compressible fluid in a rotating spherical shell *Astrophys. J. Suppl.* **61** 585–608

[337] Rieutord M, Brandenburg A, Mangeney A and Drossart P 1994 Reynolds stresses and differential rotation in Boussinesq convection in a rotating spherical shell *Astron. Astrophys.* **286** 471–80

[338] Pulkkinen P, Tuominen I, Brandenburg A, Nordlund Å and Stein R F 1993 Rotational effects on convection simulated at different latitudes *Astron. Astrophys.* **267** 265–74

[339] Brandenburg A, Tuominen I, Moss D and Ruediger G 1990 The nonlinear solar dynamo and differential rotation—a Taylor number puzzle? *Sol. Phys.* **128** 243–51

[340] Kitchatinov L L and Rüdiger G 2005 Differential rotation and meridional flow in the solar convection zone and beneath *Astron. Nachr.* **326** 379–85

[341] Brun A S and Toomre J 2002 Turbulent convection under the influence of rotation: sustaining a strong differential rotation. *Astrophys. J.* **570** 865–85

[342] Miesch M S, Brun A S and Toomre J 2006 Solar differential rotation influenced by latitudinal entropy variations in the tachocline *Astrophys. J.* **641** 618–25

[343] Jouve L and Brun A S 2007 On the role of meridional flows in flux transport dynamo models *Astron. Astrophys.* **474** 239–50

[344] Ballot J, Brun A S and Turck-Chièze S 2007 Simulations of turbulent convection in rotating young solar-like stars: differential rotation and meridional circulation *Astrophys. J.* **669** 1190–208

[345] Küker M, Rüdiger G and Kitchatinov L L 1993 An alpha Omega-model of the solar differential rotation *Astron. Astrophys.* **279** L1–4

[346] Kitchatinov L L, Pipin V V and Ruediger G 1994 Turbulent viscosity, magnetic diffusivity, and heat conductivity under the influence of rotation and magnetic field *Astron. Nachr.* **315** 157–70

[347] Rempel M 2005 Solar differential rotation and meridional flow: the role of a subadiabatic tachocline for the Taylor–Proudman balance *Astrophys. J.* **622** 1320–32

[348] Balbus S A 2009 A simple model for solar isorotational contours *Mon. Not. R. Astron. Soc.* **395** 2056–64

[349] Balbus S A, Bonart J, Latter H N and Weiss N O 2009 Differential rotation and convection in the Sun *Mon. Not. R. Astron. Soc.* **400** 176–82

[350] Tuominen I and Ruediger G 1989 Solar differential rotation as a multiparameter turbulence problem *Astron. Astrophys.* **217** 217–28

[351] Schrinner M, Rädler K-H, Schmitt D, Rheinhardt M and Christensen U 2005 Mean-field view on rotating magnetoconvection and a geodynamo model *Astron. Nachr.* **326** 245–9

[352] Schrinner M, Rädler K-H, Schmitt D, Rheinhardt M and Christensen U R 2007 Mean-field concept and direct numerical simulations of rotating magnetoconvection and the geodynamo *Geophys. Astrophys. Fluid Dyn.* **101** 81–116

[353] Kraichnan R H 1972 Test-field model for inhomogeneous turbulence *J. Fluid Mech.* **56** 287–304

[354] Madarassy E J M and Brandenburg A 2010 Calibrating passive scalar transport in shear-flow turbulence *Phys. Rev.* E **82** 016304

[355] Hubbard A and Brandenburg A 2009 Memory effects in turbulent transport *Astrophys. J.* **706** 712–26

[356] Sur S, Brandenburg A and Subramanian K 2008 Kinematic α-effect in isotropic turbulence simulations *Mon. Not. R. Astron. Soc.* **385** L15–L19

[357] Mitra D, Käpylä P J, Tavakol R and Brandenburg A 2009 Alpha effect and diffusivity in helical turbulence with shear *Astron. Astrophys.* **495** 1–8

[358] Brandenburg A, Rädler K-H, Rheinhardt M and Subramanian K 2008 Magnetic quenching of α and diffusivity tensors in helical turbulence *Astrophys. J. Lett.* **687** L49–L52

[359] Cattaneo F and Tobias S M 2009 Dynamo properties of the turbulent velocity field of a saturated dynamo *J. Fluid Mech.* **621** 205–14

[360] Tilgner A and Brandenburg A 2008 A growing dynamo from a saturated Roberts flow dynamo *Mon. Not. R. Astron. Soc.* **391** 1477–81

[361] Tschäpe R and Rüdiger G 2001 Rotation-induced lithium depletion of solar-type stars in open stellar clusters *Astron. Astrophys.* **377** 84–9

[362] Rüdiger G and Pipin V V 2001 Lithium as a passive tracer probing the rotating solar tachocline turbulence *Astron. Astrophys.* **375** 149–54